PNNL-28980

FY 2018 Report of the Atmosphere to Electrons Mesoscale-to-Microscale Coupling Project

January 2019

SE Haupt
L Berg
A DeCastro
E Koo
R Kotamarthi
L Mazzaro
E Quon
J Sauer
W Shaw
D Allaerts
M Churchfield
C Draxl
B Kosović
B Kravitz
J Mirocha
R Rai
G Sever

Prepared for the U.S. Department of Energy
under Contract DE-AC05-76RL01830

PACIFIC NORTHWEST NATIONAL LABORATORY
operated by
BATTELLE
for the
UNITED STATES DEPARTMENT OF ENERGY
under Contract DE-AC05-76RL01830

Printed in the United States of America

Available to DOE and DOE contractors from
the Office of Scientific and Technical Information,
P.O. Box 62, Oak Ridge, TN 37831-0062
www.osti.gov
ph: (865) 576-8401
fox: (865) 576-5728
email: reports@osti.gov

Available to the public from the National Technical Information Service
5301 Shawnee Rd., Alexandria, VA 22312
ph: (800) 553-NTIS (6847)
or (703) 605-6000
email: info@ntis.gov
Online ordering: http://www.ntis.gov

PNNL-28980

FY 2018 Report of the Atmosphere to Electrons Mesoscale-to-Microscale Coupling Project

January 2019

SE Haupt[1]
L Berg[3]
A DeCastro[1]
E Koo[4]
R Kotamarthi[5]
L Mazzaro[4]
E Quon[2]
J Sauer[1]
W Shaw[3]
D Allaerts[2]
M Churchfield[2]
C Draxl[2]
B Kosović
B Kravitz[3]
J Mirocha[6]
R Rai[3]
G Sever[5]

Prepared for
the U.S. Department of Energy
under Contract DE-AC05-76RL01830

Pacific Northwest National Laboratory
Richland, Washington 99352

[1] National Center for Atmospheric Research (NCAR)
[2] National Renewable Energy Laboratory (NREL)
[3] Pacific Northwest National Laboratory (PNNL)
[4] Los Alamos National Laboratory (LANL)
[5] Argonne National Laboratory (ANL)
[6] Lawrence Livermore National Laboratory (LLNL)

Executive Summary

The goal of the Mesoscale-to-Microscale Coupling (MMC) project is to build new high-performance-computing-based multiscale wind-plant simulation tools that couple a broad range of scales to enable the optimization of wind plants to ensure the efficient, reliable production and integration of future wind-generated electricity. To meet this goal, the project seeks to create, assess, and validate state-of-the-science atmospheric simulation methodologies to incorporate important mesoscale flow characteristics into microscale wind-plant simulations.

The fourth year of the project (fiscal year 2018 [FY18]) focused on:

- documenting and assessing the impacts of modeling at the mesoscale;
- assessing methods of initiating turbulence in microscale simulations;
- exploring methods to better represent the near-surface physics;
- evaluating the turbulence statistics for coupled model case studies in flat and in complex terrain.

The team conducted a rigorous analysis of the impact of modeling in the *terra incognita* on the microscale simulations, finding that 1) the upper range of the *terra incognita* is roughly the current depth of the boundary layer, 2) using higher resolution for the mesoscale model will produce a smaller fetch distance in a microscale simulation that will thus contain more turbulent kinetic energy, 3) use of the Lilly turbulence model on the microscale domain results in a higher level of turbulence than using the Mellor-Yamada-Nakanishi-Ninno (MYNN) or Yonsei University (YSU) mesoscale schemes, and 4) the microscale results do not vary with the type of turbulence model (PBL schemes or LES closure) used by its parent domain whose grid spacing falls within the *terra incognita*.

The team also put some effort into understanding how the mesoscale model setup impacts the microscale simulation, largely in the context of the Weather Research and Forecasting (WRF) model. A common issue is that to match the timing of nonstationary events, such as frontal passages, it must first be matched at the mesoscale if the microscale is expected to capture the phase well. That issue was studied for both complex and flat terrain cases. The team found that even when substituting different boundary conditions (replacing the Global Forecast System [GFS] with ERA-Interim), a phase shift persisted. The team also continued research begun during the Wind Forecast Improvement 2 project on testing a fully three-dimensional boundary-layer scheme.

Various methods of initializing turbulence at the microscale were tested and documented. Force perturbation methods were compared to the temperature perturbations methods tested in prior years and shown to yield an advantage with force perturbations leading to faster turbulence development. The team examined application of the stochastic cell-perturbation method (SCPM) to improve the turbulence equilibration process under mesh refinement within a turbulence-resolving simulation. Although the inflow contains turbulence, a significant distance is still required for the flow and turbulence field to equilibrate to the finer mesh spacing at the microscale. This study highlighted the flexibility of the SCPM to improve this application, showing that application of the perturbations to the velocities, rather than the potential temperature, and using smaller perturbation cells sizes, can improve the coarse-to-fine LES equilibration process. This study also highlighted the potential for generalization of the method to a broader range of downscaling applications, including adaptive mesh refinement.

Both the Veers and Mann methods of initializing turbulence at the inflow boundary were tested and found to be effective at generating turbulence at the microscale, with better results with more frequent updates. A library method using period precursor runs was also tested. Finally, a generalized boundary condition

with velocity perturbations from TurbSim was superimposed on WRF-derived inflow. This method was effective at spinning up turbulence, although not as quickly as preferred, and shows promise for expediting the workflow of a coupled simulation.

Two methods were studied to derive surface fluxes for the microscale model, one using the full land surface model of WRF and a second that derives a spatially averaged, yet temporally varying surface flux. The statistics of the two approaches are quite similar, and the latter method may be a simpler way to supply WRF surface fluxes to SOWFA or Nalu. A pseudo-canopy model that applies drag terms to the momentum equations over a specified depth was shown to improve upon the standard application of Monin-Obukhov Similarity Theory.

The MMC team continued to develop, test, and evaluate several techniques to couple the mesoscale to the microscale. A first basic technique is nesting from WRF run in mesoscale mode into the WRF-LES mode, which we call the concurrent online approach. This online approach was also used to study a frontal passage case for the WFIP 2 site. Using rather large grid refinement ratios of 9 between the nested and parent domains to skip over the *terra incognita*, the WRF simulation was able to capture the changes in the flow due to the frontal passage in terms of changes in wind speed, temperature, and turbulent kinetic energy, but the timing of the passage was incorrect (in the mesoscale as well as the microscale). The turbulent kinetic energy was higher than observed, and the team continues to investigate this feature.

The team also studied offline coupling between WRF-mesoscale model simulations and SOWFA as a proxy for Nalu, a new microscale solver being developed with U.S. Department of Energy (DOE) support. Two methods to integrate the mesoscale influence into the microscale solver were assessed for flat terrain (the SWiFT site) - 1) applying the large-scale advective and pressure-gradient terms extracted from the mesoscale simulation to the governing equations of the microscale solver, and 2) assimilating the mesoscale time-height history of mean wind velocity and potential temperature to generate microscale source terms. The domain was treated as flat and periodic, so turbulence naturally forms without the need for boundary perturbations. Both methods showed success at forcing the mean quantities of wind speed and direction. The turbulence intensity was overpredicted by the assimilation approach, however. For complex terrain, the team tested WRF-derived velocity, temperature, and surface sensible heat flux and skin temperature time series as boundary forcing for SOWFA. Four issues arose that the team has been working through: 1) mismatch in terrain resolution between the mesoscale and microscale simulation, for which some preliminary solutions have been tested with success, 2) the need for terrain-generalized inflow perturbations, which is under study, 3) boundary conditions of mixed inflow and outflow on a single boundary, which has been successfully addressed by using mixed boundary conditions (Dirichlet and Neumann), and 4) generation of spurious gravity waves at inflow regions, which is under study.

The MMC continues to work collaboratively and has determined strategies to work through the remaining issues required to optimally provide coupled model simulations. These simulations are expected to provide the wind industry new tools that can be used in the planning, design, layout, and optimization of wind plants, thus facilitating deploying higher capacities of wind generation.

Contents

Figures

Tables

1.0 Introduction

1.1 Purpose of the Mesoscale-to-Microscale Coupling Project

The goal of the Mesoscale-to-Microscale Coupling (MMC) project is to build new high-performance-computing-based multiscale wind-plant simulation tools by coupling a broad range of scales that will enable the optimization of wind plants thereby ensuring the efficient, reliable production and integration of wind-generated electricity.

The overarching objective of the project is to create, assess, and validate state-of-the-science atmospheric simulation methodologies to incorporate important mesoscale flow characteristics into microscale wind-plant simulations. To achieve this overall objective, project objectives include the following:

- Compare the abilities of existing full-physics models to fully characterize the meso/micro planetary boundary-layer (PBL) characteristics, including plant inflows, wake flows, and interactions with the boundaries. Identified deficiencies will provide the rationale for the next steps for model improvement.
- Establish baseline cases from existing field studies as part of the verification and validation process for existing models. Thus, improvements can be grounded in data.
- Downselect from the existing modeling suite for future implementation to improve development efficiencies using a common high-fidelity modeling (HFM) framework. This process will enable development of a tool that is usable by industry.
- Establish research and development requirements to improve PBL model performance. This initiative will identify specific areas for improvement and how they will affect the microscale modeling initiative in the HFM environment.
- Advance development issues including nonstationarity, boundary interactions, coupling strategies, *terra incognita* issues, modeling in complex terrain, and beyond.
- Transition existing model and physics requirements to the HFM development environment, working closely with the High-Fidelity Modeling team.

Realizing these objectives will enable simulation of the full suite of mesoscale and microscale flow characteristics affecting turbine and wind-plant uncertainties and performance, thereby allowing for substantive improvements in wind-plant design, operation, and performance projections. Figure 1.1 diagrams the MMC approach to the project, taking into account the objectives described above.

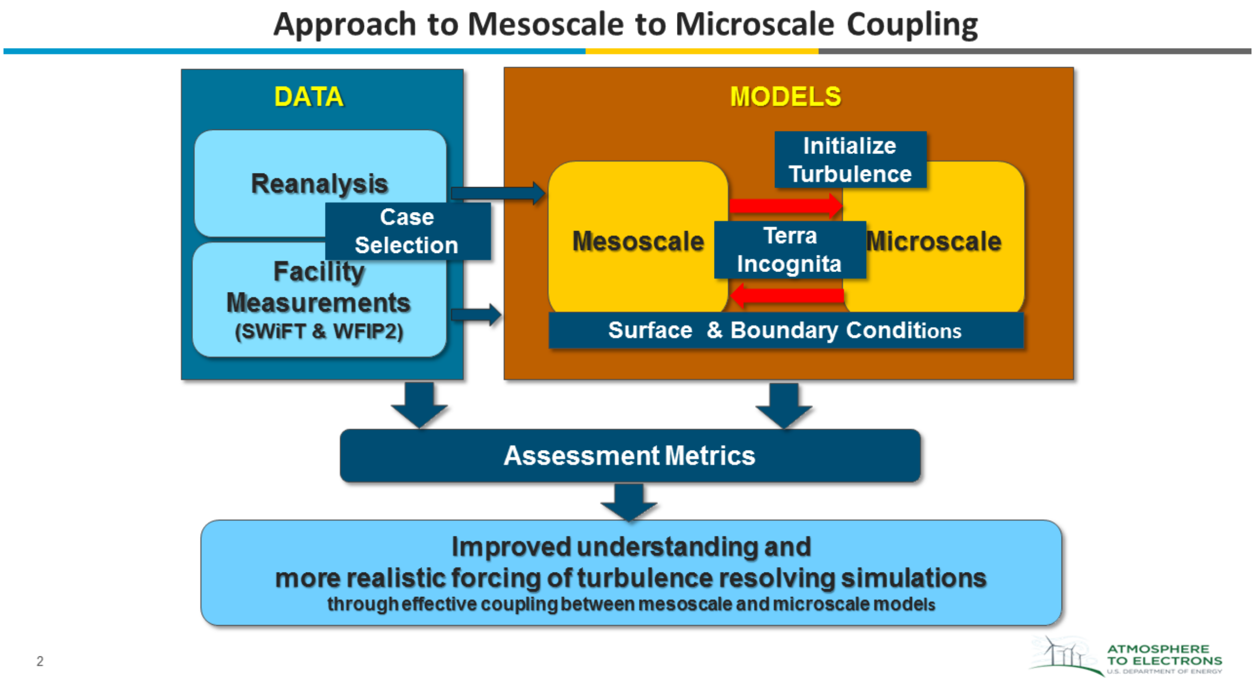

Figure 1.1. Diagram of the MMC project approach.

1.2 MMC Project Context within the Atmosphere to Electrons Initiative

The Atmosphere to Electrons (A2e) initiative is an effort within the U.S. Department of Energy's (DOE's) Energy Efficiency and Renewable Energy Office, Wind Energy Technologies Office, whose goal is to optimize power production from wind plants as a whole. To that end, the initiative is explicitly integrating advances in atmospheric sciences, wind-plant aerodynamics, and wind-plant control technologies, taking advantage of current and emerging capabilities for high-performance computing. Because atmospheric inflow is the fuel that powers wind plants, the development and validation of first-principles based, high-fidelity physics models within an opensource simulation environment has been identified as a crucial part of A2e science goals and objectives. Furthermore, there has been an overwhelming consensus within the research community that these models must be developed and systematically validated using a formal verification and validation (V&V) process. The MMC project is a joint collaborative project between six DOE national laboratories, with National Center for Atmospheric Research (NCAR) leadership as a formal subcontractor, and incorporating external feedback from A2e Initiative team members, the merit review panel, industry, DOE leadership, and other stakeholders.

The MMC project is grounded in data provided by other A2e facilities and projects. For the first two years, the data have included measurements taken at the DOE/Sandia National Laboratory Scaled Wind Farm Test (SWiFT) facility in West Texas. The MMC modeling has helped characterize and inform the wake dynamics experiments being accomplished at that site, and its results are expected to contribute to modeling wake dynamics.

In years 3 and 4, the MMC project has focused on coupled modeling in complex terrain, using data derived from observations taken in the Pacific Northwest as part of the A2e project, Wind Forecasting Improvement Project 2 (WFIP 2). Including mesoscale forcing in microscale models will also become critical to the success of the A2e project when focusing on wind-plant controls. Most prominently, the very specific coupling and modeling philosophies and technologies being developed by the MMC project are necessary for building the high-fidelity modeling tools. The results of MMC modeling and case studies are being archived in DOE's Data Archive and Portal (DAP).

1.3 Progression of the MMC Project

The MMC project was designed to systematically progress from simulation of canonical quasi-steady cases through the full complexity of nonstationarity and complex terrain. The plans are grounded in V&V based on comparing model cases to observations. Specifically, the plans for the first four years (beginning in March 2015) of the project were as follows:

- **FY15:** Couple mesoscale-to-microscale models for canonical steady flow conditions to include neutral, stable, and convective conditions for flat terrain and compare simulations to SWiFT site measurements.
- **FY16**: Couple mesoscale-to-microscale models for nonstationary conditions, also for a flat terrain site; devise coupling strategies in which mesoscale forcing causes microscale models to follow through the temporal changes; and compare to SWiFT site measurements of winds and turbulence.
- **FY17:** Couple mesoscale-to-microscale models for representative meteorological conditions occurring over a complex terrain site, where mesoscale forcing causes microscale models to follow through the temporal changes and compare to WFIP 2 site measurements.
- **FY18:** Refined testing, assessment, and uncertainty quantification of coupling methodologies, impact of the *terra incognita*, turbulence initiation techniques, and integrating boundary and surface conditions for both flat and complex terrain comparing to data from both the SWiFT and WFIP 2 sites.

In the first three years several mesoscale and microscale models were assessed. Downselection of the computational solvers for use in the HFM environment was accomplished: the mesoscale model will be the Weather Research and Forecasting (WRF) model and the microscale model will be the Nalu model.

During each of the four project years, four specific objectives have been addressed, i.e., (1) to define V&V procedures and benchmarks, (2) to develop and assess microscale turbulence-generation methods, (3) to assess current surface-layer and boundary-layer parameterizations, and (4) to develop and assess approaches for coupling mesoscale models to microscale models.

Beyond fiscal year 2018 (FY18), the MMC project team will continue to

- add complexity,
- explicitly compare microscale simulations with and without mesoscale forcing focusing on metrics important to wind plan operation,
- feedback findings into low-order models that can be used rapidly by industry,
- improve turbulence models for industry,
- work with the HFM team to provide fast mesoscale modeling capabilities and couple them to the Nalu model,
- test the methods in the offshore environment,
- and feed the results into other A2e projects including wakes, controls, and others.

1.4 Expected Impacts on Industry

The expected impact of the MMC project is to advance the science and engineering of coupled mesoscale-microscale modeling in order to provide industry with more advanced wind-plant optimization capabilities. Industry stakeholders have made it clear what must be done in terms of better modeling of power output. This issue is complex and involves many factors beyond applying a simple power curve to a simulated mean wind speed and making small adjustments for turbulence. Uncertainties come from many different aspects of the coupling, including interannual variability due to longer-term climatic variability, variability in the coarser scales that are resolved by the mesoscale models, variability due to wake effects, inner variability due to the heterogeneity within the wind plant, variability due to coherent structures such as mountain wakes, inherent uncertainty due to the chaotic nature of turbulent flow, and finally impacts through the surface-layer treatment and its interactions with characteristics of the underlying surface. The MMC project addresses these issues directly and, over the course of the multiyear project, will be able to provide specific guidance and tools to industry. The MMC team developed Table 1.1 as a list of uses of the MMC approach, the stakeholder(s), quantities and metrics to assess for each use, and the type of uncertainty analysis that will affect power output.

Both the improved computational methodologies and the knowledge gained through their assessment and validation will enable substantive improvements in wind-plant design, operation, and performance projections, all of which are required to attract continued investment in wind power as a viable means of meeting national goals of mitigating climate change and establishing energy independence.

The successful outcome of the MMC project will result in improved computer simulation capability that accurately incorporates the impact of mesoscale weather on wind power plant performance. Meeting this goal will require microscale simulations driven by realistic mesoscale forcing, knowledge of when the additional complexity of mesoscale coupling is beneficial, and recommendations for best practices for modeling across spatial and temporal scales. Over the course of this project, the tools and knowledge developed during each phase, outlined above, will continue to be made available to industry and the broader research community.

The MMC team has engaged with industry by participating in the first-year workshop held in September 2015 at NCAR, at which industry representatives were invited to comment on the approach and the results as well as to suggest changes. In FY16, the MMC team conducted an industry survey. During FY17, the team conducted a first telecom with industry to inform them of our progress and solicit input. During FY18, several more telecoms with industry demonstrated industry’s interest in the team’s research results.

MMC team members have also been actively engaged in organizing major wind industry conferences that were used as forums for bringing the research community together with industry during FY18. This was successfully accomplished at WindTech 2017 held in Boulder, Colorado, in October 2017 (organized and led by team members); at the International Conference on Energy and Meteorology held in Shanghai, China in June 2017; at the American Meteorological Society (AMS) Boundary Layer and Turbulence Conference in Oklahoma City, Oklahoma in June 2018; at the Ninth Conference on Weather, Climate, and the New Energy Economy held as part of the AMS Annual Meeting; and at the Torque Conference in Milano, Italy in July 2018. All of these meetings included presentations about the MMC project and afforded ample opportunity for industry representatives and team members to discuss the team’s progress and plans.

Table 1.1. Assessment of stakeholder use and assessment strategies to determine if MMC modeling provides useful information for that use.

MMC Use	Stakeholder	Quantity to Measure	Metrics	Uncertainty Analysis for Power Curve
Basic understanding of physics	Scientists, Engineers	Current list plus elevated structures	Current list plus below	Ensembles—physics, initial and boundary conditions
Micrositing	Developers, Contractors, Manufacturers	Binned wind speed, spectra, spatial variability	Probability structures and spatial correlations	Distributions, correlations, spatial correlations, covariance
Turbine siting	Developers, Contractors, Manufacturers	Binned wind speed, spectra, spatial variability	Probability structures and spatial correlations	Distributions, correlations, spatial correlations, covariance
Turbine reliability and design plus forensics		Turbine statistics, shear, coherent structures	Correlated structures to loads	Distribution extremes, wind direction variability
Operations and managements, controls, loads		Slow variations, event variations, binned wind speed, accurate turbulence statistics plus characterization of structures	Use spatial and temporal filters	Time-dependent statistics and variability
Inform low-order models: mass conserving models, Reynolds- averaged Navier-Stokes	Developers, contractors, OEMS	Three-dimensional wind speed, tke, and surface fluxes	Spatial correlations	All

As described in more detail in the sections that follow, each of the models and techniques we used are validated against a range of metrics to determine their accuracy for a mix of wind-energy-related applications. A key outcome of this project is concrete guidance to both industry and research communities regarding the potential strengths and weaknesses of various MMC approaches. Additionally, the best performing of the approaches assessed will be incorporated into the A2e High-Performance Modeling (HPM) environment for future design and testing. A set of metrics defined by the project continues to be refined further as the project progresses into additional realms of modeling.

1.5 Background and Motivation

This work is motivated by the fact that the current generation of tools is insufficient to adequately simulate winds and turbulence on all of the atmospheric scales that drive wind-plant performance. This project has brought together a team of subject-matter experts to address these modeling gaps. It is widely reported that many wind plants in complex operating environments continue to underperform by 30–40% relative to annual production estimates. According to a survey conducted by AWS Truepower, LLC (Bailey 2013), the three largest factors contributing to performance losses, as well as four of the eight uncertainty sources, are affected by the quality of the numerical simulation tools used for turbine and wind-plant performance estimates.

A significant fraction of wind-plant underperformance and uncertainty can be attributed to design, siting, and operational strategies based upon inaccurate assessment of environmental conditions, as well as underestimation of the importance of environmental (mesoscale) influences on the environment in which wind turbines operate. Wind turbine design, plant construction, and operations all rely on a suite of simulation design tools of varying levels of complexity and fidelity, each targeting different phases of wind-energy planning, deployment, and production. These computational tools span a range of applications including flow characterization, power production, fatigue loading, wake effects, and the impacts of complex terrain (e.g., Shaw et al. 2009).

Crucially, these tools all suffer from the inability to adequately address the impacts of the complexity of the mesoscale flow and the physical understanding and modeling of the weather phenomena that strongly influence turbine operation (Sanderse et al. 2011; Troldborg et al. 2011; Mehta 2014). While recent advances have been made in the engineering models used to estimate wakes and loads, and to examine control strategies to improve plant production or mitigate fatigue (e.g., the National Renewable Energy Laboratory's [NREL's] Simulator fOr Wind Farm Applications [SOWFA] and Fatigue, Aerodynamics, Structures, and Turbulence [FAST] toolkits; Los Alamos National Laboratory's [LANL's] WindBlade model), the applicability of these models to real-world turbine operations is limited by the low fidelity of the atmospheric flow fields represented within their simulation frameworks. Further rationale and details of the needs are described in the reports documenting the results of the first-, second-, and third-year efforts of the MMC team (Haupt et al. 2015, 2017, 2018).

One difficulty with MMC is that it bridges a wide span in spatial and temporal scales. Mesoscale models were designed for horizontal resolutions on the order of kilometers with time scales ranging from days to hours. Microscale models have resolutions on the order multi-meters (i.e., from 10 m down to a couple meters is common), depending on the atmospheric stability and desired resolution, and they resolve time scales ranging from hours to seconds. Spanning these scales involves resolving a wide range of disparate phenomena and turbulence that have different fundamental characteristics.

Examples of wind-energy applications benefiting from MMC include single wind turbine loads, power, and controls estimation (by creating more realistic microscale inflow under a variety of conditions for turbine simulators); wind-plant siting (by providing more site-specific inflow profiles under the full diurnal cycle in different seasons or terrain-induced flow behavior); wind-plant power forecasting and operation (through higher resolution wind-plant-local forecasting); wind-plant-level control system design (by testing these controls under more realistic mesoscale-forced situations rather than just applying simple canonical cases); and wake modeling (through microscale wake simulations in more realistic situations than the canonical ones). All such applications have differing needs for representations of the microscale. For example, it is possible that for load analysis the primary factor is employing more realistic mean wind profiles forced by the mesoscale as opposed to the power or log-law typically used today. Having site-specific profiles from different times of day and different types of common mesoscale-driven events could greatly improve load calculations. On the other hand, performing forensics to determine why certain turbines failed during a mesoscale weather event will likely require a sophisticated mesoscale-microscale coupled simulation. Wind-plant controls experts have been requesting more realistic mesoscale-forced microscale inflow to study because they realize that canonical microscale inflow may not rigorously exercise their control systems. Some industry experts note that the current frameworks are not sufficient. This MMC project is directly addressing these known deficiencies common to industry research and design tools by assessing and validating mesoscale-microscale coupling strategies.

Thus, MMC is a key enabling technology required for the replacement of many of the inadequate idealizations and simplifications limiting the applicability of current microscale simulation tools. MMC will replace them with environmental forcing obtained from mesoscale simulations. Incorporation of these important environmental drivers will enable simulation of critical microscale flow characteristics that affect turbine and wind-plant performance and uncertainties.

1.6 Report Contents and Organization

The remainder of this report provides detailed documentation of the results of the MMC project's fourth-year effort. The performance metrics were defined at the beginning of the project and updated as needed for these complex terrain cases to assess the phenomena mentioned above. The need for uncertainty quantification has been an intentional part of the metrics development and plans for model runs in the future.

Chapter 2 documents the benchmark cases studied during FY18, and Chapter 3 describes the methods planned for assessment and uncertainty quantification. The results of mesoscale modeling are reported in Chapter 4, and the impact of the *terra incognita* is documented in Chapter 5. Chapter 6 reports on findings regarding generating turbulence in the microscale simulations for both flat and complex terrain cases. Improvements in near-surface physics are described in Chapter 7. Chapter 8 compares model coupling techniques. Chapter 9 synthesizes the results and their expected impact. Appendix A lists the team's FY18 contributions to the peer-reviewed literature and conference papers presented. Appendix B details each lab's contributions to the FY18 efforts.

2.0 Benchmark Cases

As seen in Section 1, the MMC project seeks to improve models through assessing their capabilities for reproducing the specific characteristics of particular case days. During FY18, the team looked at advances in both complex terrain cases and in nonstationary flat terrain cases. The case days are described below.

2.1 Complex Terrain Cases

One driver of complex flow is complex terrain and proximity to a land/water interface. The Pacific Northwest portion of the United States includes both and is a rich source of complex atmospheric phenomena. The Wind Forecasting Improvement Project 2 (WFIP 2) provides instances of very interesting atmospheric phenomena, including westerly flow with topographic wakes and mountain waves forced by Mt. Hood. Other atmospheric phenomena include easterly gap flow, cold pools to the east of Mt. Hood and their breakup, and frontal passages that are impacted by these interesting terrain features.

2.1.1 Waves and Wakes – November 21, 2016 WFIP 2 Site

The November 21 case includes a wake in the lee of Mt. Hood during the period from 19:00–23:00 UTC, which may or may not have affected the Wasco site. The mesoscale simulations from this case were initially analyzed as part of Section 2 of the FY17 MMC Annual Report (Haupt et al. 2018) and in the microscale as part of the microscale turbulence evaluation in Section 5 of that report.

Preliminary results from mesoscale simulations performed for November 21, 2016 with westerly flow over Mt. Hood and associated orographic wakes. In addition, waves are also seen in the flow field of HRRR's finer resolution (750 m) simulation. These findings suggest that the presence of Mt. Hood and its associated wake could affect the results of the simulations on the microscale domain, which is located approximately 100 km northeast of Mt. Hood. To investigate this, a coupled simulation (WRF-LES) was performed for the conditions of westerly winds on November 21, 2016.

2.1.2 Frontal Passage

Based on the WFIP 2 Event log, few days with frontal passages were selected in the WFIP 2 region. A representative day (November 15, 2016) was chosen using the composite maps of satellite data and surface weather as well as profiler data and NOAA's HRRR model output for the region.

The results from mesoscale simulations using initial and boundary conditions derived from two reanalysis products—NARR and GFS—were compared. Figure 2.1 displays simulated wind speed and direction using forcing from these two reanalysis products. The vertical profiles of wind velocity and temperature were saved every 10 seconds at a location above the WFIP 2 Physics Site. At lower altitude (up to 600 m), the result shows that the wind direction changes around 0900 PST for WRF simulations completed using the NARR boundary forcing, whereas its frontal passage occurs earlier, near 0800 PST, using GFS boundary forcing. The potential temperature follows a consistent pattern (not shown) that also starts to drop when the wind direction changes. These results highlight the uncertainty in the timing of important meteorological phenomena.

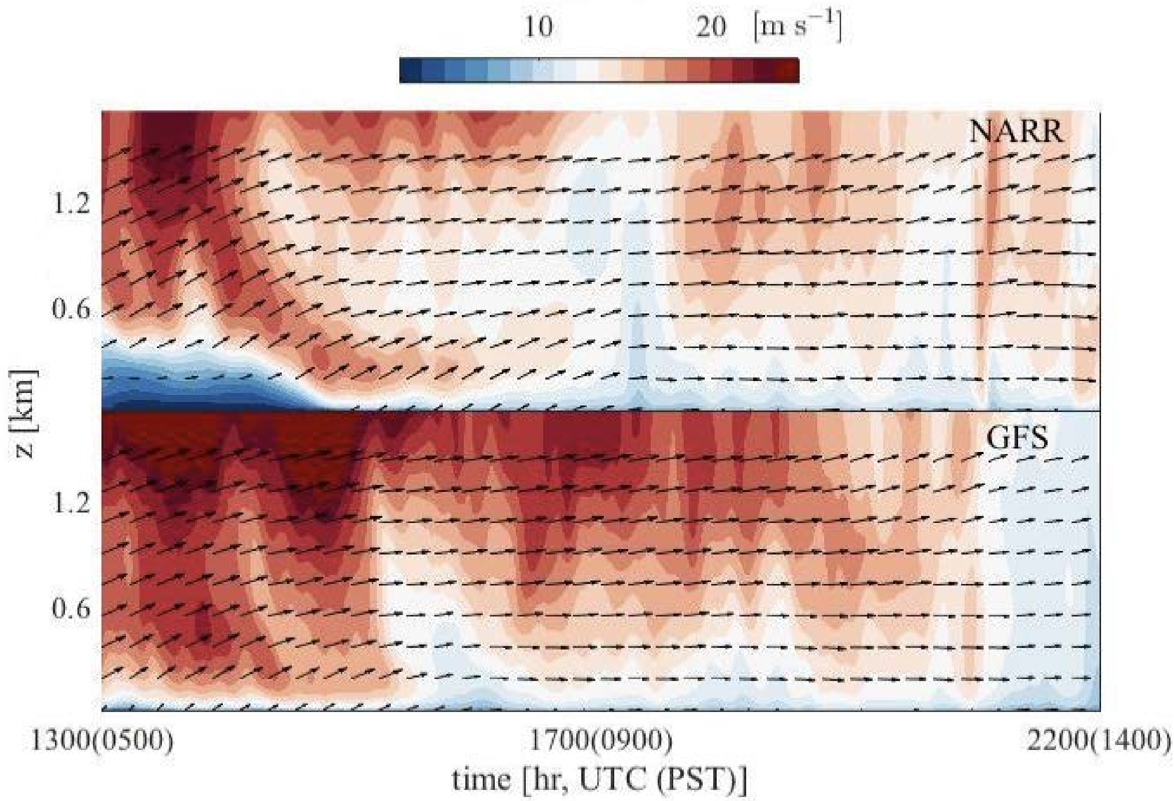

Figure 2.1. Wind speed and direction predicted using two reanalysis products – NARR (top) and GFS (bottom).

Two microscale domains were nested inside the mesoscale domain that used initial and boundary conditions from the NARR. The simulation was performed using concurrent online coupling starting from 09:00 UTC and was run for 12 hours. To initialize the turbulence properly near the inflow boundary, temperature perturbations were applied at the boundary of the microscale domain. The flow field from the third domain with horizontal grid spacing of 30 m was used for the analyses. Figure 2.2 (top) shows the time-height cross-section of the simulated wind speed and direction. The magnitude of wind speed and wind direction changes slightly compared to the results from mesoscale simulation (Figure 2.1, top). The potential temperature (Figure 2.2, bottom) decreases around 0900 PST corresponding with the frontal passage. The simulation results from the microscale domain highlights the transient nature of the meteorological condition during events like frontal passage.

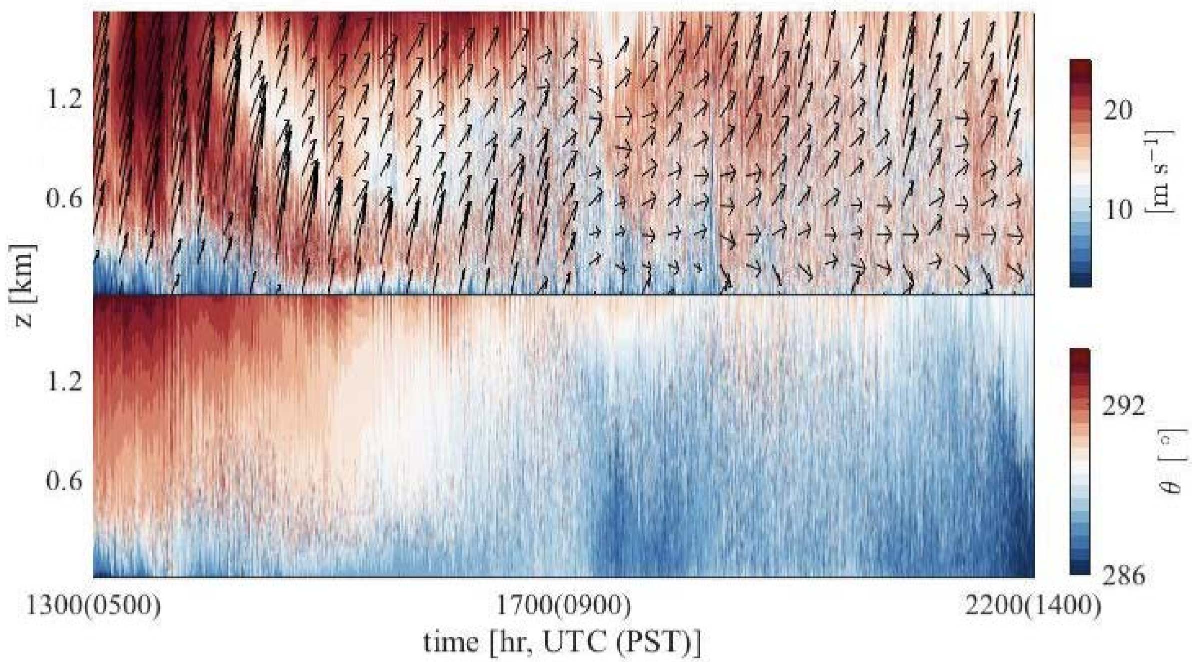

Figure 2.2. Wind speed and wind direction (top), and potential temperature (bottom) predicted by WRF/WRF-LES simulation.

2.2 Canonical Diurnal Case in Flat Terrain – Nov. 8, 2013 SWiFT Site

In order to assess the ability of the coupled models to capture more canonical diurnal changes as one progresses through a typical day, it is convenient to use data from a flat terrain site. To that end, the team has considered a case day from measurements taken at the DOE/SNL SWiFT facility in West Texas. The SWiFT site was chosen for to its flat terrain, relevance to wind energy installations in the U.S., and because of the adjacent atmospheric measurement facilities hosted by Texas Tech University's (TTU) National Wind Institute (NWI). More details of the SWiFT site are documented in the team's Year 2 report (Haupt et al. 2016) and in SNL's report regarding that site (Kelley and Ellis 2016).

The team selected November 8, 2013 as the primary diurnal cycle case to model because it represents a quiescent day that includes typical morning and evening transitions and makes a good first test case with common conditions that are important for wind energy. This is the same day studied earlier in the Year 2 report. The 1-hour, near-neutral transition is centered around 22:30 UTC, with profiles shown in Figure 2.3. The diurnal cycle, convective-neutral-stable atmospheric transition, is shown for the 24 hours centered on the near-neutral transition in Figure 2.4.

This period was marked by strong southwesterly winds over the west Texas panhandle and generally clear conditions (Figure 2.5). Data from the TTU Radar Wind Profiler (RWP) operated at the SWiFT site shows that the winds at the lowest altitudes are consistently south-southwesterly over the course of the day (Figure 2.6).

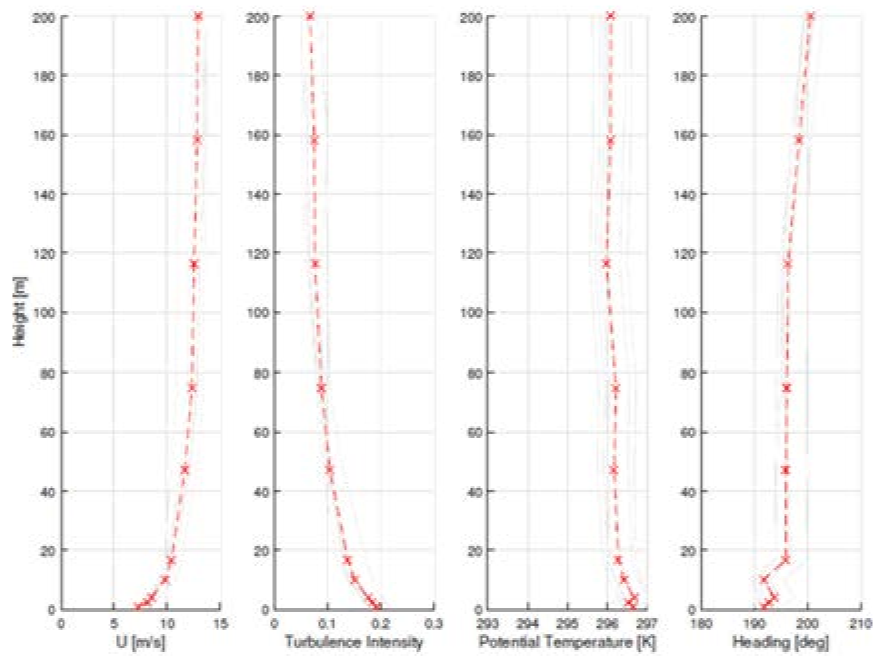

Figure 2.3. November 8-9, 2013 Near-neutral transition profiles (gray profiles are for the 10-min. averages, red profile is the 1-hour average).

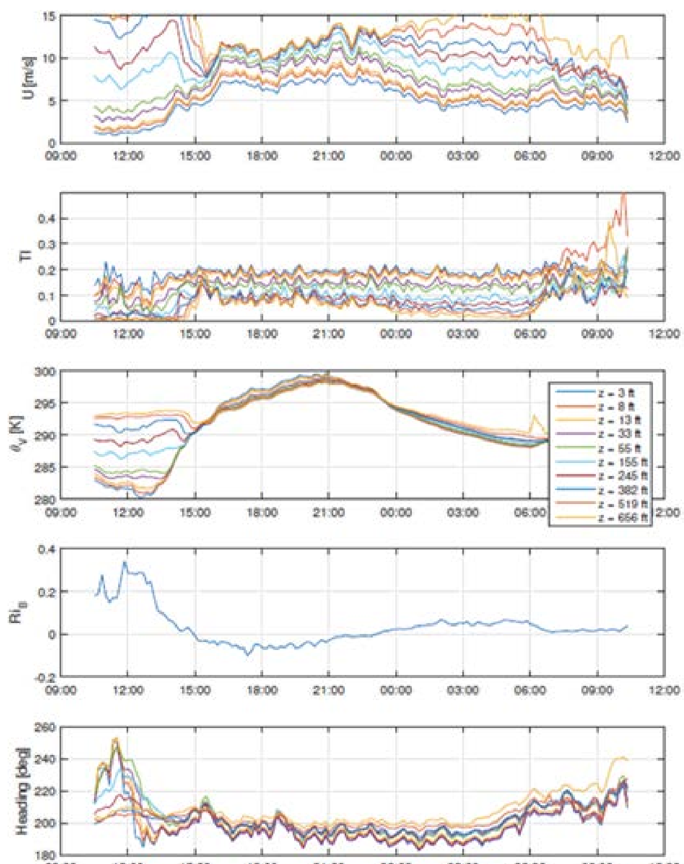

Figure 2.4. November 8-9, 2013 diurnal cycle time history.

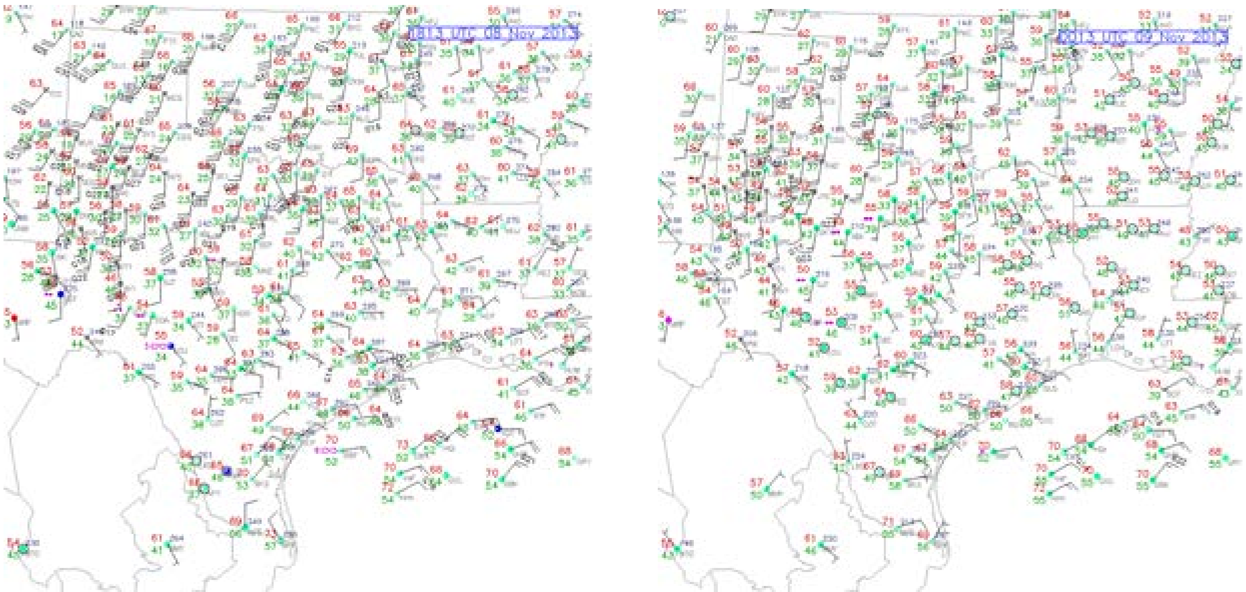

Figure 2.5. Surface weather map valid at 18:13 UTC (12:13 CST) on November 8, 2013 (left) and 00:13 UTC (18:13 CST) on November 9, 2013 (right).

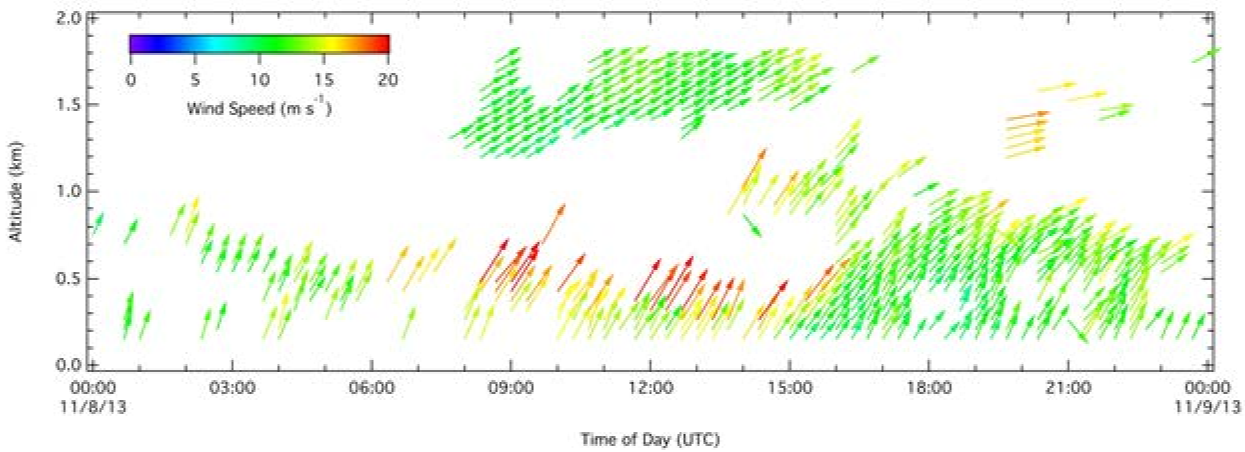

Figure 2.6. Time-height cross-section of wind speed and wind direction measured at the TTU RWP for November 8, 2013.

3.0 Plan for Assessment and Uncertainty Quantification

The MMC project is grounded in rigorous assessment based on data collected in DOE-funded experiments and facilities. This chapter describes the methods planned for this assessment.

3.1 Mesoscale Assessment

One set of mesoscale results from the frontal passage case were submitted for evaluation during fiscal year 2018. The results were from a simulation of 13:00 – 23:00 (UTC) November 15, 2016 at the WFIP 2 site, with a grid spacing of 1215 m and hourly output.

Observations were collected from six sodar sensors (AON), eight Bonneville Power Administration (BPA) sites, and four surface meteorological stations (MET) for comparison against model output. Sensor locations can be seen in the map below, and a brief description of each sensor is listed in Table 3.1 following. Although there are several other sensors at the WFIP 2 Physics site, observational data sets were chosen based on data availability (with respect to date, time, and variable), as well as spatial distribution.

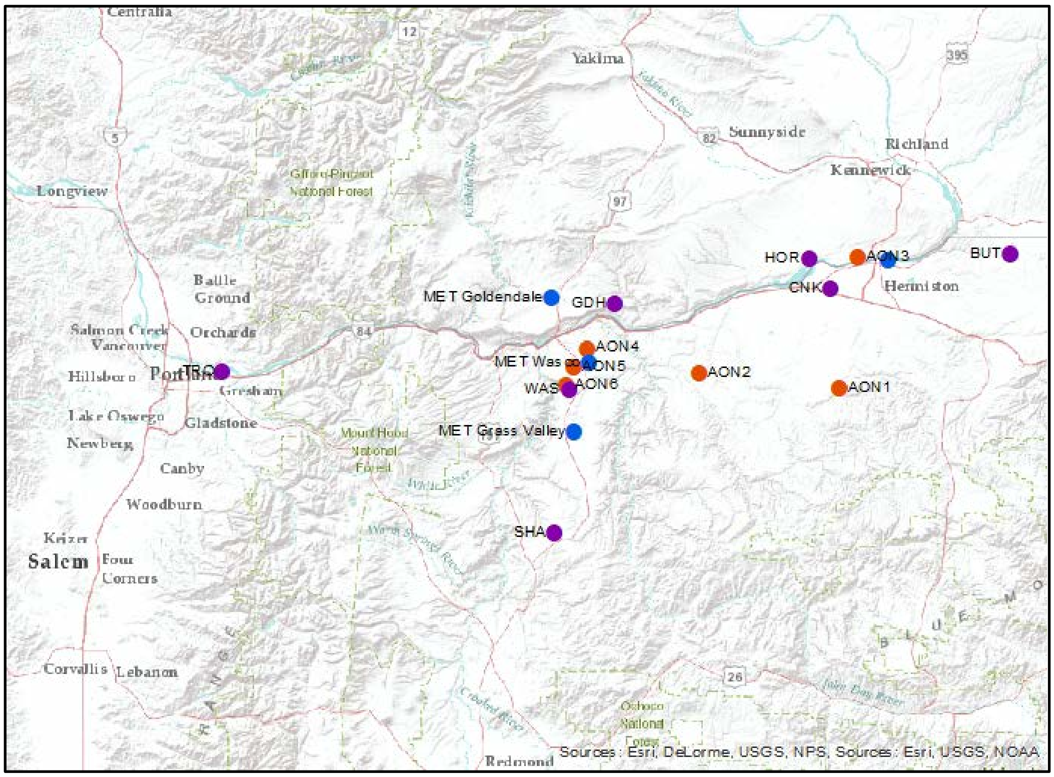

Figure 3.1. Map of the WFIP 2 site with observation data source locations (AON in red, BPA in purple, MET in blue).

Before comparison with model results, observational data were inspected for evidence of a frontal passage. Observations show that this feature occurred between 13:00 – 19:00 (UTC) over the spatial distance between the sensors. Both the observational data and the model data were subset to this time window to highlight model performance with specific regard to the frontal passage.

Observations from the six sodar stations are used to assess model output for wind speed and wind direction, and observations from the four MET stations and eight BPA stations are used to assess model output for potential temperature. Summary statistics—including mean error, mean absolute error, root mean squared error, and correlation coefficient—are given for each set of observation data and model output.

Table 3.1. List of instruments and their location.

Data Source	Name in Map	Latitude	Longitude	Elevation (m)
sodar	AON1	45.50483	-119.49102	696
sodar	AON2	45.55357	-120.15554	356
sodar	AON3	45.93761	-119.40594	112
sodar	AON4	45.63742	-120.67993	428
sodar	AON5	45.57451	-120.74734	450
sodar	AON6	45.51586	-120.78069	727
Surface Met	MET Umatilla	45.9278	-119.2651	150
Surface Met	MET Grass Valley	45.362	-120.7456	708
Surface Met	MET Goldendale	45.80552	-120.84861	502
Surface Met	MET Wasco	45.59011	-120.67193	456
BPA Tower	GDH	45.78336	-120.55023	748
BPA Tower	BUT	45.95008	-118.68341	545
BPA Tower	WAS	45.50026	-120.76687	642
BPA Tower	CNK	45.83334	-119.53361	122
BPA Tower	HOR	45.93377	-119.63422	149
BPA Tower	SHA	45.02515	-120.83532	1115
BPA Tower	TIL	45.45772	-123.82864	19
BPA Tower	TRO	45.55832	-122.40173	37

3.2 Microscale Assessment

The assessment of mesoscale-to-microscale coupling focuses on the effectiveness of rapid development of a fully developed turbulent flow on the microscale domain driven by a mesoscale simulation. The assessment of different approaches is proceeding as the simulation data are being shared with NCAR's team.

In mesoscale simulations turbulence is not resolved, but fully parameterized; therefore, in coupled simulations the inflow to a microscale simulation is smooth. Turbulence development in a microscale simulation driven by a mesoscale forcing is not guaranteed. To ensure effective turbulence development, the project team developed several approaches including inflow perturbation, synthetic turbulence inflow, and a precomputed library of turbulent flows. Several inflow perturbation approaches have been explored including: potential temperature perturbation, perturbation of velocity components, or combined potential temperature and velocity perturbations. Synthetic turbulence approaches are based on Veers (1988) and Mann (1998) methods of creating three-dimensional velocity fields with energy spectra characteristic for atmospheric boundary-layer (ABL) flows.

It has been shown by Muñoz-Esparza et al. (2018) that under different atmospheric stability conditions the requirements for turbulence development are different. Therefore, to provide a comprehensive assessment of the approaches to turbulence development selected assessment cases include a range of stability conditions: stably stratified, neutral, and convective ABL flows. For the purpose of assessment a set of three cases related to observations at the SWiFT tower on November 8 and 9, 2013, are being simulated using the WRF and SOWFA models. The simulations will specify a large-scale pressure gradient and a potential temperature profile on an outer, mesoscale domain, while an inner, large-eddy simulation domain of the size 4.33 km by 4.33 km is resolved using 433x433 grid cells with 10 m grid cell size. More details about the simulation set up are provided in Table 3.2.

In order to enable objective assessment of different approaches to turbulence generation two-hour time series output from WRF or SOWFA at a frequency of 1 Hz on a 10x10 grid of grid cells/points is used. The locations where time series are recorded are: x = y = [255,505,755,1005,1505,2005,2505,3005,3503,4005] m (see Figure 3.2). Time series include the following variables: Cartesian coordinate of vertical levels (in WRF vertical levels are time dependent since WRF uses a pressure coordinate), velocity components, potential temperature, pressure, subgrid turbulent kinetic energy, subgrid stresses, subgrid vertical heat flux, surface friction velocity, and surface roughness. Such a grid of time series output provide sufficient information to assess how rapidly in the spatial sense these various approaches result in realistic, fully developed, three-dimensional turbulence. The assessment quantifies resolved turbulence based on computation of power spectra and cospectra of velocity components and potential temperature in addition to vertical profiles of wind speed and potential temperature. To assess how rapidly turbulence is developed and equilibrium state reached, spectra, cospectra, and vertical profiles are computed at different downstream locations and subsequently compared to equilibrium profiles. Equilibrium profiles are generated by spectra and cospectra computed from a reference LES simulation with prescribed periodic lateral boundary conditions.

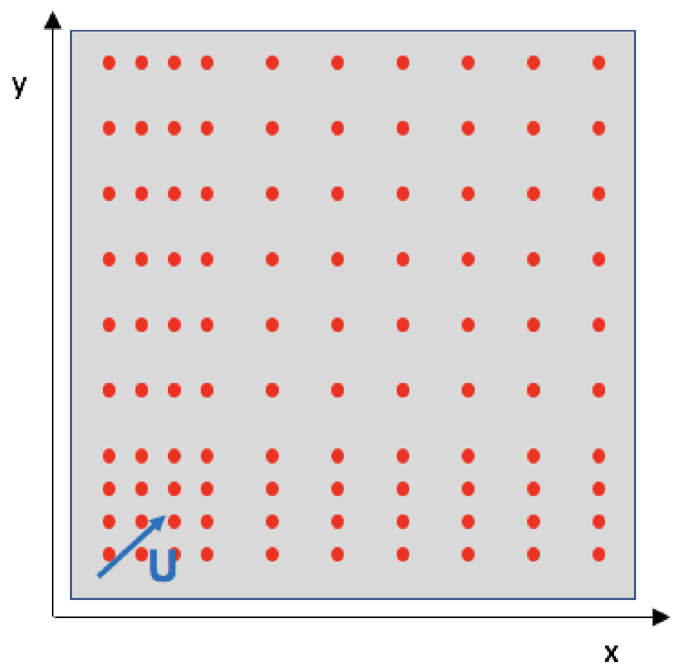

Figure 3.2. Distribution of locations where 1 Hz time series of velocity components, potential temperature, subgrid stress components, and subgrid vertical heat flux are recorded.

Table 3.2. Setup for canonical experiments of perturbation approaches for Nov. 8-9, 2014 at the SWiFT site.

<u>Quiescent Diurnal Cycle</u> Typical morning and evening transition				
Date	November 8-9, 2013			
	Convective (C)	11/08/2013: 20:00-22:00 UTC	Surface Heat Flux [K m s^{-1}]	0.17
	Neutral(N)	11/08/2013: 21:30-23:00 UTC		0.08
	Stable(S)	11/09/2013: 04:00-05:00 UTC		-0.015
Domains	Roughness	0.1 m		
	Latitude	33.61 deg (0.68661 rad)		
	Parent (Mesoscale) d01	Resolution	990 m	
		Dimensions Extents	[Nx,Ny,Nz] = [529,529,150] [Lx,Ly,Lz] = [523.7,523.7,3] km	
		Spin-up	1h (C), 2 (N)	
		Data Collection	Frequency	1 min
			Time Period	2h
		Vertical Levels	# of levels	150
	Nest #1 (LES) d02	Resolution	90 m	
		Dimensions Extents	[Nx,Ny,Nz] = [529,529,150] [Lx,Ly,Lz] = [47.6,47.6,3] km	
		Spin-up (after domain d01 spin-up)	2h (C), 2 (N)	
		Data Collection	Frequency	1 s
			Time Period	2h
	Nest #2 (LES) d03	Resolution	10 m	
		Dimensions Extents	[Nx,Ny,Nz] = [433,433,150] [Lx,Ly,Lz] = [4.3,4.3,3] km	
		Spin-up (after domain d02 spin-up)	2h (C), 2 (N)	
		Data Collection	Frequency	1 s
			Time Period	2h

3.3 Using Wind Plants for Assessment

For the past few years of the MMC project, we have been performing validation with atmospheric quantities of interest. These quantities include mean vertical profiles of velocity, temperature, turbulence statistics—along with turbulence spectra—and more. Validation using these quantities of interest is extremely valuable because MMC is an atmospheric flow problem.

Because the ultimate goal of the A2e MMC project is to apply MMC methods to the wind-plant problem, and we have been developing methods and validating with atmospheric quantities of interest for the past few years, now is an appropriate time to enhance our set of validation quantities of interest with wind-plant-specific quantities. In FY18, we began thinking about how to validate MMC methods using wind-plant-derived data, and our initial thoughts are summarized in NREL's FY18 Q1 milestone report, "Wind-Plant-Specific Validation Metrics, Quantities of Interest, and Benchmark Cases for Mesoscale-Microscale Coupling Validation." That report was meant as a starting point that will become more clearly defined as we practice actual validation using wind-plant data in the coming years. n this section, we summarize highlights of that report.

Wind-plant-centric quantities of interest include direct and indirect flow measurements. Direct flow measurements are those taken by meteorological masts often placed within wind plants. They can also include more sophisticated measurements taken by scanning lidar or scanning radar. These measurements not only capture the incoming atmospheric flow, but also wakes and how they respond to the atmospheric flow. This is an important point because wake response may be an indicator of how well mesoscale influences are captured. Indirect flow measurements are measurements recorded by the wind turbine's supervisory control and data acquisition (SCADA) system and load sensors placed on turbine components. These measurements include turbine power output, rotor speed, yaw angle, blade-root moments, and tower bending moments. Indirect measurements are especially interesting because they capture the turbine's response to the atmospheric inflow. They are akin to how a strain gauge or thermocouple works: these devices do not directly measure strain and temperature, but rather they often measure changes in electrical resistance in the measurement device, and a transfer function between voltage and strain or temperature is known beforehand. These indirect measurements can be used as an indicator of how well MMC is working.

Also interesting with wind-plant-centric measurements is the fact that the wind plant can be viewed as a sensor array spanning a large horizontal extent. If we think of the turbine response as an indirect measurement of the flow, then we can gather a time-resolved picture of how the flow is varying horizontally at the turbine height. This is especially valuable because mesoscale events often cause horizontal inhomogeneity, and it is rare that a field campaign would have sensors placed in the field with the same density and height as wind turbines. The two disadvantages to using turbines rather than direct flow sensors is that the transfer function between the flow quantities is not always known (i.e., there may be a way to correlate turbulence intensity to RMS turbine loads, but that is not straightforward), and the turbines disrupt the flow significantly with their wakes.

A last point for using wind-plant-centric data is that it often comes as time histories, just like direct atmospheric measurements. To perform meaningful validation, those time history data must be reduced in some way for two reasons. First, we cannot expect to match measured high-frequency time history data in simulations because turbulence causing the high-frequency component of the signal is stochastic. Rather, we can only expect to match statistics. Second, to perform rigorous validation, we must move beyond simply plotting time-history line plots of field data compared to simulated data and visually making an assessment. We must reduce the data such that we can have scalar numbers that give a measure of MMC performance. Such scalar numbers include root-mean-square error (RMSE), etc. This idea is captured in the flow chart shown below in Figure 3.3.

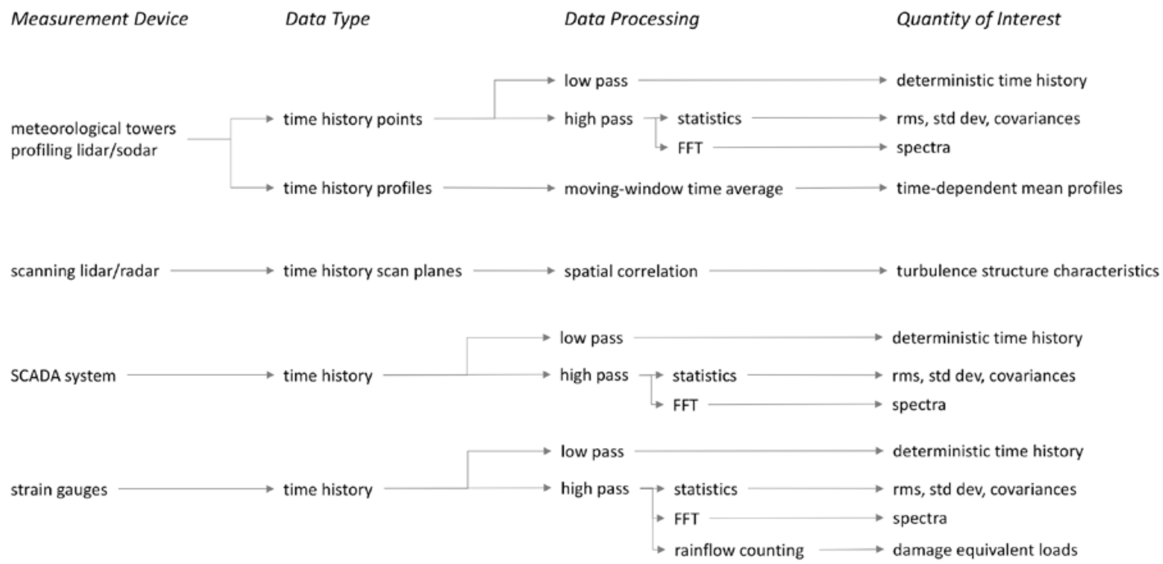

Figure 3.3. A flow chart illustrating the process of reducing raw wind-plant-centric data collected in the field or in experiments to useful quantities of interest.

We have begun simulating the Biglow Canyon wind farm because it is adjacent to the WFIP 2 Physics Site, for which we have a multitude of direct flow measurements, and we have obtained the wind-plant SCADA data. Assessment of the SCADA data has actively been performed in FY18, in conjunction with the A2e Wake Dynamics task, and will continue in FY19. We also will apply and refine our wind-plant-centric validation techniques to the SWiFT site, and possibly the National Wind Technology Center site.

3.4 Parametric Uncertainty Quantification

Uncertainty quantification work during FY18 has focused on two main tasks that will position us for additional progress during FY19.

The first task involves a collaboration with a group of applied mathematicians at PNNL to quantify uncertainty across multiple spatial and temporal scales in the presence of sparse data. An approach such as this is desirable due to the computational expense of microscale simulations. We conducted simulations using multiple nested LES domains in a single region, thereby obtaining information about the relationships between processes at multiple scales in that region. We then used co-kriging methods to understand how well the derived covariance structures in that region translate to other nearby regions. The results of this study indicate that spatial covariance information can only be extrapolated to areas near the fine-scale domain, due to the small length scale of the processes being modeled. Our next effort will be to explore uncertainty quantification using fine-scale simulations throughout the entire study area, but only turning on the finest scales periodically, thereby saving computational time.

The second task has involved getting Nalu installed on PNNL computing systems. This is in preparation for two main tasks. The first is to conduct parametric sensitivity studies in Nalu to understand how parametric uncertainty in Nalu compares to uncertainties in boundary-layer inflow. The second is to conduct actuator line simulations to explore the role of spacing and wakes on generated power in a simulated wind plant.

4.0 Mesoscale Modeling for MMC

In order to obtain a good solution for a mesoscale-to-microscale coupled simulation, one must first be able to provide a good mesoscale simulation. At times, the mesoscale model captures most of the physics, and the microscale model is able to fill in the fine-scale structures. But during times of nonstationarity, it is critical to first model that nonstationarity at the mesoscale, forced by the global scales. It is common for mesoscale models to be able to model structures like diurnal variations, frontal passage, thunderstorm outflows, and other transient features, but not quite get the timing correct. If one expects the microscale model to “follow” the mesoscale simulation, then those phase errors will be passed on to the microscale simulation.

This section studies the phase errors typical in modeling frontal passages at the mesoscale. Section 4.1 assesses whether using a different set of boundary and initial conditions can improve upon a simulation with a phase error. Section 4.2 looks at the progression of a front through a series of sites to assess the coherence of a phase error. Section 4.3 looks at applying a fully three-dimensional boundary-layer scheme to a frontal passage case.

4.1 Modeling Nov. 21 in WRF – A Complex Terrain Frontal Passage Case

The mesoscale HRRR simulations for the November 21, 2016 case show a phase shift compared to the observations, which is a disadvantage when using the simulations as input for microscale simulations. Therefore, the group analyzed whether this phase shift could be alleviated by using different boundary conditions. The HRRR was run with GFS boundary conditions, so we compared that to simulations using ERA-Interim boundary conditions. Note that the simulations using the ERA-Interim boundary conditions use the community WRF 3.7.1.

Shown below are time-height plots from lidar observations at the WFIP 2 Physics Site (Figure 4.1), output from the 3-km simulations of the HRRR runs using GFS boundary conditions (Figure 4.2), and from the WRF V3.7.1 simulations using ERA-Interim boundary conditions (Figure 4.3).

The time series output (Figure 4.4) shows that using different boundary conditions did not change the simulations considerably. Simulated wind speeds are too high before the ramp occurs. During the ramp the 80 m winds are too low in the ERA-WRF run, but the down ramp is well captured.

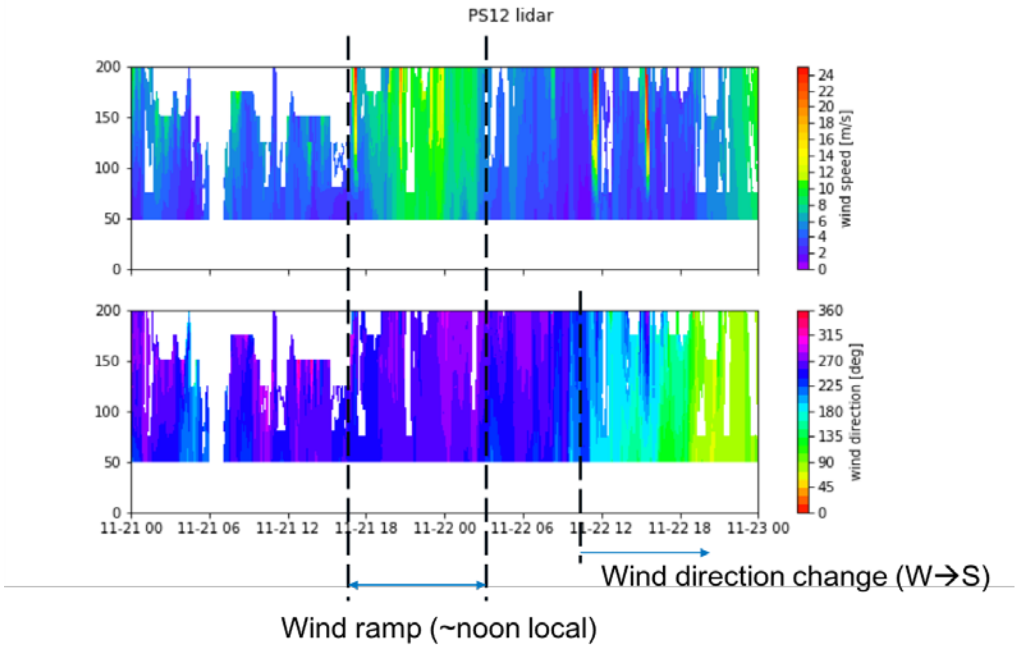

Figure 4.1. (Top) Wind speed and (bottom) wind direction as a function of time and height from lidar observations at the WFIP 2 physics site.

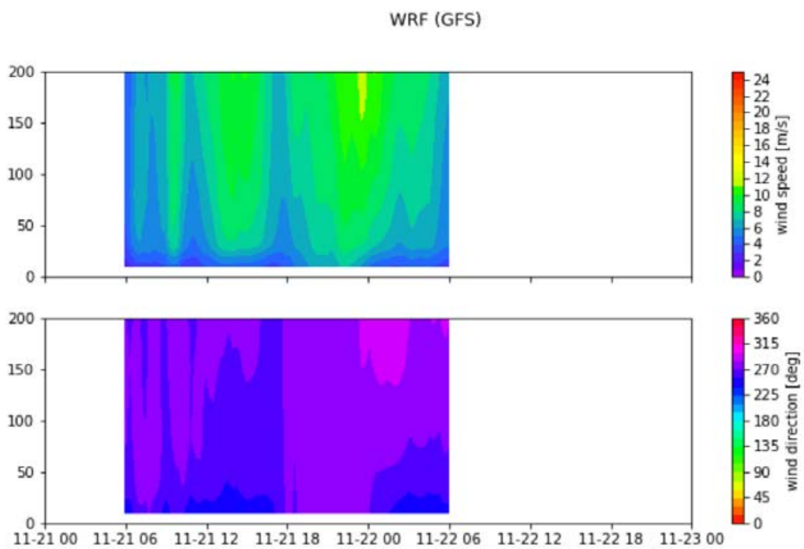

Figure 4.2. (Top) Wind speed and (bottom) wind direction as a function of time and height from HRRR simulations using GFS boundary conditions.

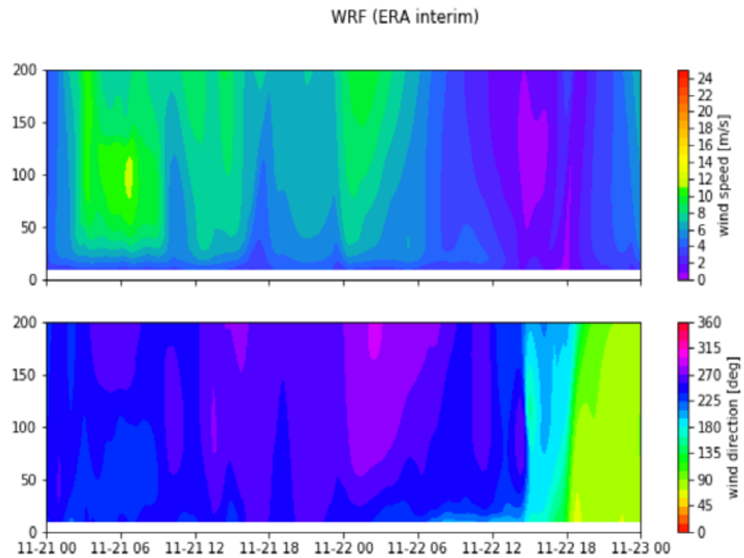

Figure 4.3. (Top) Wind speed and (bottom) wind direction as a function of time and height from WRF simulations using ERA-Interim boundary conditions.

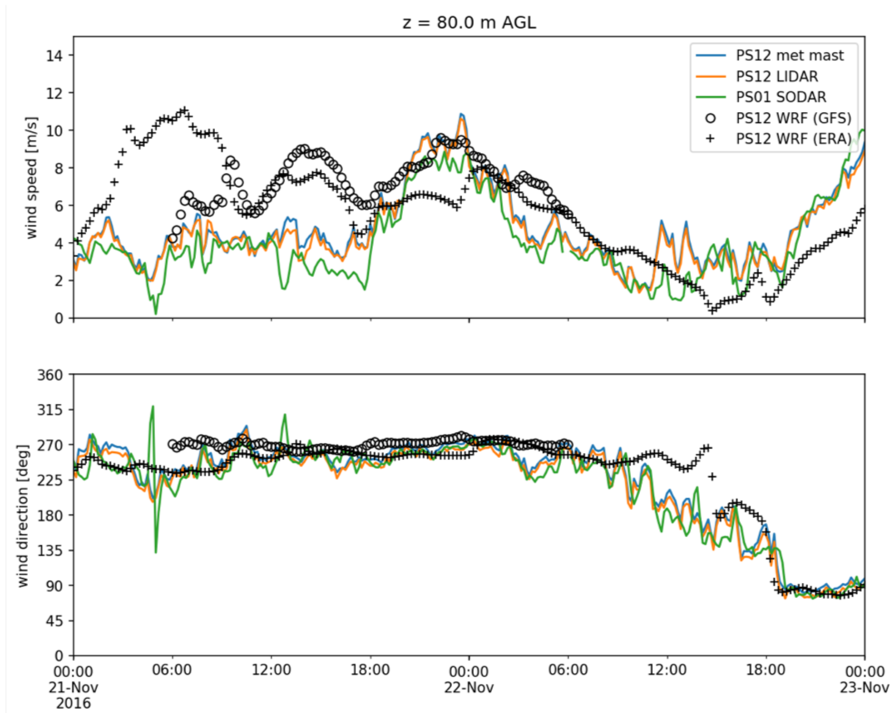

Figure 4.4. (Top) Wind speed and (bottom) wind direction time series sodar (green), lidar (orange), and met mast data (blue), HRRR simulations (circle), and WRF simulations (cross) at the Physics site. Note that sodar data are from a site 2.8 km upwind.

4.2 Formal Assessment of Mesoscale Forecast of Frontal Passage

The November 15, 2016 case was characterized by a frontal passage, occurring between 13:00 – 19:00 UTC. Predictions from the mesoscale model referenced in section 3.1 are evaluated against observations from several locations at the WFIP 2 site (see section 3.1 for a complete list). Time series and summary statistics are given in the following subsections for potential temperature, wind direction, and wind speed.

4.2.1 Potential Temperature

Time series plots of temperature from each of the MET and BPA stations referenced in Section 3.1 are shown in Figure 4.5, depicting the model data points for temperature (at heights corresponding to each sensor) in red. Summary statistics for each observation-model output pair are given to the right of each plot. The plots and statistics are listed by location from west to east.

On average, the potential temperature predictions are within a couple degrees of the observed values. The model did not consistently predict the trend in potential temperature across space, although it did notably well in the northeastern part of the site, as evidenced by high correlation coefficients at the BPA Horse Heaven (HOR) and BPA Chinook (CNK) locations.

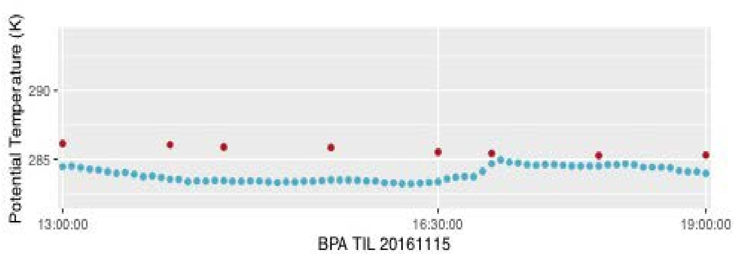

statistic	value
ME	-1.74
RMSE	1.87
MAE	1.74
CC	-0.32

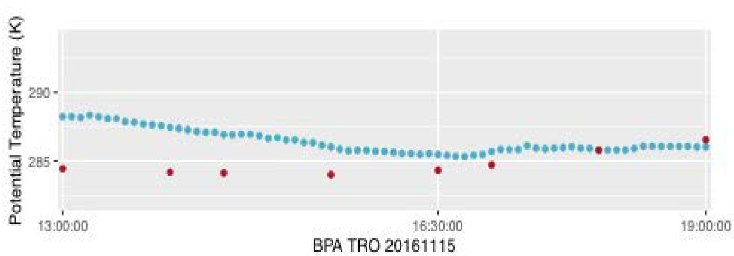

statistic	value
ME	1.68
RMSE	2.22
MAE	1.81
CC	-0.33

Figure 4.5. Time series plots of potential temperature, with observational data in blue and model predictions in red.

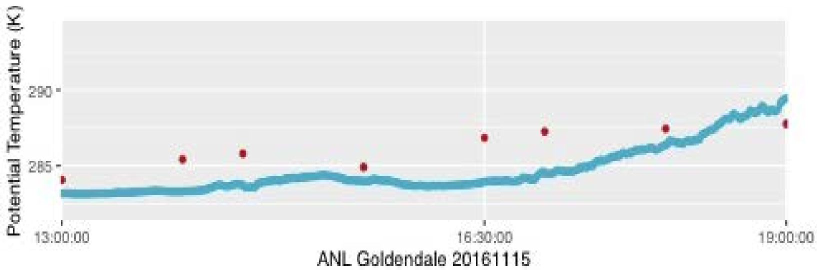

statistic	value
ME	-1.39
RMSE	1.96
MAE	1.81
CC	0.73

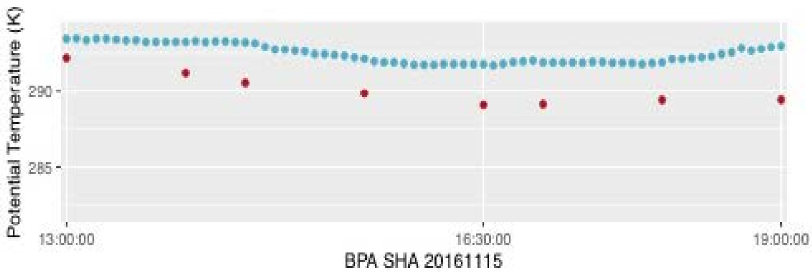

statistic	value
ME	2.46
RMSE	2.53
MAE	2.46
CC	0.84

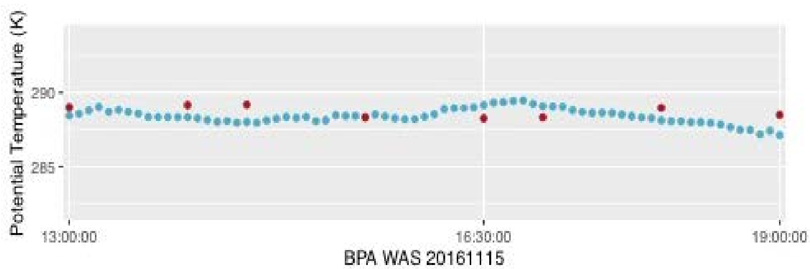

statistic	value
ME	-0.38
RMSE	0.89
MAE	0.81
CC	-0.32

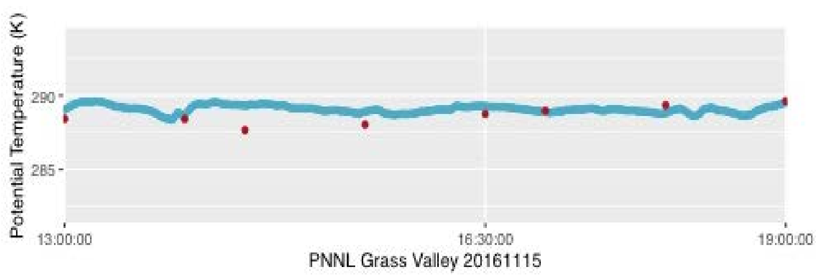

statistic	value
ME	0.40
RMSE	0.76
MAE	0.59
CC	0.12

Figure 4.5. (contd)

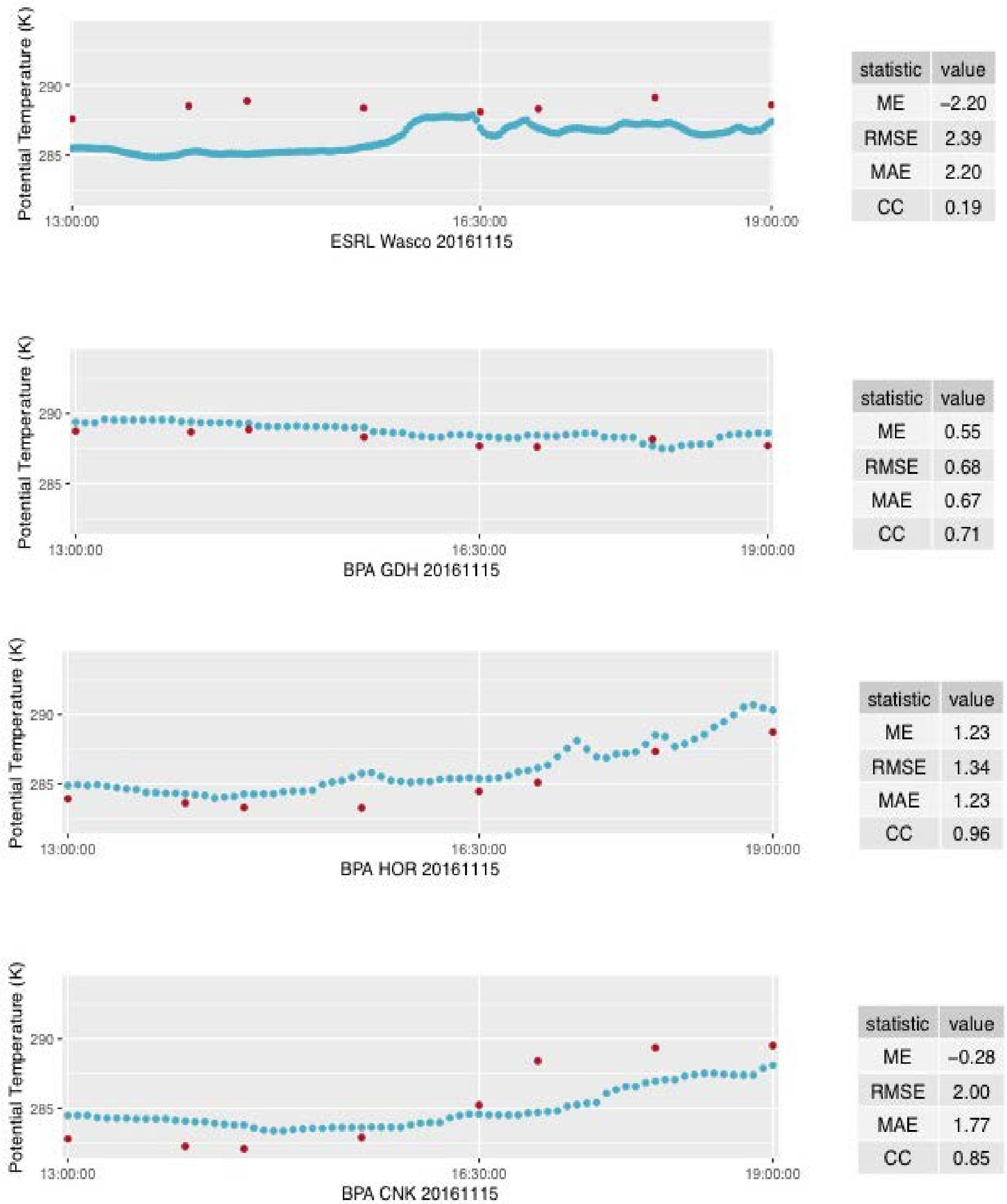

Figure 4.5. (contd)

4.2.2 Wind Speed and Wind Direction

Time series plots of wind speed and wind direction from each of the six sodar stations (referenced in Section 3.1 and shown in Figure 4.6) and the corresponding model output time series for the sensor location are provided in Figure 4.7 through Figure 4.12. Summary statistics for each observation-model output pair are given in Table 4.1 and Table 4.2.

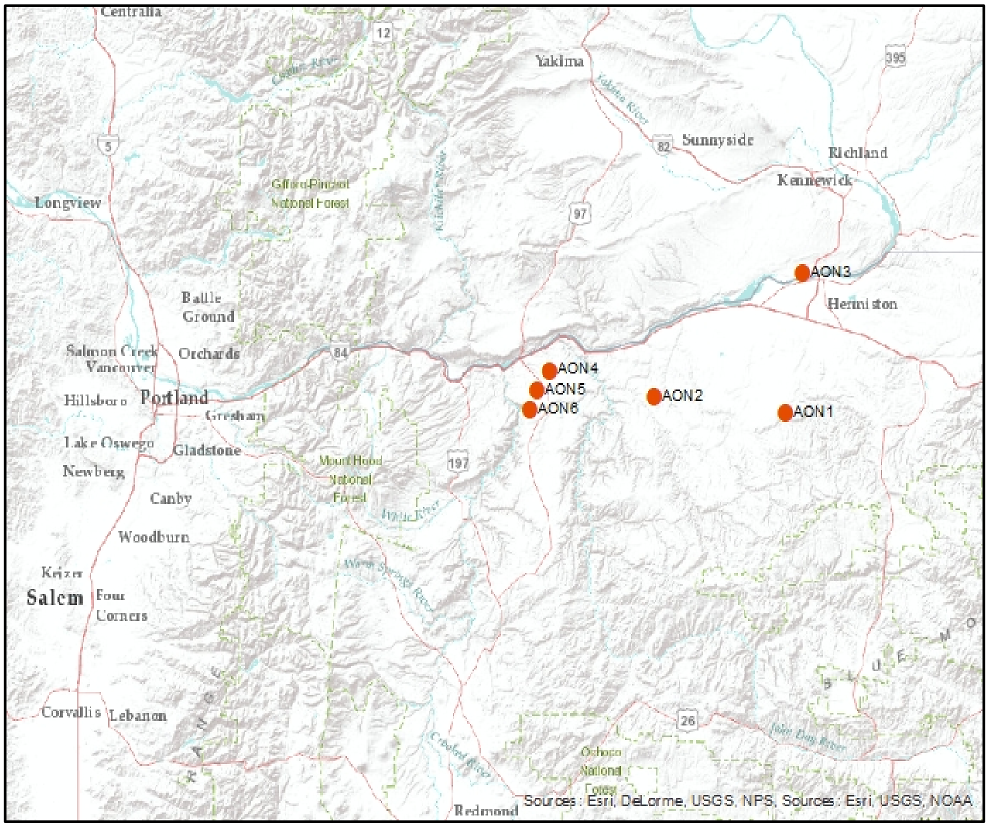

Figure 4.6. Map of sodar station locations.

Wind speed at the AON6 location varies in magnitude by height but follows the same trend throughout the hours from 13:00 – 19:00 UTC, with lower speeds generally at the lower sensor heights. At this location, the wind is southwesterly at 13:00 UTC and shifts to westerly around 18:00 UTC. The model did not capture the trend in wind speed values for the AON6 location, predicting a slight increase from 13:00 – 14:30 UTC, and a decrease from 18:00 – 19:00 UTC that is not seen in the observation data. However, the model followed the general trend in wind direction from the southwest to the west, though it was forecast an hour early.

Wind speeds at the AON5 location increased steadily from less than 5 m/s to about 10 m/s throughout the time window, with a peak around 17:45 UTC. Wind direction at the AON5 location varies quite a bit at the beginning of the time window (during frontal passage), but steadies to westerly around 14:00 UTC. The model did capture the increase in wind speed at this location, although the values were about 5 ms^{-1} higher than the observation values throughout the time window. It did not predict the initial variance in direction by height at the AON5 location but did eventually capture the steady westerly wind after frontal passage.

Similarly, winds increased steadily at the AON4 location, with a peak around 17:30 UTC. Wind direction at AON4 also varied until around 14:00 UTC, and on average steadied, coming from the west, although there were still large directional shifts at the lower levels. The model did not predict wind speed or direction well at this location. The increase in wind speed was predicted a few hours earlier than observed, the initial variance in direction was not captured, nor was the trend in direction, indicating a potential phase error in capturing the frontal passage.

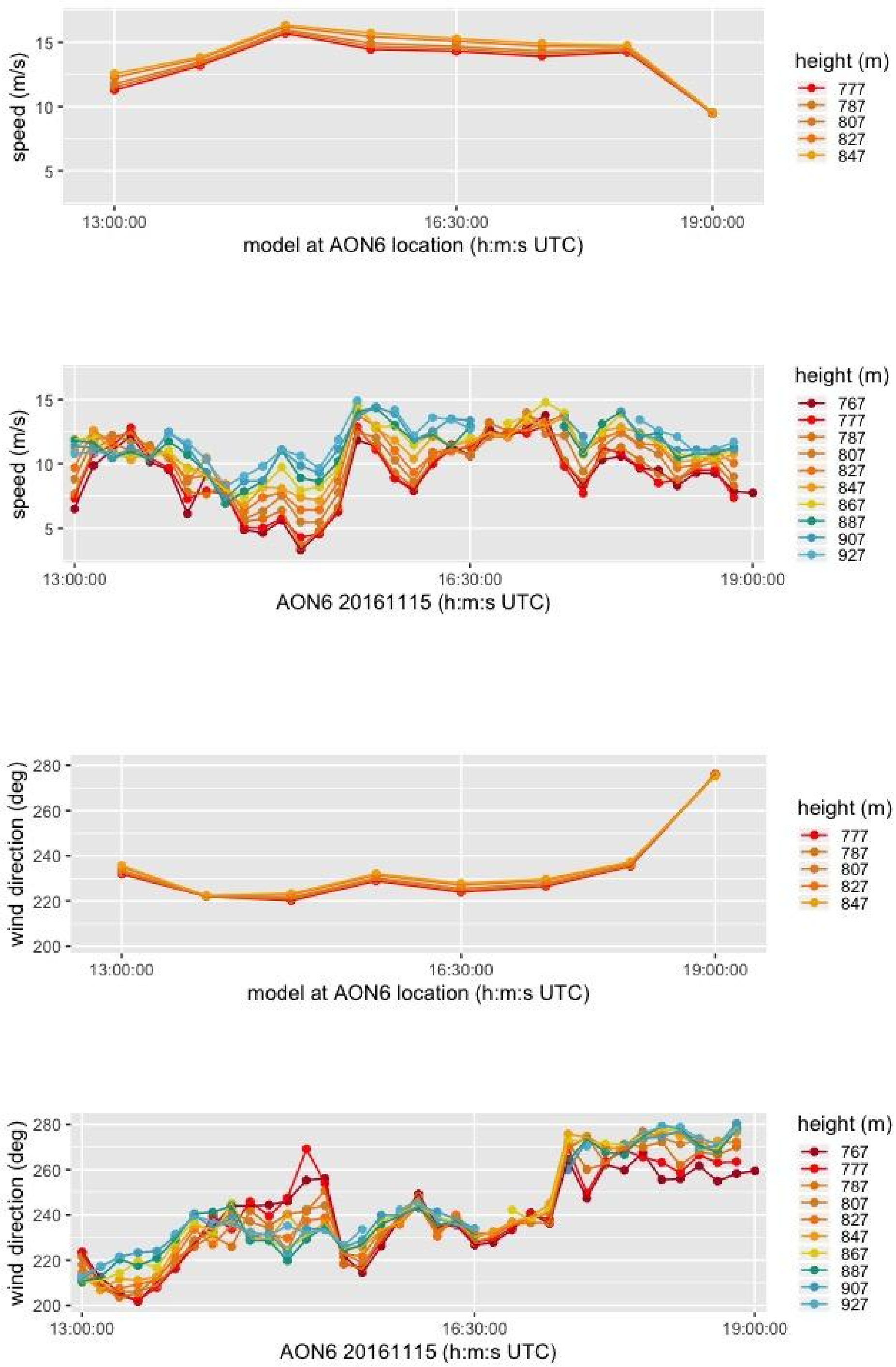

Figure 4.7. Time series plots of wind speed predictions, wind speed observations, wind direction predictions, and wind direction observations at sodar station AON6.

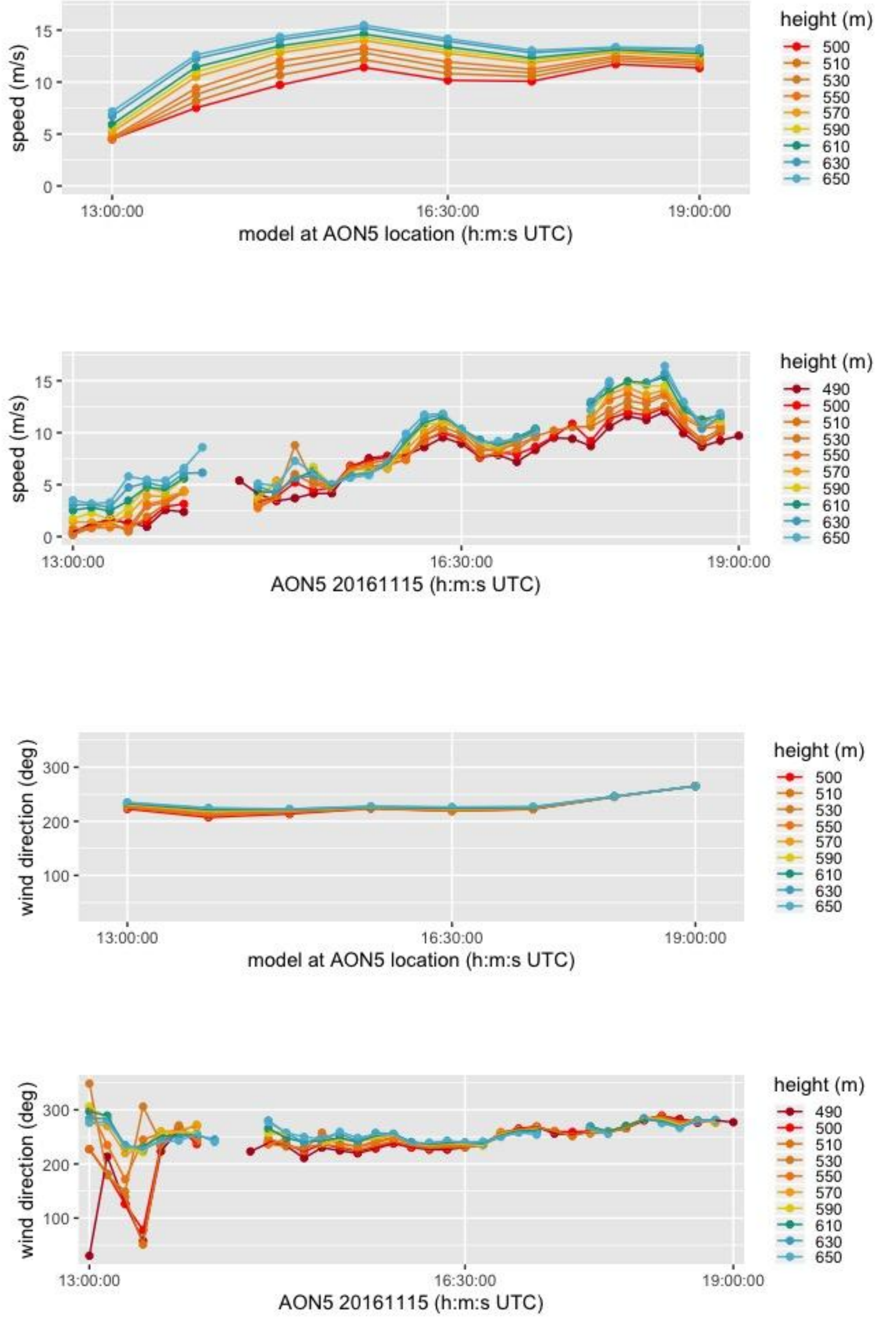

Figure 4.8. Time series plots of wind speed predictions, wind speed observations, wind direction predictions, and wind direction observations at sodar station AON5.

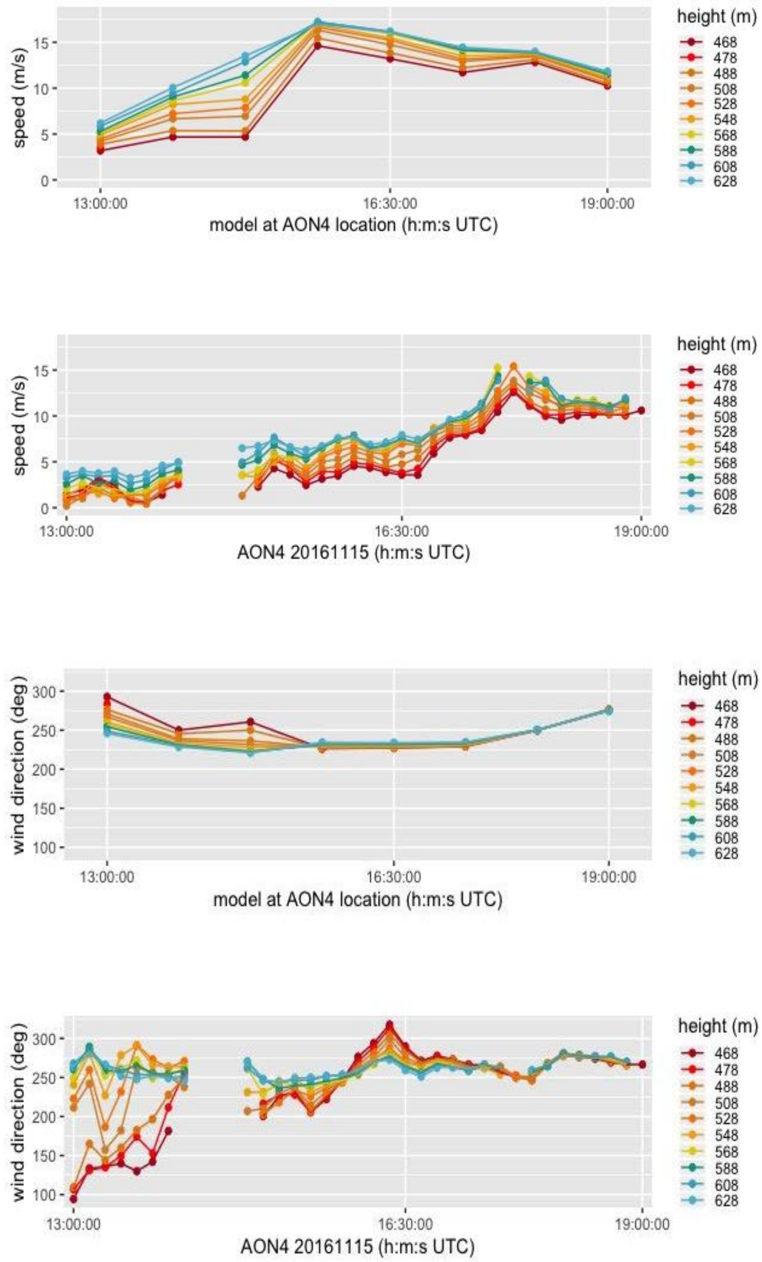

Figure 4.9. Time series plots of wind speed predictions, wind speed observations, wind direction predictions, and wind direction observations at sodar station AON4.

Wind speed at the AON2 location also increased throughout the time window, rising from less than 5 ms^{-1} to about 13 ms^{-1}, with the lowest speeds at the lowest sensor heights. Observations show a steady westerly wind at this location throughout the time window. Overall the model did well in predicting both wind speed and direction at this location. It captured the increase in wind speed, though again the predicted values were about 5 ms^{-1} higher and predicted a steady westerly wind.

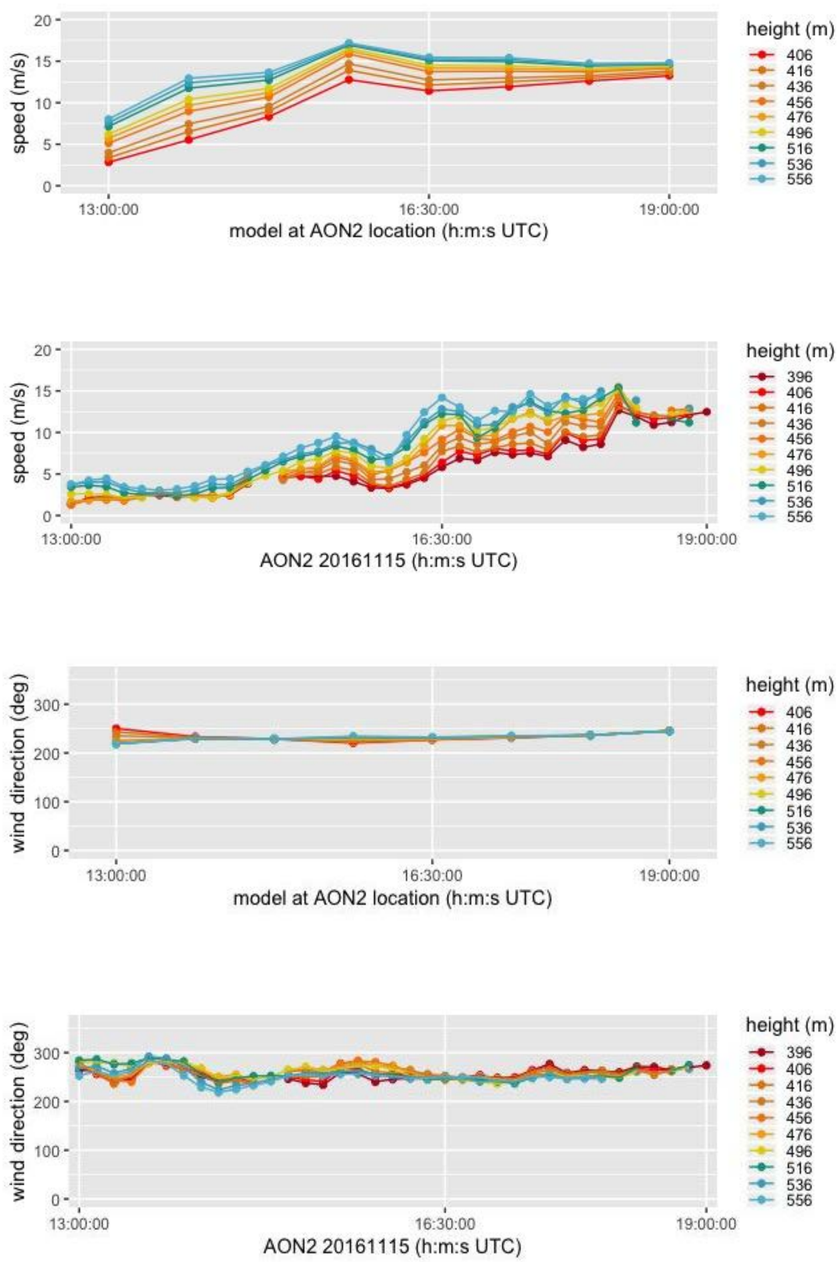

Figure 4.10. Time series plots of wind speed predictions, wind speed observations, wind direction predictions, and wind direction observations at sodar station AON2.

Wind speeds at the AON1 location decreased slightly, from about 15 ms^{-1} to 10 ms^{-1}, again with the lowest speeds at the lowest sensor heights. Observations at AON1 show a fairly steady wind, although it began from the south and shifts to southwesterly around 16:00 UTC, as the front passes. The model performed well at AON station 1 in particular. At this location, the model values decreased slightly as in the observed data, though after 16:30 UTC the model forecasts a slight dip and increase that is not present in the observations. The predicted values for wind speed followed a similar trend as the observations, with little variation between heights and a slight shift in direction around 16:00 UTC.

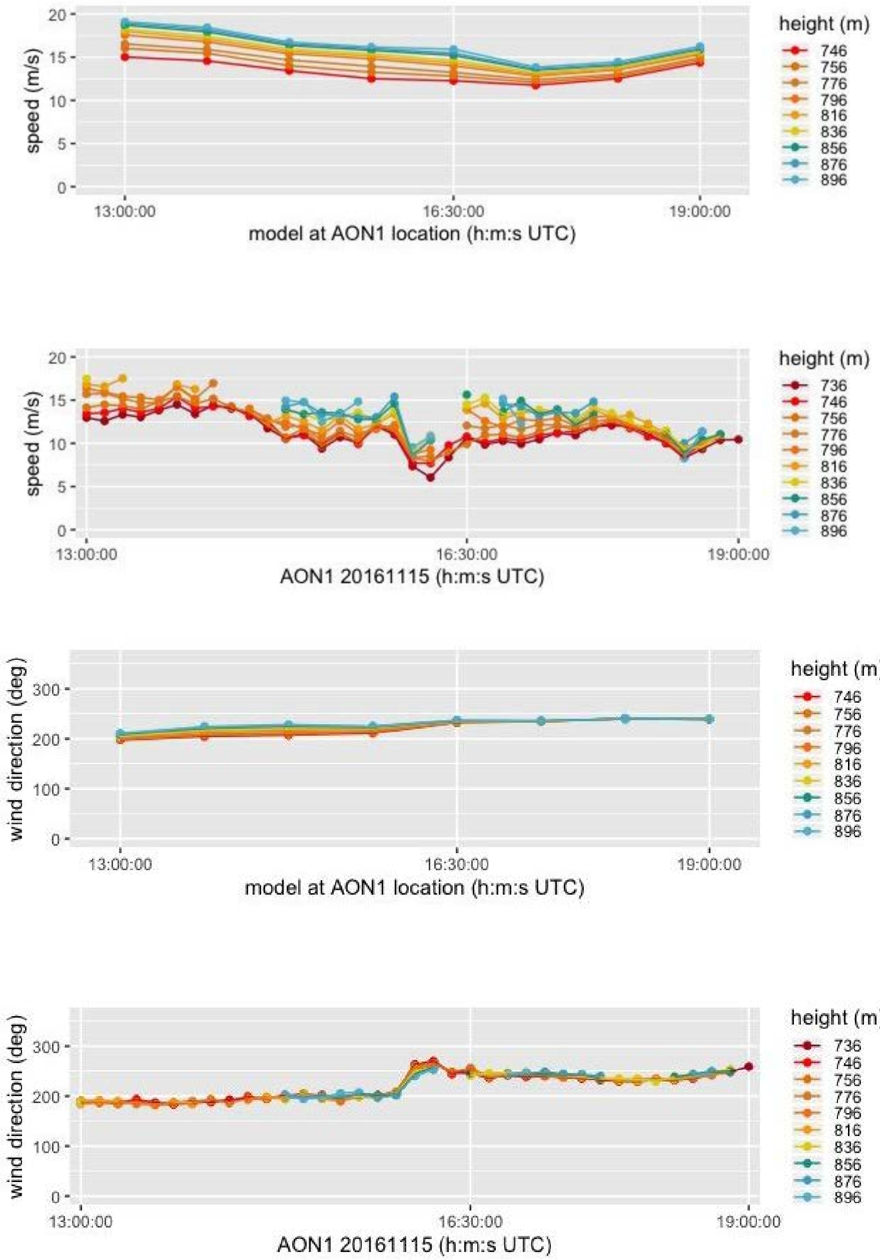

Figure 4.11. Time series plots of wind speed predictions, wind speed observations, wind direction predictions, and wind direction observations at sodar station AON1.

At the AON3 location observations show a small increase in wind speed followed by a dip around 17:00 UTC and an increase during frontal passage. The wind direction at the AON3 location shows the most variance,[1] with most wind shifts at the lower sensor heights. The model captured the steady, low wind speeds at the beginning of the time window at the AON3 station, but it did not pick up the small dip and increase between 16:30 and 19:00 UTC. Although the model did not show the same overall trend, it did forecast some variance with height at the AON3 location.

[1] This is exaggerated due to the method of plotting, with 0 and 360 degrees both being from the north but associated with different values at either end of the y-axis.

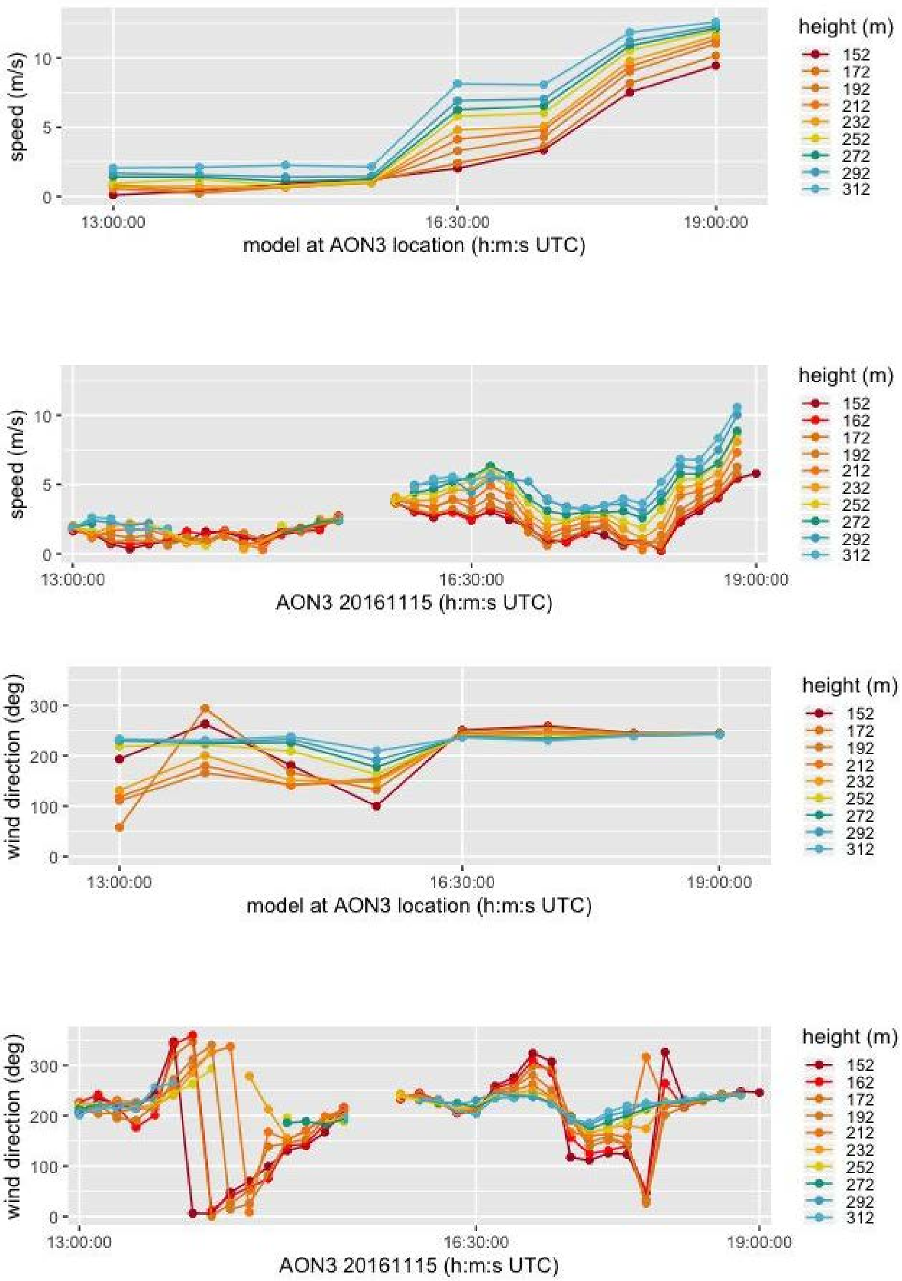

Figure 4.12. Time series plots of wind speed predictions, wind speed observations, wind direction predictions, and wind direction observations at sodar station AON3.

Table 4.1. Summary statistics for wind speed forecast versus observation values at AON stations.

	statistic	40 m	50 m	60 m	80 m	100 m	120 m	140 m	160 m	180 m	200 m
AON1	ME	NA	-1.5	-1.93	-1.56	-1.74	-1.51	-1.39	-1.33	-1.91	-2.44
	RMSE	NA	1.79	2.28	2.02	2.27	2.32	2.19	2.67	2.63	2.83
	MAE	NA	1.5	1.93	1.56	1.74	1.66	1.55	2.25	2.33	2.44
	CC	NA	0.74	0.73	0.71	0.62	0.57	0.59	-0.65	-0.96	0.33
AON2	ME	NA	-3.84	-4.17	-4.33	-5.01	-4.99	-4.87	-5.52	-5.39	-5.04
	RMSE	NA	4.37	4.69	4.89	5.6	5.69	5.76	6.45	6.47	6.17
	MAE	NA	3.84	4.17	4.33	5.01	4.99	4.87	5.52	5.49	5.04
	CC	NA	0.83	0.83	0.83	0.79	0.77	0.72	0.65	0.62	0.65
AON3	ME	-1.27	NA	-1.48	-1.73	-2.1	-2.01	-2.49	-2.95	-3.08	-3.65
	RMSE	2.98	NA	3.27	3.62	3.94	3.79	4.04	4.24	4.15	4.64
	MAE	2.07	NA	2.26	2.49	2.5	2.45	2.79	3.14	3.18	3.65
	CC	0.64	NA	0.62	0.61	0.57	0.64	0.65	0.6	0.67	0.73
AON4	ME	-4.77	-3.84	-4.83	-5.12	-4.98	-4.91	-4.8	-4.84	-4.78	-6.35
	RMSE	6.32	4.37	6.29	6.58	6.39	6.37	6.26	6.26	6.2	6.95
	MAE	4.87	3.84	4.96	5.28	5.06	5.04	4.87	4.84	4.78	6.35
	CC	0.44	NA	0.49	0.5	0.51	0.48	0.48	0.46	0.41	0.75
AON5	ME	NA	-2.49	-2.64	-2.75	-2.78	-3.18	-3.18	-3.34	-4.5	-4.63
	RMSE	NA	3.08	3.23	3.53	3.72	4.25	4.37	4.53	5.19	5.41
	MAE	NA	2.55	2.78	2.97	3.14	3.61	3.72	3.86	4.5	4.63
	CC	NA	0.92	0.89	0.85	0.81	0.72	0.67	0.61	0.6	0.52
AON6	ME	NA	-4.16	-4.12	-3.59	-3.36	-2.97	NA	NA	NA	NA
	RMSE	NA	5.03	4.91	4.6	4.41	4.08	NA	NA	NA	NA
	MAE	NA	4.16	4.12	3.59	3.36	2.99	NA	NA	NA	NA
	CC	NA	0.26	0.26	0.15	0.17	0.17	NA	NA	NA	NA

Table 4.2. Summary statistics for wind direction forecast versus observation values at AON stations.

	statistic	40 m	50 m	60 m	80 m	100 m	120 m	140 m	160 m	180 m	200 m
AON1	ME	NA	-0.3	-2.48	-3	-5.96	-3.36	-0.55	6.31	4.3	7.81
	RMSE	NA	14.29	15.26	15.55	18.47	17.96	16.88	16.92	19.28	20.79
	MAE	NA	12.6	14.42	14.88	17.22	16.76	14.9	15.63	18.08	19.26
	CC	NA	0.93	0.93	0.94	0.91	0.9	0.9	0.99	0.99	0.99
AON2	ME	NA	26.71	27.79	29.15	29.9	30.25	30.58	28.99	22.65	15.97
	RMSE	NA	28.5	29.81	31.79	33.32	33.34	35.64	35.2	27.78	19.57
	MAE	NA	26.71	27.79	29.15	29.9	30.25	30.58	28.99	22.65	17.1
	CC	NA	0.57	0.47	0.31	0.04	-0.03	-0.15	-0.69	-0.41	-0.01
AON3	ME	-75.82	NA	-15.76	-13.24	19.79	30.1	-0.07	-11.29	-7.29	-18.53
	RMSE	132.95	NA	114.56	116.39	81.39	71.16	22.54	16.99	13.67	24.38
	MAE	97.97	NA	90.64	93.23	66.26	56.37	16.68	14.28	11.49	21.81
	CC	0.13	NA	0.27	0.09	0.54	-0.28	-0.27	0.37	0.58	0.94
AON4	ME	-24.73	-3.84	-13.89	4.71	8.7	13.65	14.32	15.49	17.87	21.64
	RMSE	85.09	4.37	69.68	33.95	29.46	25.5	21.82	20.44	20.43	22.18
	MAE	60.21	3.84	47.18	28.24	25.61	22.12	18.63	17.55	18.43	21.64
	CC	-0.6	NA	-0.46	-0.16	-0.15	0.05	0.3	0.53	0.77	0.68
AON5	ME	NA	17.47	16.96	35.77	32.22	29.12	30.95	28.44	25.15	25.28
	RMSE	NA	22.55	21.61	51.18	39.83	32.96	36.97	32.97	28.62	27.11
	MAE	NA	17.47	16.96	35.77	32.22	29.12	30.95	28.44	25.15	25.28
	CC	NA	0.73	0.74	0.26	0.33	0.5	0.44	0.54	0.62	0.77
AON6	ME	NA	5.23	5.3	6.65	5.36	5.08	NA	NA	NA	NA
	RMSE	NA	16.65	15.98	17.55	16.52	16.52	NA	NA	NA	NA
	MAE	NA	14.12	12.58	13.39	12.94	12.43	NA	NA	NA	NA
	CC	NA	0.57	0.67	0.69	0.69	0.68	NA	NA	NA	NA

The analysis of wind speed and direction observed on November 15, 2016 from the six sodars deployed in the WFIP 2 field study area east of the Cascades reveals a passage of a weak cold front. Before the frontal passage observed winds are weak, generally less than 5 ms^{-1}, except at the far southeastern location (AON1) where wind speeds are 15 ms^{-1}. The significant difference in observed wind speeds could be attributed to the contrast between mountain wake that affects sodars AON2, AON4, AON5, and AON6 and a gap flow through the Columbia River Gorge that affects AON1. A signature of a weak front can be seen between 16:00 and 17:00 UTC. Corresponding weather maps from the National Oceanic and Atmospheric Administration's Weather Prediction Center archive (https://www.wpc.ncep.noaa.gov/noaa/noaa_archive.php?reset=yes) indicate the passage of a cold northwesterly front that brought snow to the area. The sodar observations are consistent with a northwesterly front as it affected the northern sodar AON6 first (Figure 4.7) at about 16:00 UTC, followed by AON5 (Figure 4.8) at about 16:30 UTC, and finally AON4 (Figure 4.9) at 17:00 UTC. At these three sodar locations the wind speed increases to 10 – 15 ms^{-1} while the wind direction changed to westerly following a frontal passage. Changes in wind direction and wind speed indicate that after the frontal passage the gap flow spread further south.

4.3 Development of a PBL Parameterization with Three-Dimensional Turbulent Mixing

The MMC team is also continuing the work of the WFIP 2 team to develop and test fully three-dimensional boundary-layer schemes. The planetary boundary-layer (PBL) parameterizations implemented in numerical weather prediction models are based on the assumption of horizontal homogeneity. Under this assumption, the horizontal turbulent mixing is neglected. Hence, current PBL parameterizations are one-dimensional with turbulent mixing only accounted for in the vertical direction. However, the assumption of horizontal homogeneity does not hold at high horizontal grid spacings. To overcome this limitation, we are developing a three-dimensional PBL parameterization that accounts for both horizontal and vertical turbulent mixing.

We have tested the 3D-PBL parameterization in idealized cases, and now we are moving to test it in real cases. Unfortunately, the simulations that we have performed so far turn unstable. Further development to the 3D-PBL is necessary to fix the problem(s).

We have conducted a number of tests to isolate the origin of the instabilities. With this aim, we configured WRF with the same setup for the November 15, 2016 case over the WFIP 2 domain. This experiment has two domains, with domain 01 using roughly 1-km grid spacing and a standard one-dimensional-PBL parameterization, and domain 02 using about 100-m grid spacing with a large-eddy simulation (LES) closure to represent turbulent mixing. Initially we only changed the turbulence representation from LES to the three-dimensional-PBL parameterization in domain 02. Our progress and primary findings can be summarized as follows:

- The simulation became unstable after 1 s.
- To identify the problem we applied what is known as the “PBL approximation,” wherein the horizontal gradients of resolved quantities as well as vertical gradients of the vertical velocity are neglected in the calculation of the turbulent fluxes. The simulation became unstable after 11 s.
- We tried reducing the number of vertical levels from 145 to 45. However, the simulation still became unstable after about 15 s. The instability is generated over the steep slopes of Mt. Hood.
- We decided to simplify the experiment a bit further and we turned off the second domain and turned on the 3D-PBL parameterization in the first domain (D01). However, the simulation became unstable at roughly 15 s. The instability originated in the first model level over the slopes of the mountain.
- The model ran for a few hours before becoming unstable when we reduced the time step from 1 s to 0.01 s.
- The slopes of the mountain where we have the instability have snow, and we did another experiment wherein we removed the snow. The simulation also became unstable.
- To further explore the impact of the mountain slope, we artificially reduced the elevation by 30%. In this case the simulation ran for almost a minute. This points to topographic issues as the origin of the instability.

Our working hypothesis at this moment is that steep slopes can trigger instabilities in the 3D-PBL parameterization. We are developing the code to reduce the turbulent mixing strength over grid cells with steep slopes.

5.0 Documenting the Impact of the *Terra Incognita*

5.1 Analysis of Coupled Simulations in Terms of *Terra Incognita* Issues

The impact of the *terra incognita* on mesoscale and microscale simulations was evaluated using a series of coupled online simulations using multiple nested domains to downsize the horizontal grid spacing from mesoscale to microscale. In some of the tested model configurations, the horizontal grid spacing of one or more domains often falls into the *terra incognita* (nominally having a grid spacing from about 100 m – 1 km). In these situations, existing boundary-layer parameterizations can fail, producing anomalous numerical rolls.

In the study presented by Rai et al. (2018), the impact of boundary forcing from a domain within the *terra incognita* on a nested microscale simulation was evaluated using a number of simulations by varying the horizontal grid spacing applied on parent domains (Table 5.1, domain D02). However, the size of the outermost domain of all simulations was similar, and the horizontal grid spacing is comparable to or larger than the boundary-layer depth (i.e., ~ 2 km). Figure 5.1 shows the contours of the instantaneous w-component of velocity for domain D02 using various horizontal grid spacings and turbulence parameterizations. The horizontal grid spacing varied between 1.44 km to 0.32 km, all within the *terra incognita*, and two types of turbulence parameterizations—those designed for mesoscale simulations (MYNN or YSU) or those designed for LES (Lilly model). Figure 5.1a compares results using MYNN and YSU schemes. It shows that simulations with smaller grid spacing resolved more tke and finer structures. However, there are different amounts of tke resolved for MYNN and YSU schemes for the same horizontal grid spacing associated with the different approaches (i.e., local and non-local) and order of closure (i.e., first and second). Compared to the Lilly model results (Figure 5.1b), the MYNN/YSU model produced a completely different flow structure, particularly for the smaller grid spacing. The structures are oriented along the mean wind direction when the Lilly model is employed, whereas they are irregular cell-like structures in the simulations completed using the MYNN and YSU schemes. Note that all horizontal grid spacings studied are within the *terra incognita*. Both the MYNN and YSU schemes produced similar shaped spectra, and as expected, the simulations with finer grid spacing resolves more tke (Figure 5.2a and Figure 5.2b). However, the amount of energy contained at different frequencies from these two types of turbulence models differs. The Lilly model produces more spectral energy compared to MYNN or YSU schemes.

Table 5.1. Domain configuration for different simulations.

<table>
<tr><th rowspan="2">Run</th><th colspan="3">D01</th><th colspan="2">D02</th><th colspan="3">D03</th></tr>
<tr><th>Δxy</th><th>L_x</th><th>L_y</th><th>Δxy</th><th>L_x, L_y</th><th>Δxy</th><th>L_x</th><th>L_y</th></tr>
<tr><td>**Ti1**</td><td>2.88</td><td rowspan="6">900</td><td rowspan="6">L_x</td><td>1.44</td><td rowspan="6">155</td><td rowspan="3">0.24</td><td rowspan="3">50</td><td rowspan="3">L_x</td></tr>
<tr><td>**Ti2**</td><td>3.84</td><td>0.96</td></tr>
<tr><td>**Ti3**</td><td>2.88</td><td>0.48</td></tr>
<tr><td>**Ti4**</td><td>2.56</td><td>0.32</td><td rowspan="3">0.04</td><td rowspan="3">10</td><td rowspan="3">18</td></tr>
<tr><td>**Ti5**</td><td>2.52</td><td>0.28</td></tr>
<tr><td>**Ti6**</td><td>2.40</td><td>0.24</td></tr>
</table>

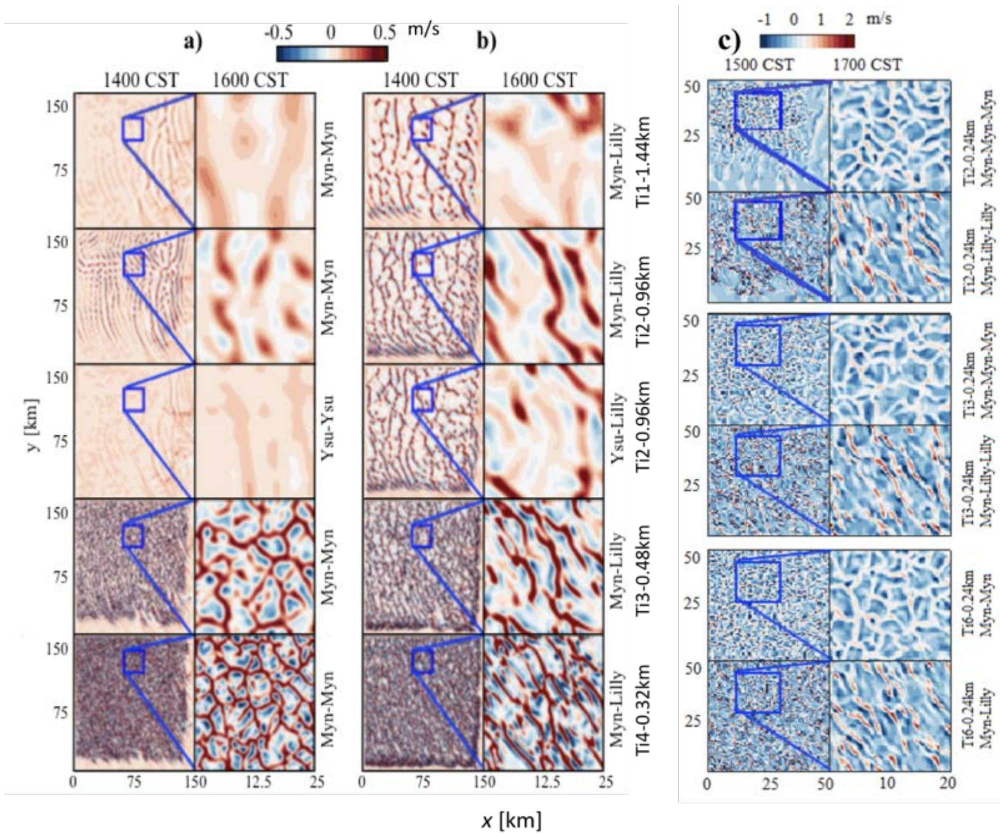

Figure 5.1. Instantaneous w-component velocity for simulations with varying horizontal grid spacing (top to bottom row) and using different turbulence models: a) MYNN/YSU scheme and b) Lilly model. Contour plot of the w-component velocity for grid resolution of 200 m with MYNN/YSU and Lilly model c) forced by a domain with different combinations of turbulence model and grid spacing as denoted.

The instantaneous vertical velocity from a microscale domain forced by the intermediate domains listed in Table 5.1, as well as by the outermost mesoscale domain, are shown in Figure 5.1c. As mentioned previously, the intermediate domains use different horizontal grid spacing and turbulence models. The results indicate that the flow structures on the microscale domain are similar for all simulations. The only differences in the structures are associated with the type of turbulence model used at the microscale. Furthermore, the spectra for the u-component velocity (Figure 5.2c and Figure 5.2d) also show similar spectral energy for various frequencies. The only difference is the magnitude of the spectral energy for the two different types of turbulence model. This suggests that the energy of the microscale domain depends on the type of turbulence model used for that particular domain, but that those results are insensitive to the grid spacing and type of turbulence model used on the parent domain.

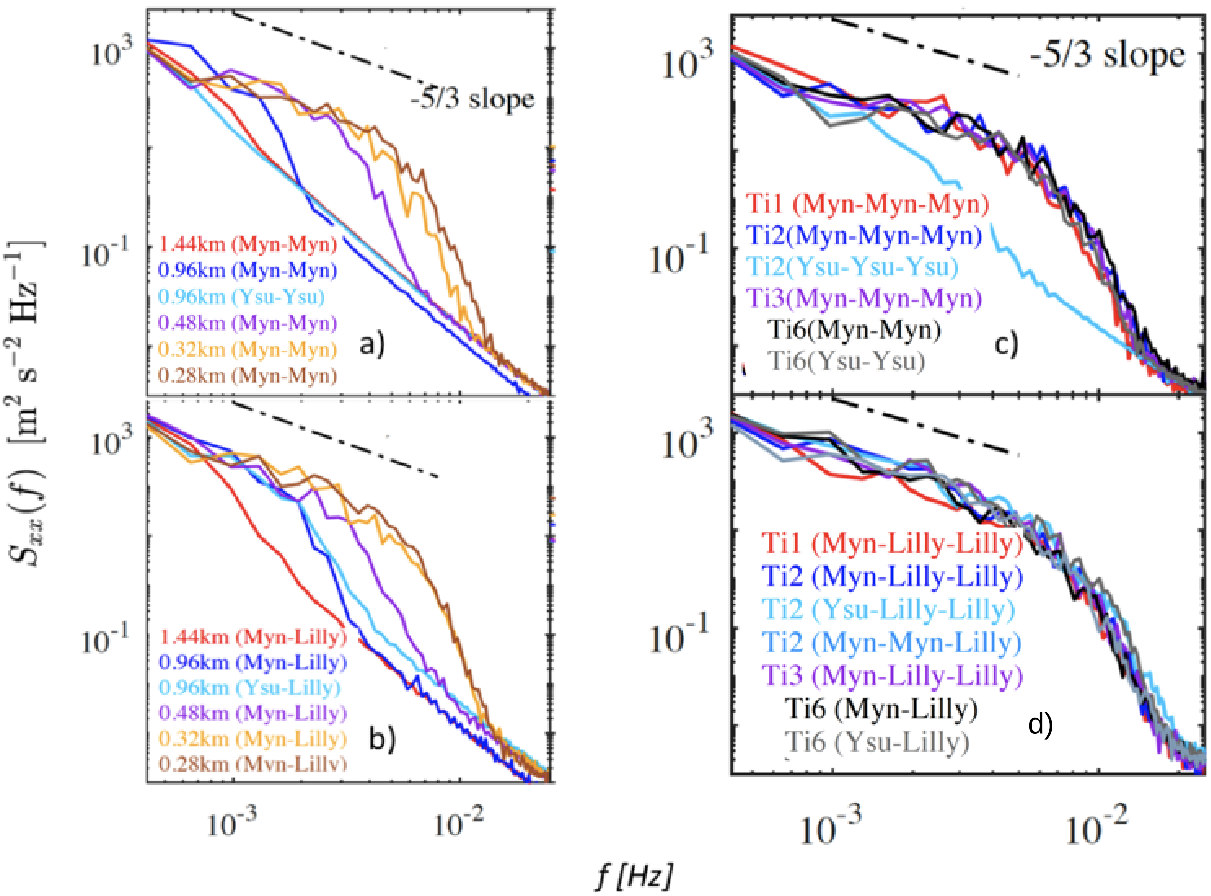

Figure 5.2. Spectra for u-component velocity for several grid resolutions at the mesoscale (1.44 km – 0.28 km) that use the a) MYNN/YSU scheme and b) Lilly model. c) Spectra for u-component velocity for a 240-m grid spacing simulation forced by a domain with varying grid resolution and turbulence model.

5.2 Guidance for Configuring Mesoscale Simulations for MMC

The results presented here, together with those of Rai et al. (2018) have led to suggesting specific guidance for coupled simulations with grids that span the *terra incognita*.

- While running either a single mesoscale domain or nested mesoscale simulation, the horizontal grid spacing should be greater than, or at least comparable to, the boundary-layer thickness. In addition, while a mesoscale domain grid spacing used to force the microscale domain could use a grid spacing smaller than the boundary-layer depth, the domains could also be configured to skip over the *terra incognita*.
- When not using perturbations (velocity, temperature) at the boundaries, the area of interest in the nested microscale domain must be kept far enough (~ z_i) from the inflow boundary to ensure that the turbulence has adequately spun up.

6.0 Generating Turbulence in the Microscale Simulations

Because mesoscale models do not resolve the fine-scale turbulence of the atmospheric boundary layer, turbulence-generation methods are required at the interface of a large-eddy simulation microscale domain situated within and forced by a mesoscale domain. For this type of coupling, mesoscale flows are modeled by large, coarsely resolved domains, the solution of which is then used as boundary conditions to smaller, highly resolved, microscale domains that are strategically placed over an area of interest. This enables modeling of a wide range of scales, while considering mesoscale heterogeneities, without incurring the enormous computational costs required by a single-domain simulation. However, such coarsely resolved parent domains are lacking the fine scales of turbulence expected from the higher resolution domains. These finer scales are developed over a certain distance in the LES, which can be very costly (Tabor and Baba-Ahmadi, 2010; Zajaczkowski, et al., 2011; Mirocha, et al., 2014; Muñoz-Esparza, et al., 2014). This fetch can take a distance of over 30 km downstream of the inflow boundary for a microscale simulation performed at grid-cell sizes of ~50 m (Muñoz-Esparza, et al., 2014; Mazzaro, et al., 2017). Turbulence-generation methods aid in reducing the turbulence-generation fetch, thus saving valuable computational resources, making this type of coupling more accessible.

6.1 Introduction to Random Perturbation Methods

Different turbulence-generation methods have been developed. Some of these methods use statistics of the desired turbulence to superimpose turbulent motions, or to strategically force the incoming flows (Keating, et al., 2004, Zajaczkowski, et al., 2011, Poletto, et al., 2013). Other methods recycle turbulent motions within a simulation by extracting them from the outflow and imposing them on the inflow boundaries (Araya, et al., 2011; Morgan, et al., 2011; Nakayama, et al., 2012).

Most recently, random perturbation methods have been increasingly used due to their simplicity and effectiveness. The main one of these methods is the random potential temperature (θ) perturbation method (Muñoz-Esparza, et al., 2015 and 2018). The θ perturbation method adds stochastic, small-scale variations to the θ fields over cells composed of 8x8 horizontal grid points in the horizontal direction. These variations trigger small-scale motions, and thus significantly accelerate the generation of fine-scales near the nested domain inflow boundaries. The θ perturbation method is minimally dependent on the target turbulence, and instead can be based on the large-scale PBL conditions, making it simple to implement.

Despite the recent advances in turbulence-generation techniques, turbulence generation fetches continue to incur significant computational expenses: with the θ perturbation method, fetches on the order of tens of kilometers may be necessary for the proper turbulence scales to develop, with grid-cell sizes as low as 50 m (Mazzaro, et al., 2017). Ongoing research seeks to build upon the benefits of the θ perturbation method by using direct force perturbations, rather than θ perturbations.

6.2 The Force Perturbation Method

We developed a new perturbation method for turbulence generation, consisting of random vertical and horizontal forces applied at the inflow boundaries of highly resolved, grid-nested domains. This method was based on the cell-perturbation method (Muñoz-Esparza, et al., 2015 and 2018), which uses random potential temperature perturbations to trigger small-scale turbulent motions. By perturbing the flow with direct forces rather than through temperature gradients, we hope to gain more fine-tuned control over the turbulence generation, including the ability to apply different forcing magnitudes in different directions. We have implemented this method in the WRF model, and compared it with the θ perturbation method in an idealized setting for two atmospheric stability conditions: neutral and convective.

The random force perturbation method is implemented by superimposing random perturbations to the WRF tendency fields near the nested inflow boundaries. This is equivalent to adding random accelerations to the flow. As with the potential temperature perturbation method, the force perturbations are applied over two-dimensional cells with a size of 8x8 grid cells (Figure 6.1, Figure 6.2, and Figure 6.3). This size was selected by Muñoz-Esparza et al. (2014) as the minimum necessary to avoid numerical dissipation effects that can weaken the perturbations before the full turbulent cascade can develop. The orientation of the perturbed cells is chosen to be perpendicular to the direction of the perturbing force (Figure 6.2, and Figure 6.3). For example, a force perturbing the x-direction (Figure 6.2) will be applied over a cell of dimensions $[L_x,L_y,L_z] = [1,8,8]$ grid cells, while a force perturbing the z-direction (Figure 6.3) will be applied over [8,8,1] grid cells. We perturb a total of 24 grid cells along each inflow boundary. The perturbation magnitude at each cell is selected from a random uniform distribution. The entire perturbation field is refreshed after a period of time, t_d, calculated following the method described by Muñoz-Esparza et al (2015).

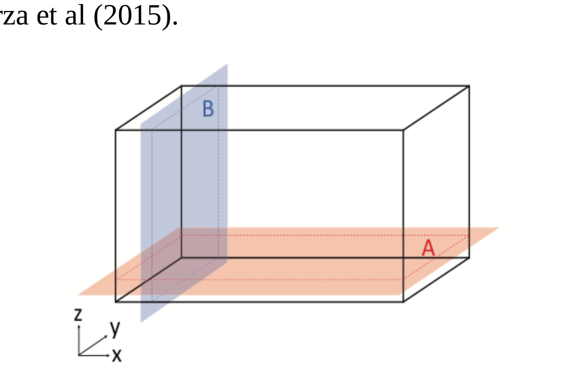

Figure 6.1. Diagram of the domain cross-sections shown in Figures 6.2 and 6.3.

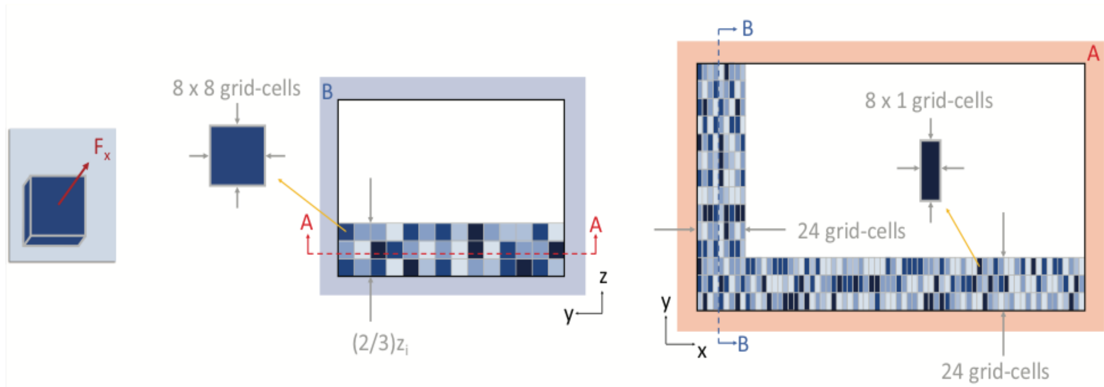

Figure 6.2. Force perturbation structure in the x-direction.

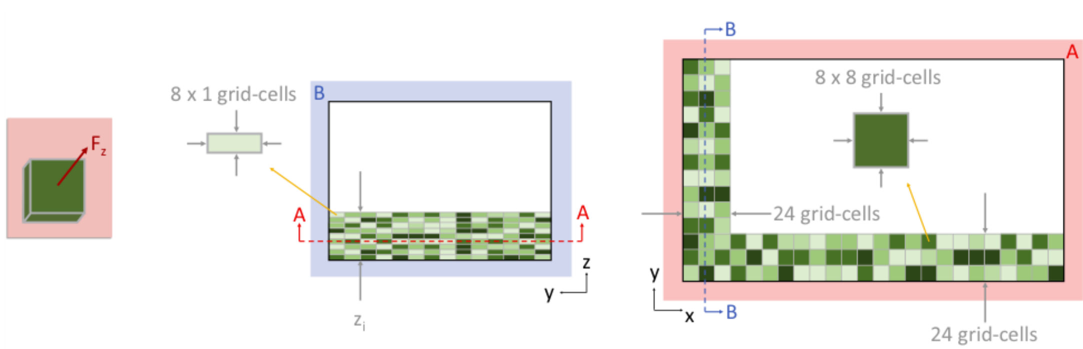

Figure 6.3. Force perturbation structure in the z-direction.

To assess its performance, the force perturbation is optimized for two different stability conditions: neutral and convective. The main optimization variables are the maximum perturbation amplitude for both, the vertical and horizontal force perturbations. Once an ideal maximum amplitude is identified for each stability condition, the force perturbation is compared to the potential temperature perturbation method setup as described by Muñoz-Esparza et al. (2015 and 2018). Finally, the effect of combining force and θ perturbations is tested.

6.2.1 Force and θ Perturbation Method Comparison

We performed a series of idealized, nested simulations under neutral and convective atmospheric stability conditions. The simulations are performed in flat terrain, with a surface roughness, z_o, of 0.1 m. There is no atmospheric humidity in these runs. Coriolis effects are equivalent to a latitude of 43.3°N. A geostrophic wind is applied in the x-direction, with a magnitude of $(U_g,V_g) = (10,0)$ ms^{-1} for the neutral case, and (8.1,0) ms^{-1} for the convective case. The boundary-layer depth is determined by an inversion layer at a height z_i = 500 m for the neutral case, and 2000 m for the convective case. Finally, a surface heat flux of 0.08 K-ms^{-1} was used in the convective case. The structure of the domains is shown in Table 6.1.

Table 6.1. Domain characteristics for the two stability conditions in this study, including horizontal resolution ($\Delta x, \Delta y$), vertical resolution (Δz), domain size (L), and spin-up times.

		Δx, Δy	Δz	$[L_x,L_y,L_z]$	Spin-up
Parent (Mesoscale)	Convective	999 m	20 m	[600,600,3] km	4 h
	Neutral	270 m	20 m	[58,25,1.5] km	24 h
Nest (LES)	Convective	47.57 m	20 m	[51,21,3] km	4 h
	Neutral	30 m	20 m	[54,21,1.5] km	4 h

Based on the configurations shown in Table 6.1, the neutral, nested LES was forced by a homogeneous flow, containing no turbulence (Figure 6.4a). However, the parent, mesoscale simulation for convective conditions contained coarse flow heterogeneities caused by the strong surface heat flux.

A series of force perturbation amplitudes were tested for both F_{xy} and F_z (Table 6.2). For each of these force perturbation directions, an optimal amplitude was selected based on the shortest x-direction distance necessary for the turbulent kinetic energy (tke) variations to be within 10% of a stable value.

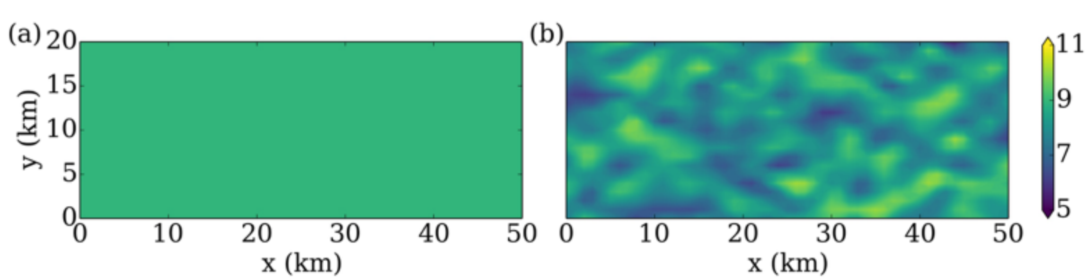

Figure 6.4. Horizontal contours of wind speed in the x-direction, u (m/s) at a height of 0.5 z_i for the periodic, mesoscale parent domains where (a) is neutral and (b) is convective.

The unperturbed, neutral case (N_{NP}) showed that the increase in resolution alone was not able to trigger turbulent motions from the smooth inflow. However, all of the convective stability cases, including the unperturbed case (C_{NP}), were able to produce fine-scale turbulence that stabilized within the simulated domains.

Table 6.2. Tested perturbation amplitudes.

	Neutral		**Convective**	
Method	Label	Amplitude	Label	Amplitude
-	N_{NP}	-	C_{NP}	-
θ (K)	$N_{\theta 0.5}$	0.5	$C_{\theta 0.33}$	0.33
F_{xy} (kg s^{-4})	N_{xy750}	750	C_{xy500}	500
	N_{xy1000}	1000	C_{xy1000}	1000
	N_{xy1250}	1250	C_{xy2000}	2000
F_z (kg s^{-4})	N_{z1000}	1000	C_{z5000}	5000
	N_{z1250}	1250	C_{z10000}	10000
	N_{z1500}	1500	C_{z15000}	15000
	N_{z1750}	1750	C_{z20000}	20000

One of the advantages of the horizontal force perturbation method (F_{xy}) is that it is implemented throughout the ABL depth without negative interactions with the inversion layer. Vertical contours show the development of tke for all heights within the ABL for the neutral stability case (Figure 6.5). A comparison of the optimal perturbation configurations, $N_{\theta 0.50}$, N_{xy1000}, and N_{z1250}, shows that the horizontal perturbations (F_{xy}) are the fastest to develop turbulence for all heights.

The θ perturbation method (Figure 6.5a) produces lower overall levels of turbulence than the force perturbation methods (Figure 6.5b and c). Horizontal contours of horizontal wind speed show a qualitative image of these lower turbulence levels (Figure 6.6). We observe that θ perturbations (Figure 6.6a) develop flows with higher mean wind speeds, but fewer small-scale fluctuations than the force perturbations (Figure 6.6b and c). This is also reflected in a comparison of turbulence spectra in the y-direction, at a distance of 40 km downstream of the inflow boundary (Figure 6.7), which shows that the θ perturbation method produces higher turbulent kinetic energy levels at low wavenumbers in the horizontal wind-speed field, and lower energy at higher wavenumbers (Figure 6.7a), when compared with both directions of the force perturbation method. Additionally, Figure 6.7 indicates that the θ perturbation method produces lower energy fluctuations of vertical wind speed for all wavenumbers (Figure 6.7b), and higher energy for all wavenumbers for the case of θ fluctuations. These observations of turbulence energy levels show that the conversion from θ fluctuations to kinetic energy fluctuations is not as efficient at producing fine-scale turbulent motions as directly increasing kinetic energy near the inflow boundaries with force perturbations.

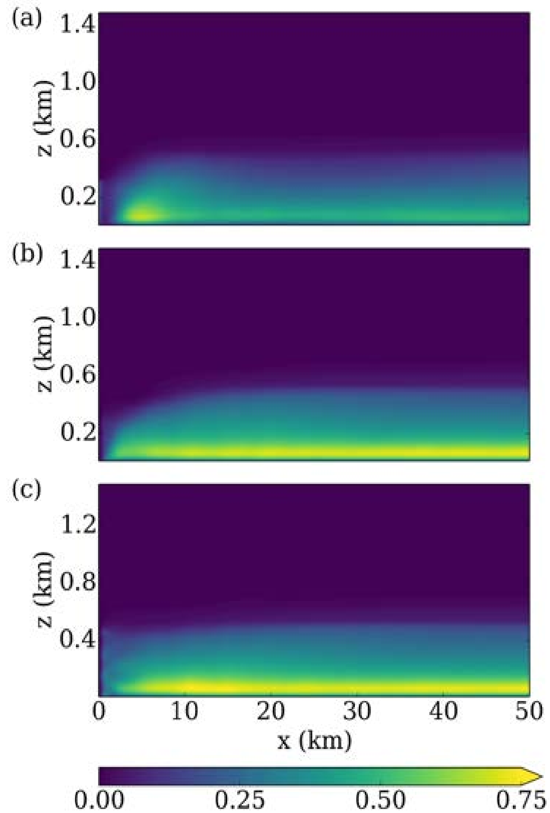

Figure 6.5. Evolution of tke, q (m^2s^{-2}), (a) $N_{\theta 0,s_r}$ (b) N_{z1250}, and (c) N_{xy1000}, as a function of distance downstream of the inflow boundary, x.

The case of convective atmospheric stability shows that all perturbation methods produce equal levels of turbulent spectra in the y-direction for u, w, and θ after a distance of 40 km. The strong heat flux in this case aids in the more rapid conversion of turbulent energy from θ fluctuations to the velocity fields.

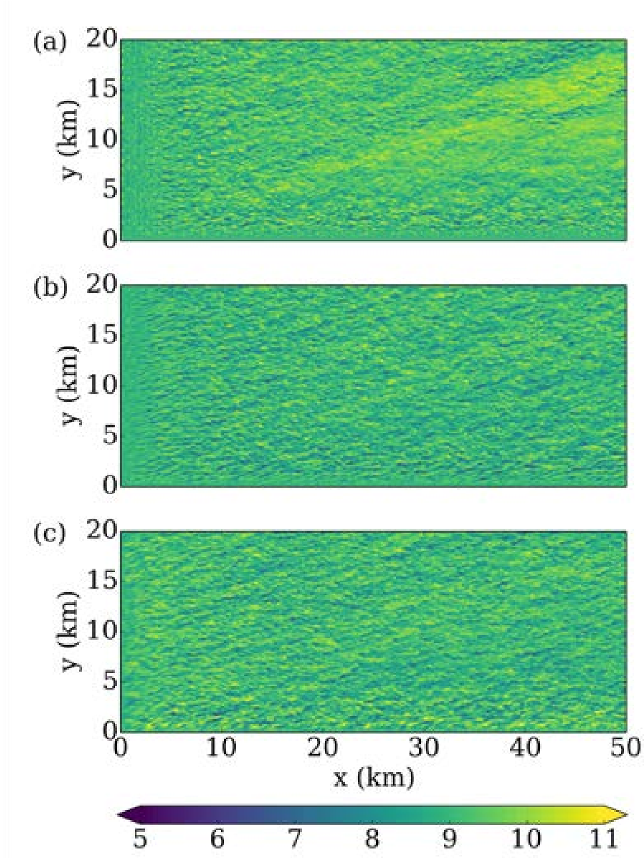

Figure 6.6. Horizontal contours of wind speed in the x-direction, u (ms^{-1}) at a height of 0.5 z_i = 250 m for (a) $N_{\theta 0,s_r}$, (b) N_{z1250}, and (c) N_{xy1000}.

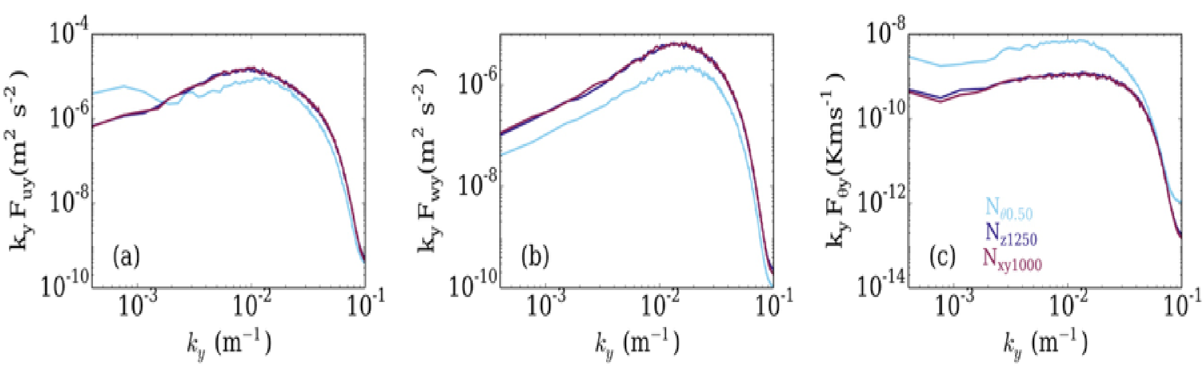

Figure 6.7. Turbulent spectra of u, w, and θ in the y-direction as a function of wavenumber, k_y for x = 40 km.

An analysis of the evolution of energy of the turbulent fluctuations for the convective case (Figure 6.8) shows that the vertical force perturbations, F_z, are the quickest to produce the consistent levels of turbulence observed at a downstream distance of 40 km. This result is observed for the three scalar fields considered (Figure 6.8g [u], Figure 6.8h [w], and Figure 6.8i [θ]).

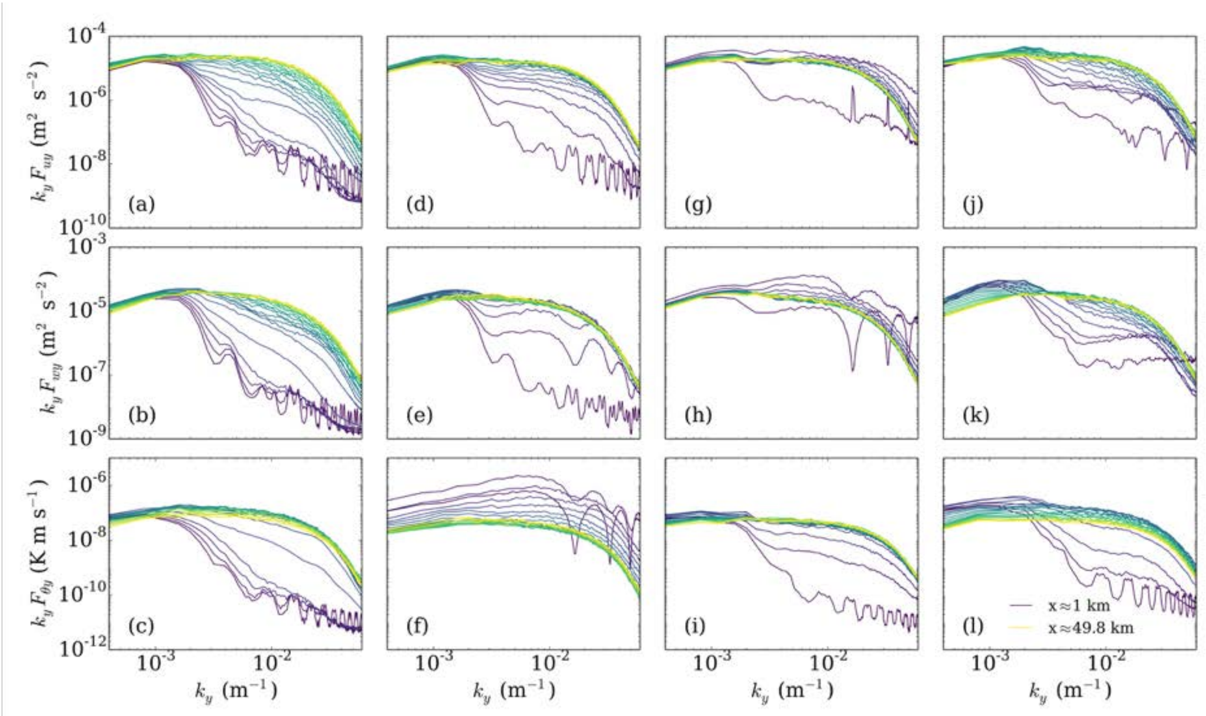

Figure 6.8. Turbulent spectra of u, w, and θ in the y-direction for (a,b,c) C_{NP}, (d,e,f) $C_{\theta0,33}$, (g,h,i) C_{z15000}, and (j,k,l) C_{xy1000} as a function of wavenumber, k_y, for a height of 1000 m.

Our analysis suggests that force perturbations produce faster turbulence development than the θ perturbation method. Additionally, we show that the directional application of the force perturbations is beneficial for cases with different atmospheric stability conditions: neutral stability conditions benefit most from horizontal force perturbations (Fxy), while convective stability conditions benefit most from vertical force perturbation (Fz). We would expect that a stable boundary layer would benefit most from horizontal force perturbation (Fxy), as vertical perturbations would be dampened by the stratification.

6.3 Using the SCPM to Improve Online-coupled Mesoscale-LES Simulation in WRF

Online-coupled mesoscale-to-LES simulations were conducted using a multiple-nested-domain configuration within the WRF model to examine the efficacy of the stochastic cell-perturbation method (SCPM) to improve the turbulence content of the simulated flow field on an LES domain embedded within a multiscale simulation. Two test cases from the SWiFT facility were utilized for comparison, a diurnal cycle occurring during 11/08-11/09 2013, and a frontal passage case occurring 05/12 2014. Data from the Texas Tech University 200 m instrumented tower were used for the evaluation. Initial coupled runs of these cases appear on our year 2 report (Haupt et al. 2017), but no perturbations were applied in those earlier runs.

The WRF simulations utilized for this study were configured with two successively refined LES domains located within two successively refined mesoscale domains. The simulations were forced by data from the NOAA NCEP GFS analysis, at 6-hourly frequency. No analysis or observational nudging was used during these simulations. The physics options chosen for all domains included the WRF Single-Moment (WSM) three-class simple ice scheme for cloud microphysics, the Dudhia shortwave and RRTM longwave radiative transfer schemes, the Monin-Obukhov (Janjic Eta) Similarity scheme for the surface layer, and the Noah land surface model. The two mesoscale domains used the Mellor-Yamada-Janjic tke-based PBL turbulence scheme, while the LES domains used the 1.5-order tke-based SFS scheme. The outermost mesoscale domain also used the Kain-Fritsch cumulus scheme. Other configuration choices were standard, including 3rd and 5th order advection operators.

Horizontal mesh spacings of 6050, 550, 50, and 10 m were utilized on the four domains. A variable number of vertical mesh levels were utilized, with the outer two mesoscale domains using a standard mesoscale grid with 51 vertical levels and grid spacings beginning with (approximately) 20 m spacing near the surface, while the LES domains used 109 and 205 vertical levels, with 10 m and 5 m on the coarse and file LES domains, respectively. All of the vertical grids were stretched, to a model top of 200 hPa. Implicit vertical velocity damping was applied to the uppermost 5000 m. The simulations were spun up for several hours in mesoscale mode prior to the LES nests being instantiated one hour prior to the period of examination of the model output, which focused on the innermost LES domain.

6.3.1 Diurnal Cycle Case

Figure 6.9, Figure 6.10, and Figure 6.11 depict the evolution of the simulated and observed potential temperature (θ), wind speed (U), and turbulent kinetic energy (tke, resolved portion only from the simulations) during the diurnal cycle case, from the late morning through the overnight hours. Top panels show 20-minute average simulated (lines) and observed (squares) values, while bottom panels show simulated (solid) and observed (dashed) profiles from the middle 20-minute average value each hour. Observed and simulated data were averaged from 1 Hz output, with simulated data consisting of the full vertical profile of relevant state variables from the innermost LES domain at the location closest to the SWiFT tower, (latitude, longitude) = (33.6105, -102.0505). Left and right panels show simulations without and with the SCPM, respectively.

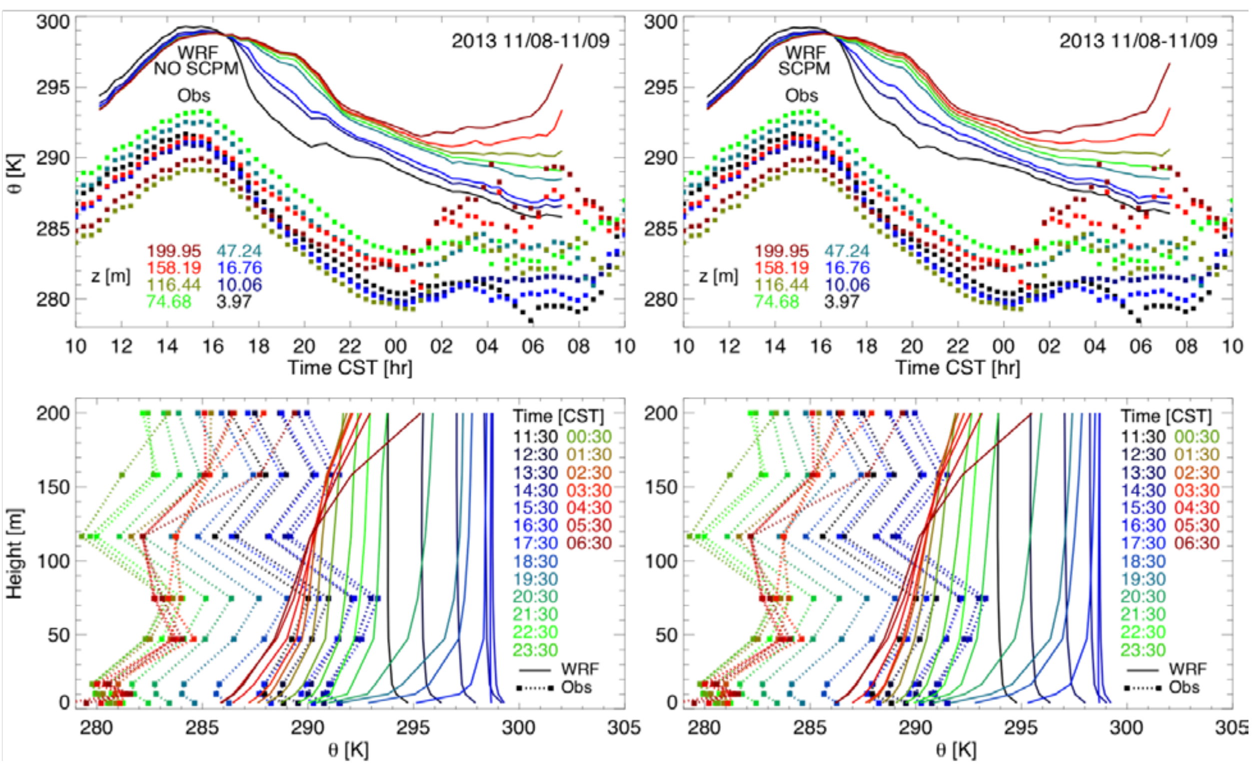

Figure 6.9. Simulated versus observed potential temperature from the diurnal cycle case.

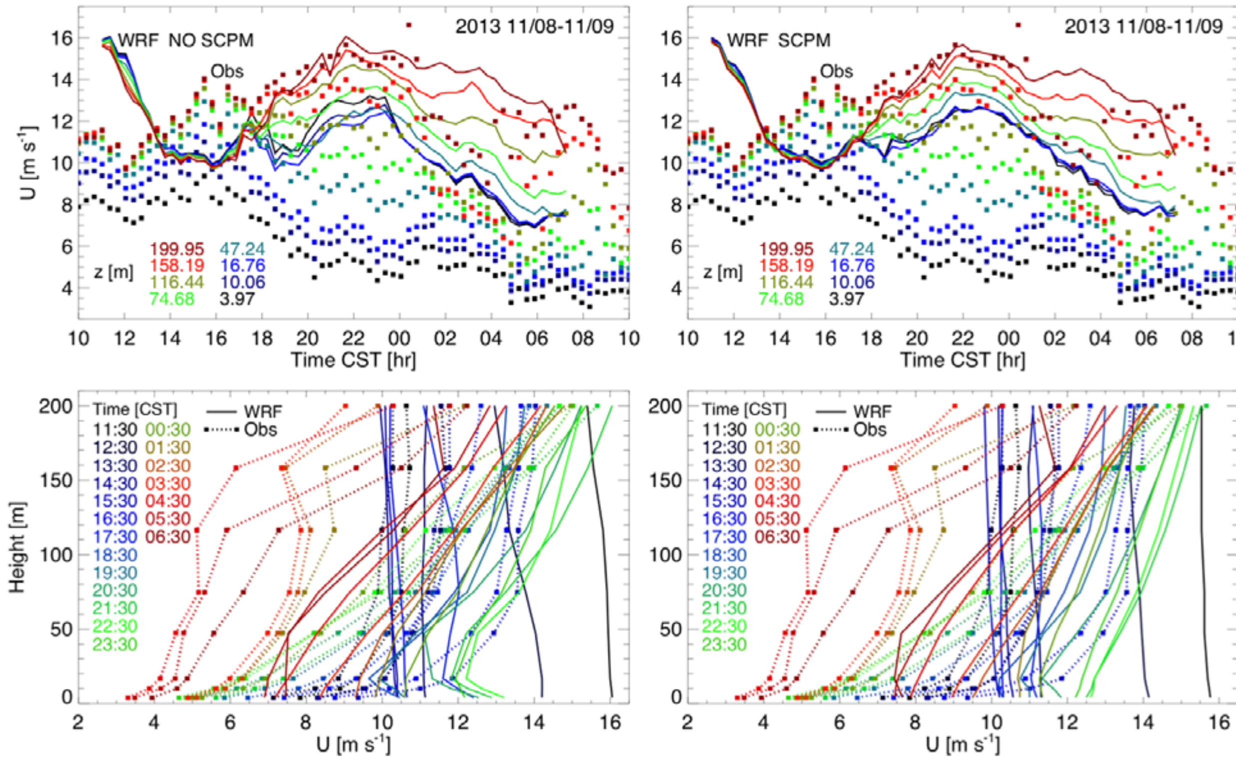

Figure 6.10. Simulated versus observed wind speed, as in Figure 6.9.

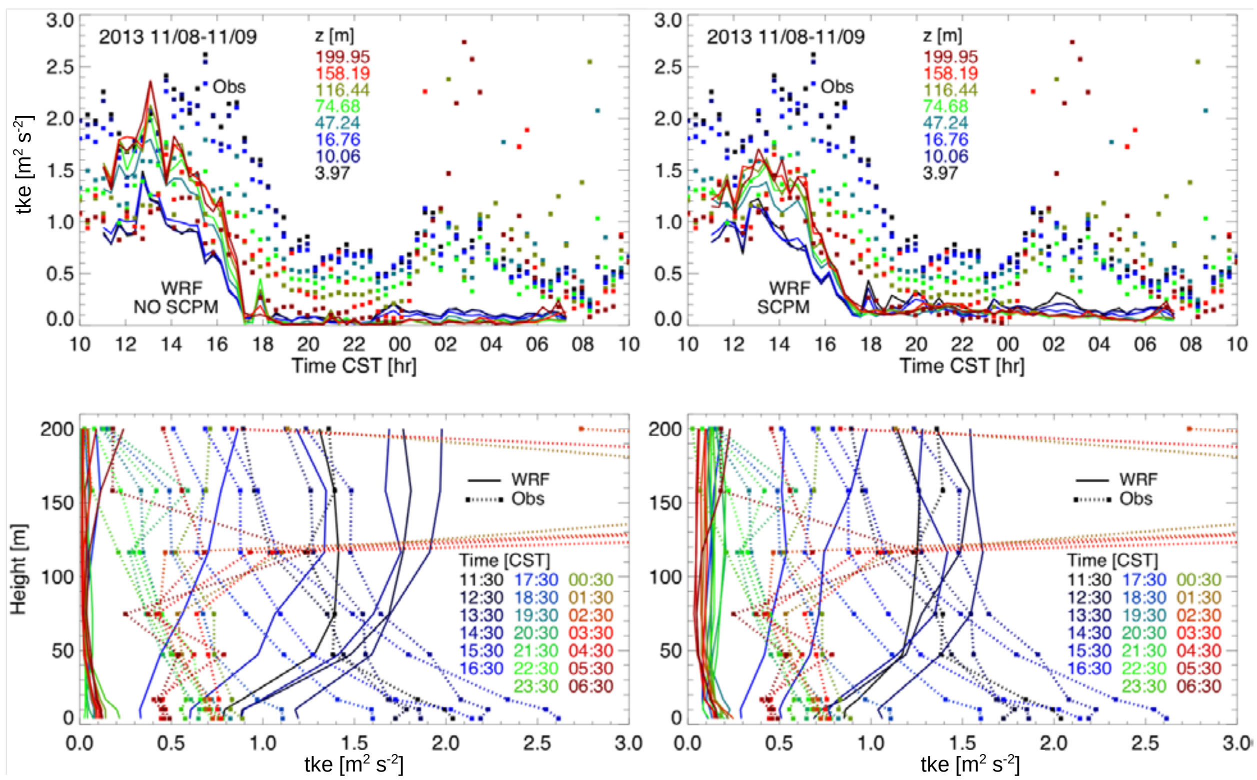

Figure 6.11. Simulated versus observed turbulent kinetic energy, as in Figure 6.9.

The diurnal case is characterized by moderate and steady wind speeds near the surface, rotating from predominantly southerly to southwesterly, with changes of stability controlled by the solar cycle, as described in more detail in section 2.2. Figure 6.9 shows that the simulations correctly capture the diurnal trend of θ, albeit with a significant warm bias. The observed values (dashed lines in lower panels, shown each hour) feature a persistent sawtooth pattern, indicating that some of the sensors may have been out of calibration. This feature makes it impossible to assess whether the simulations are accurately depicting the temperature variability occurring across the height of the tower. However, both the simulations and observations show a larger range of values during the latter portion of the period, suggesting the development of stably stratified conditions. The SCPM is seen to have almost no effect on the potential temperature field during either convective or stably stratified conditions.

Figure 6.10 shows that the simulations likewise capture only the general trends of the observed wind speeds during the period, again indicating an increased shear during the overnight hours that qualitatively matches the observations. The simulations exhibit almost uniform wind speed across the grid cells spanning the tower during the convective portion of the cycle, while the observations show considerable shear. The SCPM is again seen to have very little effect on the wind speeds, except a slight overall reduction of shear, due again to the strong constraint imposed by the bounding domain mass flow solution.

An explanation for the lack of shear in the simulated U profiles is the coarse vertical grid spacing used on the outermost mesoscale domains, which only place a few model grid points within the span of the tower. While the nested LES domains use much finer vertical resolution, capable of resolving significant shear, wind speeds in online-coupled simulations are strongly constrained by the bounding domains' solution, which defines the mass flow through the nested domains. The idealized simulations of the convective portion of this diurnal cycle case study conducted during the MMC in FY15 and FY16 and reported in Mirocha et al (2018; see Figure 15) featured more realistic vertical shear profiles, due in part to the use of periodic lateral boundary conditions, and therefore the constraint of an under-resolved near-surface mesoscale flow field.

Figure 6.11 shows that the simulations also capture the overall trend of the observed tke over the diurnal cycle but do not consistently achieve correct magnitudes and tend to predict uniformly increasing values with height, in opposition to observed values, which always exhibit a near-surface maxima, even when larger magnitudes are observed aloft. The SCPM has a much more noticeable influence on the simulated tke values than those of θ and U. During the convective portion of the cycle, the SCPM reduces the over-prediction of tke values at upper tower heights, due to the development of scales of motion that can dissipate energy from the large convective plumes that develop within the LES domains due to strong surface heating. During the stable portion of the cycle, the SCPM maintains larger resolved tke values, but magnitudes remain significantly smaller than observed values. The simulations fail to capture the very large tke values occurring at the upper tower heights during the latter stages of the period, likely the result of wave activity in the stably stratified environment. Potential reasons for this underprediction include both inadequate representation of unresolved terrain and surface vegetation heterogeneity, as well as shortcomings of the conventional implementation of the surface boundary condition in the LES domain, as described in Section 6.3.3.

Figure 6.12 shows instantaneous plan views of the wind speed at approximately 100 m above the surface during four different times during the diurnal case study, representing four different stability regimes, including strongly convective (Figure 6.12a, e), weakly convective (Figure 6.12b, f), nearly neutral (Figure 6.12c, g), and moderately stable (Figure 6.12d, h) conditions, both without (Figure 6.12a—d) and with (Figure 6.12e—h) the SCPM applied. Figure 6.12 shows that application of the SCPM noticeably increases the range of scales resolved during each of the snapshots, especially during weaker forcing conditions, leading to the appearance of a more realistic turbulence field, even though simulated tke values are significantly lower than their observed counterparts.

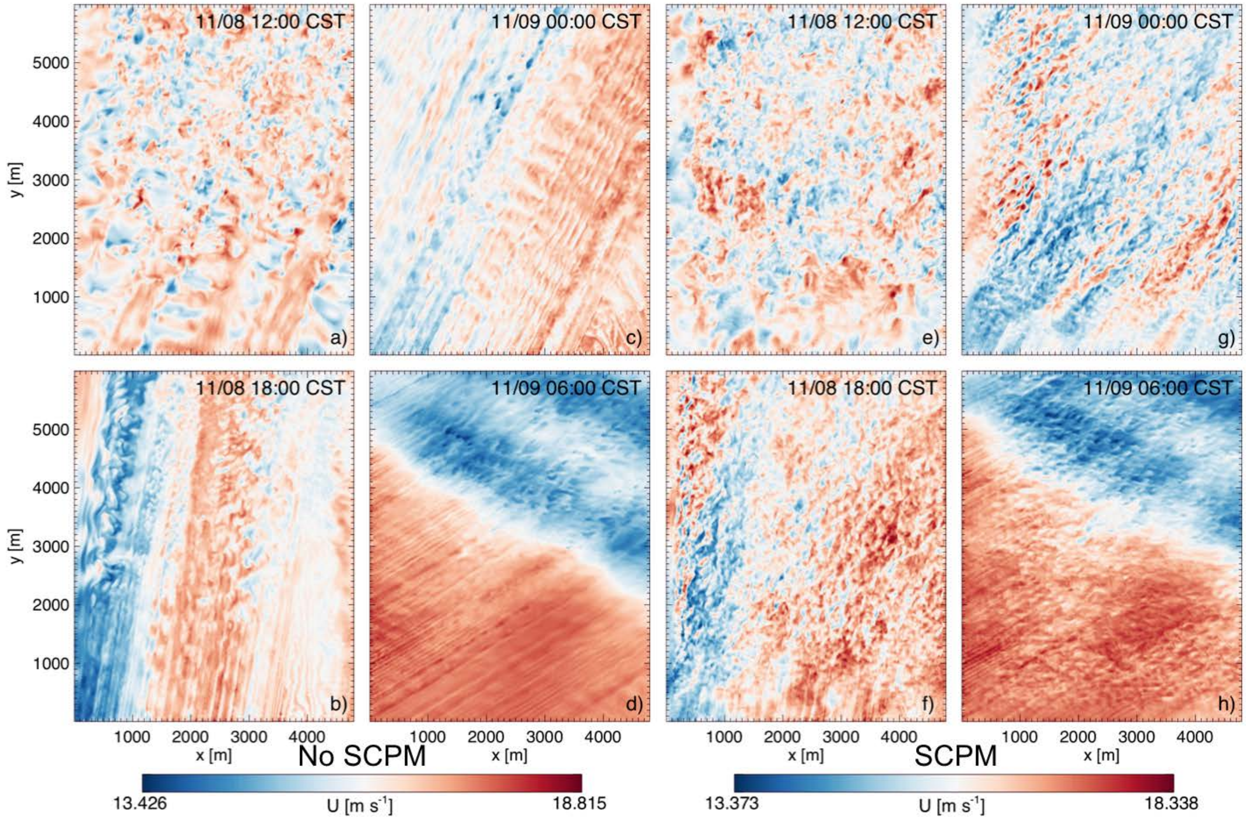

Figure 6.12. Instantaneous snapshots of simulated wind speed at 100 m above the surface from four times during the diurnal cycle, featuring four stability regimes, including strongly convective (a,e), weakly convective (b,f), nearly neutral (c,g), and moderately stable (d,h), both without (a,b,c,d) and with (e,f,g,h) the SCPM.

6.3.2 Frontal Passage Case

The diurnal cycle case is characterized by the passage of a cold front, coincident with a change of wind direction from southerly to northerly, with generally decreasing wind speeds throughout the period. The case study features a decrease of static stability, from moderately stable prior to the frontal passage, to more weakly stable thereafter, due to the post-frontal advection of cooler air from the north, weakening the surface-to-air temperature gradient.

Figure 6.13 shows that the simulations are able to approximately capture the timing of the arrival of the frontal passage, but significantly underestimate the magnitude of the cooling thereafter. As with the diurnal cycle case, the observed values (dashed lines in lower panels, shown each hour) again feature a persistent sawtooth pattern, making it impossible to assess whether the simulations are accurately depicting the temperature variability occurring across the height of the tower. The SCPM again is seen to have almost no effect on the potential temperature field.

Figure 6.14 shows that the simulations are able to generally capture the wind speeds during the period, albeit with somewhat reduced shear, including a brief period of slower wind speeds with small shear occurring about an hour later than the occurrence of a similar feature within the observations. As with temperature, the SCPM is again seen to have little effect on wind speeds.

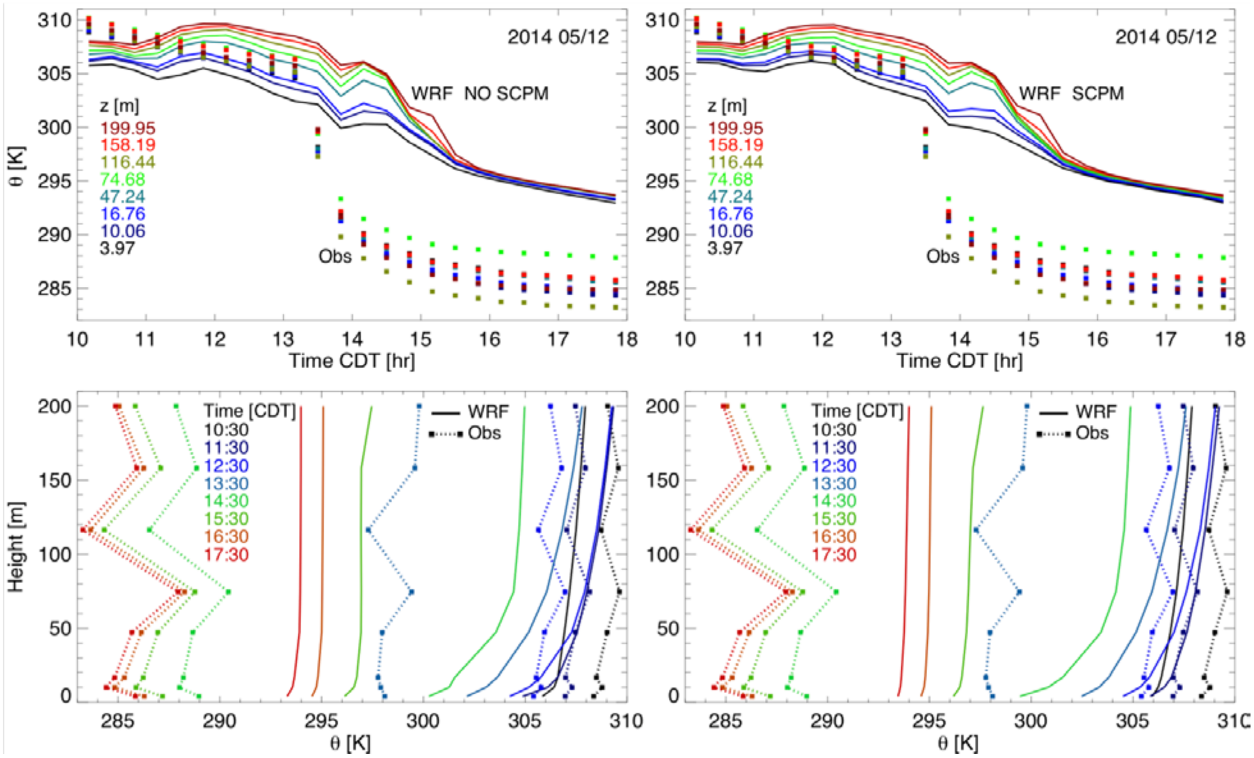

Figure 6.13. Simulated versus observed potential temperature from the frontal passage case.

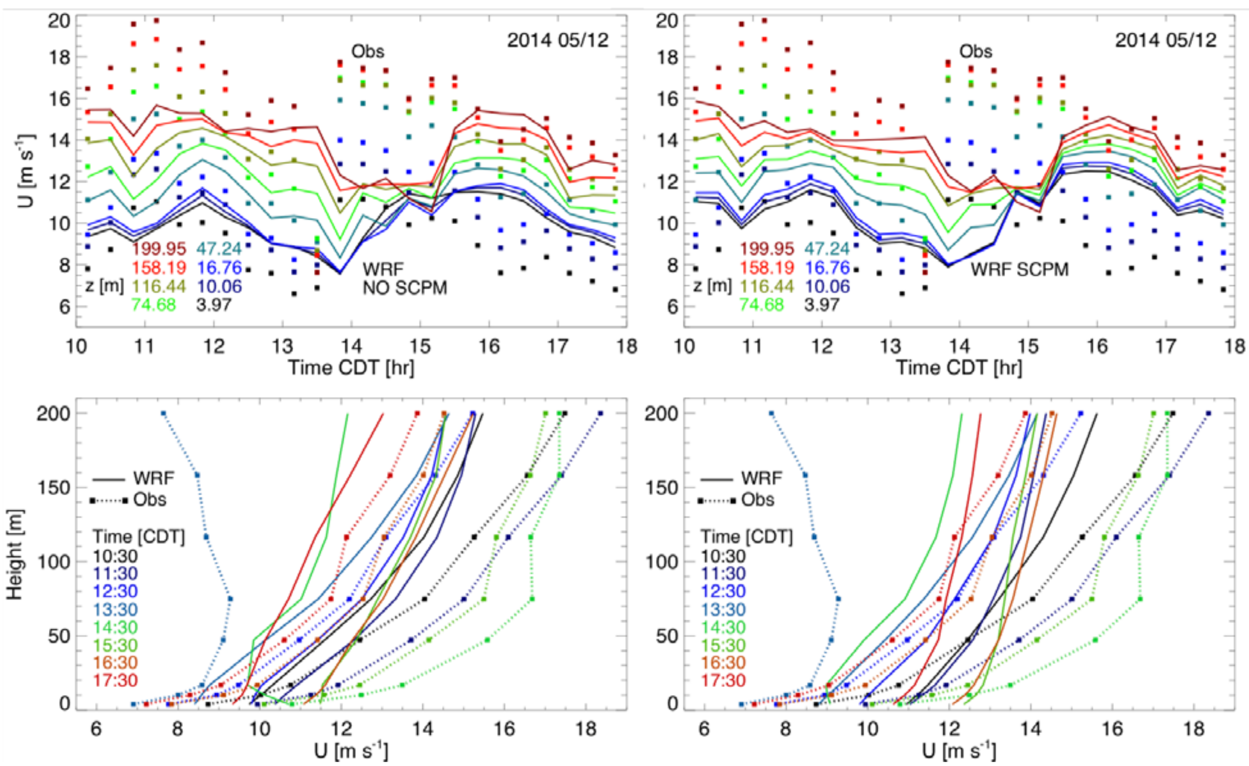

Figure 6.14. Simulated versus observed wind speed from the frontal passage case.

Figure 6.15 shows that the simulations are able to capture some features of the observed tke trajectory, but again fail to consistently achieve correct magnitudes, and again tend to predict uniformly increasing values with height. The SCPM has little effect on tke prior to the passage of the front, except a reduction of one spike early in the period. However, the SCPM increases tke values after the passage, although again produces smaller than observed values.

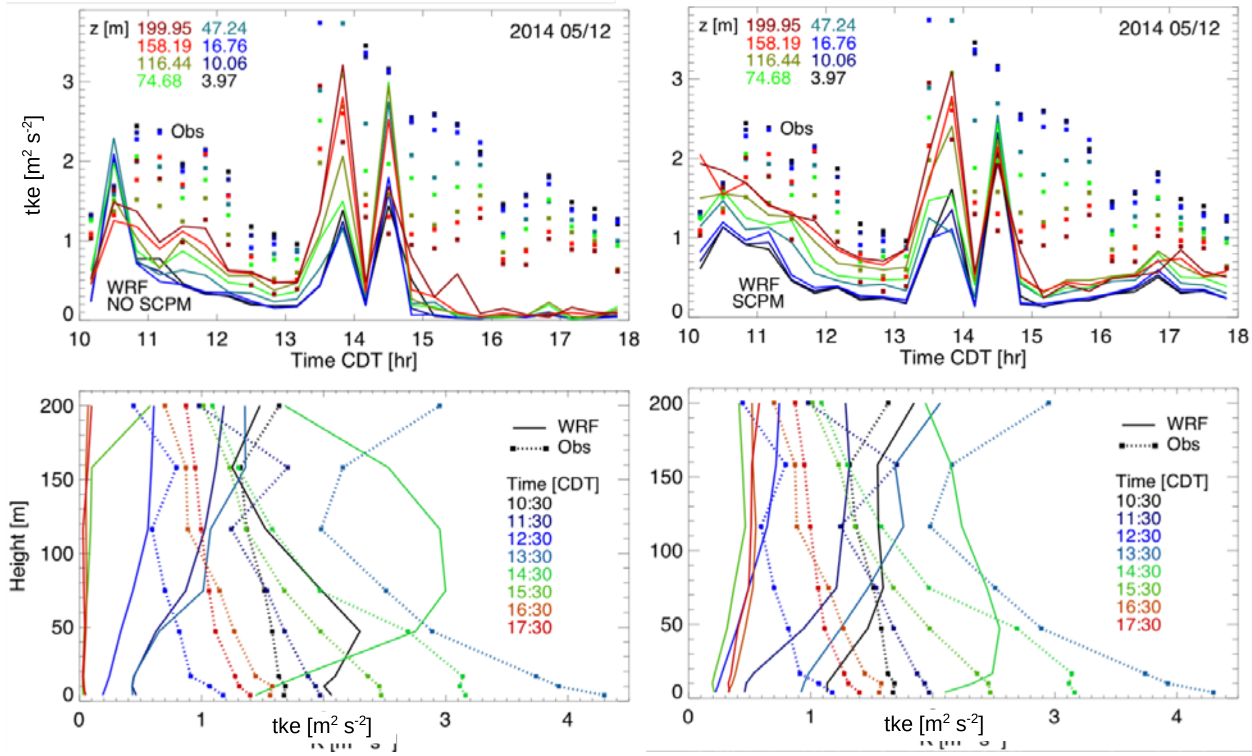

Figure 6.15. Simulated versus observed turbulent kinetic energy from the frontal passage case.

Figure 6.16 shows instantaneous plan views of the wind speed at approximately 100 m above the surface during two times, one before (Figure 6.16a,c) and one after (Figure 6.16b,d) the passage of the front, both without (Figure 6.16a,b) and with (Figure 6.16c,d) the SCPM. Again, the SCPM noticeably increases the range of scales resolved during each of the snapshots, leading to the appearance of a more realistic turbulence field, especially during the post-frontal portion of the period.

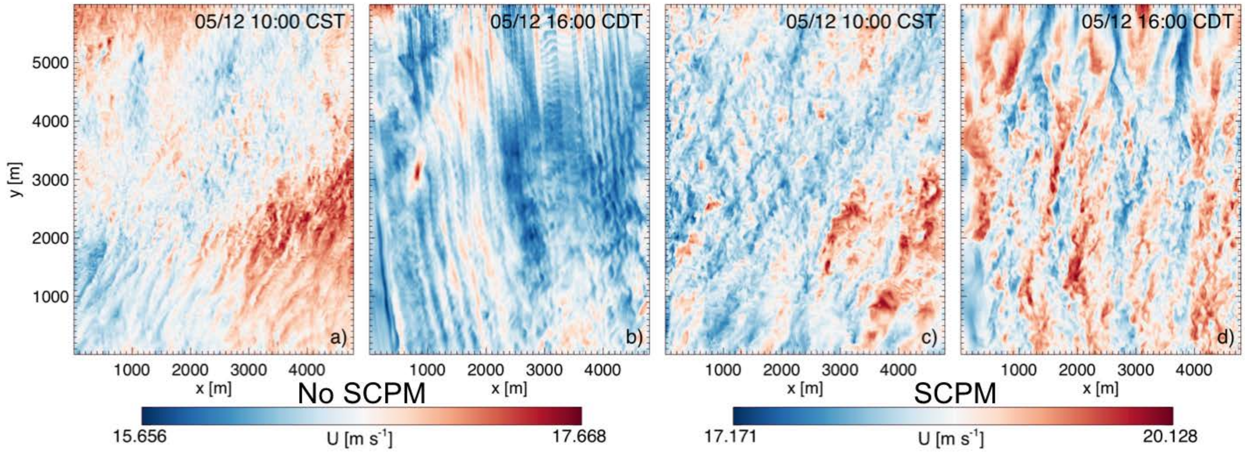

Figure 6.16. Instantaneous snapshots of simulated wind speed at 100 m above the surface from before and after the frontal passage, both without (left) and with (right) the SCPM, as in Figure 6.12.

6.3.3 Discussion and Conclusions

Fully online-coupled MMC simulations of these two case studies from the SWiFT facility using the WRF model are able to capture several important features of the observed flow field; however, the agreement is not perfect. The simulations generally do not capture the potential temperature (θ) well, with distinct warm biases during all of the diurnal cycle case study, and following the passage of the cold front during the frontal passage case. Wind speed (U) was generally captured better than θ, but significant biases were likewise present, with the simulations generally capturing too little vertical shear, especially during the convective portion of the cycle. Turbulent kinetic energy (tke) was also generally under-predicted during all but the strongly convective portion of the diurnal cycle, and during the passage of the front.

Application of the SCPM has only minimal impact on θ and U, but does improve tke overall, although the simulations still produce smaller than observed tke values during the stable portions of each period. The SCPM also reduces the over-prediction of tke at the upper tower heights during the convective portion of the diurnal case study by providing dissipation of the convectively forced plumes that developed upon inflow to the LES domain. The simulations likewise fail to capture the increase of tke approaching the surface occurring in most of the observed tke profiles. However, some reduction of tke approaching the surface from the simulations is expected among the lowest few height levels, since those profiles contain only the resolved component.

A possible explanation for the simulations to under-predict tke values during the near-neutral and stable portions of the diurnal cycle is the existence of unresolved terrain and surface vegetation heterogeneity, each of which can enhance tke production near the surface in the absence of convective instability. Figure 6.17 shows profiles of simulated (resolved) tke relative to observed values during an idealized near-neutral case study from the SWiFT facility also showing under-predictions using not only WRF but also two other solvers (Mirocha et al 2018). While tower wake contamination was surmised to have augmented the observed values during 08-17, the 07-10 observations are considered uncontaminated, and still show significantly enhanced tke values.

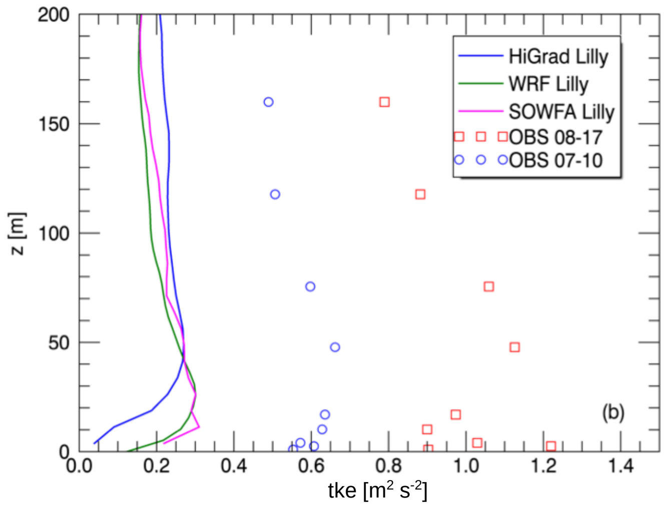

Figure 6.17. Profiles of simulated tke (lines) and observations (dots).

A second issue potentially impacting the underprediction of tke is the implementation of the surface boundary condition within the LES domains of WRF, and in the other solvers used in Mirocha et al (2018), which may suppress flow variability near the surface. A novel approach to treating the surface boundary condition as a distributed drag term, which has been shown to enhance resolved tke values in neutral flow simulations, is described briefly in Chapter 7 herein, and more fully in Arthur et al (2018).

6.4 Using Perturbations to Accelerate Turbulence Transition under Mesh Refinement with LES

While perturbations have shown promise in accelerating the development of turbulence upon a mesoscale inflow entering a simulation with a mesh spacing fine enough to resolve turbulence explicitly, subsequent mesh refinement from a coarser- to a finer-scale mesh within the turbulence-resolving simulation likewise produces a transition of the turbulence field resulting from a lag between the reduction of the grid spacing and the development of finer-scale turbulence motions resolvable on the finer mesh. As is the case with mesoscale inflow, the length scale of this secondary transition under further mesh refinement can be extensive, requiring in excess of several hundred computational grid cells under moderate flow velocities in the absence of strong convective forcing (Mirocha et al, 2017).

The turbulence equilibration process under coarse-to-fine LES mesh refinement was examined in an idealized LES setup featuring a coarsely resolved outer-domain LES, using periodic lateral boundary conditions, with a finer-scale nest embedded within. As the nest receives its lateral boundary conditions from the parent domain, perturbations were placed along the inflow boundary (west) of the nested domain. The evolution of the turbulence field within the nested domain was then examined as a function of distance from the inflow boundary. Both temperature and velocities were perturbed, with the latter using two different magnitudes of forcing of the velocities. Perturbation cell sizes were also varied between 4 and 8 grid points in the vertical, and 1 and 4 grid points in the vertical, and both 3 and 6 strips of perturbations cells were examined.

All of the simulations were forced with a geostrophic wind of 10 m s^{-1} oriented from a northwesterly direction, such that the counterclockwise rotation of the flow approaching the surface (due to the Coriolis acceleration, assuming the latitude of 30 degrees) resulted in flow being very closely aligned with the x-direction at 100 m above the surface. Figure 6.18 and Figure 6.19 show spectra of the u (streamwise), v (cross stream), and w (vertical) velocity components in the y-direction as functions of distance from the x-inflow boundary within the nested domain. Spectra are shown relative to domain-averaged counterparts obtained from a stand-alone (SA) LES with the same domain size and mesh spacing as the nested domain, but run with periodic lateral boundary conditions. Results using both the Smagorinsky (SMAG) and Lagrangian Averaged Scale-Dependent (LASD) SFS stress models are shown, along with a few different cell-perturbation approaches, as labeled on the figures. The turbulence equilibration process can be viewed as the progression of the shape of the spectra with increasing distance throughout the nested domain. As described more thoroughly in Mirocha et al (2017), the equilibration process involves both a somewhat rapid development of smaller scales, which increase higher-frequency spectral content, as well as slower changes to the low-frequency spectral content.

Figure 6.18 shows the spectral equilibration from four nested domain simulations, two using the SMAG and two using the LASD model (as labeled), both with no SCPM (Figure 6.18a-f) and with the standard SCPM of Muñoz-Esparza (2015), using three strips of potential temperature perturbations along the inflow boundary (Figure 6.18g-l). The standard application of the SCPM best suited to triggering turbulence development from a mesoscale inflow does not improve the equilibration process from coarse-to-fine LES refinement, instead causing larger departures of low-frequency power and slower equilibration. This result is perhaps unsurprising, as the optimal choice of cell sizes to trigger the entire turbulence cascade is likely to be different than that which best triggers smaller inertial scales to form within a simulation already resolving the largest scales of turbulence.

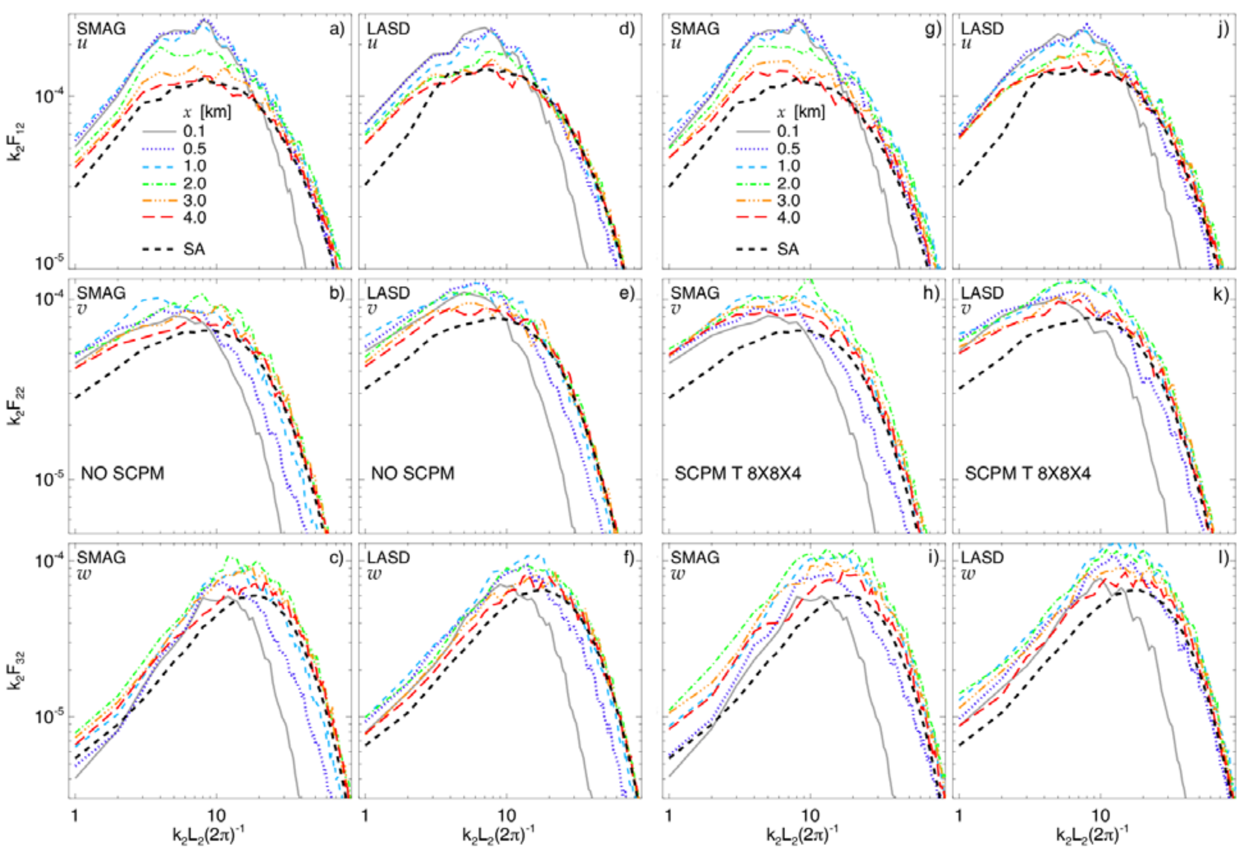

Figure 6.18. Spectra of all three flow components at 100 m above the surface within the nested domain, as functions of distance (colored lines), relative to the stand-alone (SA) value (black dashed lines) obtained from a simulation using periodic lateral boundary conditions.

Figure 6.19 shows the impact of perturbing the horizontal velocity components relative to θ, using both the same perturbation cell geometries, and also using smaller cell sizes, as labeled on the figure panels. Perturbing velocity rather than θ, and using smaller cells, each appear to slightly enhance the rate of attenuation of the largest scales, which is the slowest part of the equilibration process. Here, for brevity, results are only shown for the SMAG simulations; however, results were qualitatively similar using the LASD model.

The flow equilibration process can also be viewed from the evolution of U and K within the nested domain. Figure 6.20 and Figure 6.21 show profiles of U (Figure 6.20a,c,e,g and Figure 6.21a,c,e,g) and K (Figure 6.20b,d,f,h and Figure 6.21b,d,f,h) at five of the six inflow distances shown for the spectra (with the profile nearest the inflow omitted from the K analysis due to the slow evolution of K relative to the spectra). The rapid increase of K followed by a gradual reduction is related to the temporary disconnect of resolved structures from dissipation during the time required for smaller scales to form on the refined mesh, followed by the gradual dissipation of that excess energy. Profiles of U show little evolution, as those are primarily fixed by the bounding domain solution at the nest boundaries, which constrains the mass flow within the nested domain. The SA solution, obtained using the same forcing as the bounding domains solution from the nested simulations, but with a finer mesh spacing, indicates the impact of mesh spacing and domain size on U.

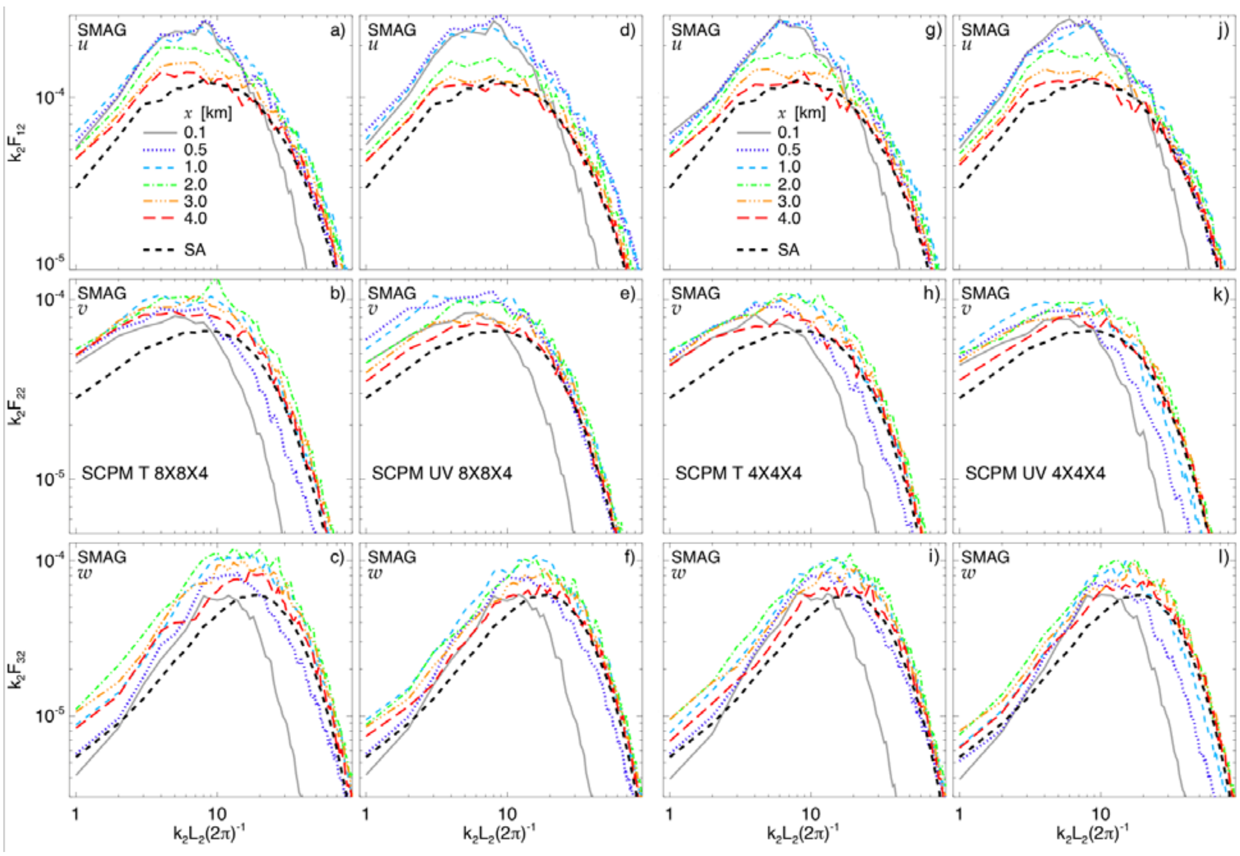

Figure 6.19. Spectra, as in Figure 6.18, using the SCPM, as specified in the figure panels.

The much larger over-predictions of K under the standard SCPM, shown in Figure 6.20 f,h are consistent with the impact of the perturbations on the spectra, again showing that the SCPM configuration optimized for mesoscale inflow is not appropriate for an inflow with resolved turbulence.

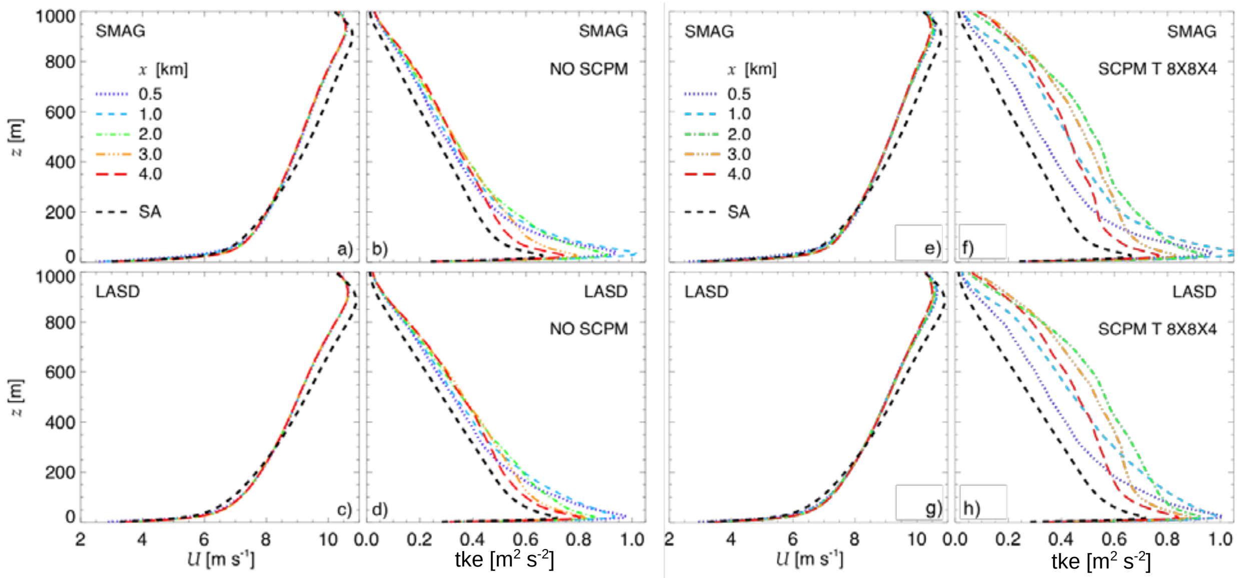

Figure 6.20. Profiles of U and tke within the nested domain, as functions of distance (colored lines), relative to the stand-alone (SA) value (black dashed lines) obtained from a simulation using periodic lateral boundary conditions.

Figure 6.21 shows U and tke profiles from simulations using the same variants of the SCPM as shown for the spectra in Figure 6.19, featuring perturbations to the velocity components, and using smaller cells. As with the corresponding spectra, each of these changes led to better performance than the standard SCPM, with velocity perturbations leading to faster equilibration overall, and with the smallest perturbations (Figure 6.21g,h) leading to slightly more rapid equilibration than the unperturbed case, especially at the heights of a characteristic turbine rotor.

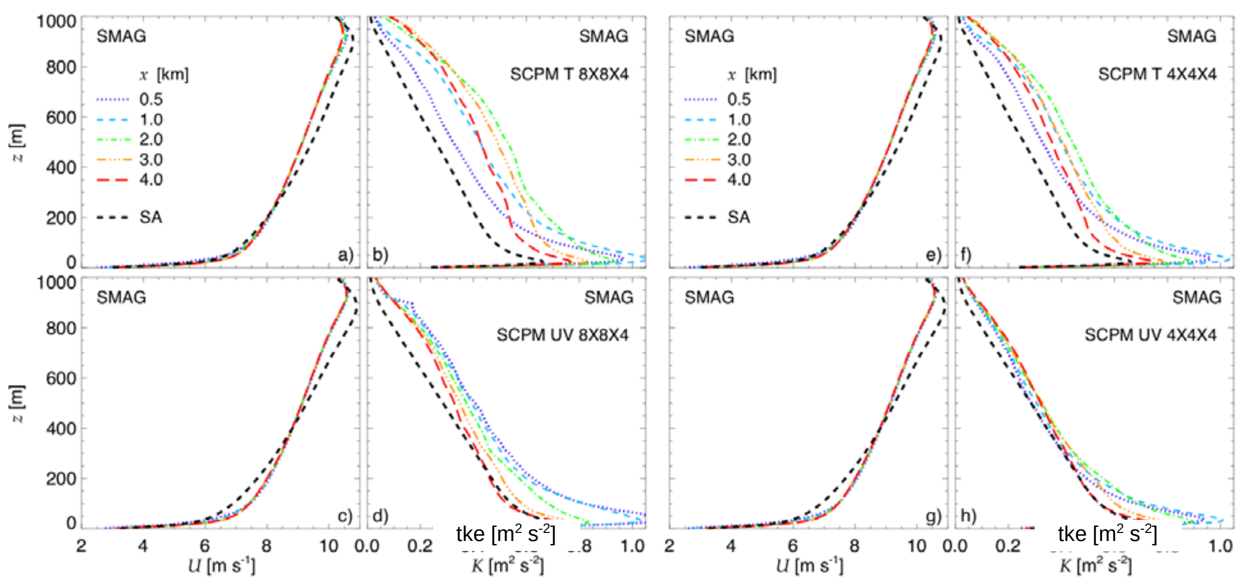

Figure 6.21. Profiles of U and tke, as in Figure 6.20, using inflow perturbations as specified in the figure panels.

The improvements of the turbulence equilibration process afforded by the use of velocity perturbations with relatively small cell sizes, while modest, motivate continued exploration of different force magnitudes, cell sizes, and cell geometries as a means to further improve the fidelity of mesh refinement within turbulence-resolving domains. The improvements may be more substantive when using larger horizontal mesh refinement ratios than the factor of 3 used herein.

6.5 Generating Inflow Turbulence using Observational Data

In nested simulations, turbulence develops slowly near the inflow boundary due to the mismatch of scales as well as differences in the turbulence models used on the nested domains. To speed up the development of turbulence in coupled simulations, the use of perturbation methods (e.g., Muñoz-Esparza, et al. 2014) that are deployed along in the domain boundary is becoming popular. In this section, we investigate an alternative approach by building the velocity fluctuations from observations (i.e., vertical profiles of wind components) using stochastic methods, such as the one developed by Veers (Veers 1988). This method uses spectra from observational data and empirical coherence functions to predict the time series of velocity in the inflow plane. In addition to the Veers method, a synthetic method – the Mann method (Mann 1998) **-** is also used to produce perturbations. The turbulence fields are added to the flow field simulated with coarser resolution that has the mesoscale forcing footprints. This flow field is used as the lateral boundary forcing into the microscale domain.

The observational data were collected from six heights on the SWiFT tower (ranging from 10 m to 100 m) using sonic anemometers. Using these data, we estimated the turbulence field for a nocturnal case. Figure 6.22a shows a snapshot for three velocity components for a horizontal plane at a height approximately 90 m above surface from simulations that use no turbulence perturbations (left column) and that use turbulence perturbations at the lateral boundary generated from the Veers method (right column). The flow field in the first column shows almost no turbulence over the entire domain, indicating that it is difficult to develop turbulence in stable conditions. On the other hand, the flow structures in the right column indicate development of turbulence over the entire domain for all velocity components using the Veers method. This result clearly indicates that adding the turbulence perturbations using the Veers method helped to develop the turbulence. Similar flow structures were obtained using the turbulence generated by the Mann method at the lateral boundary (not shown here). Moreover, the turbulence decreases more quickly with height than is seen for the Mann method.

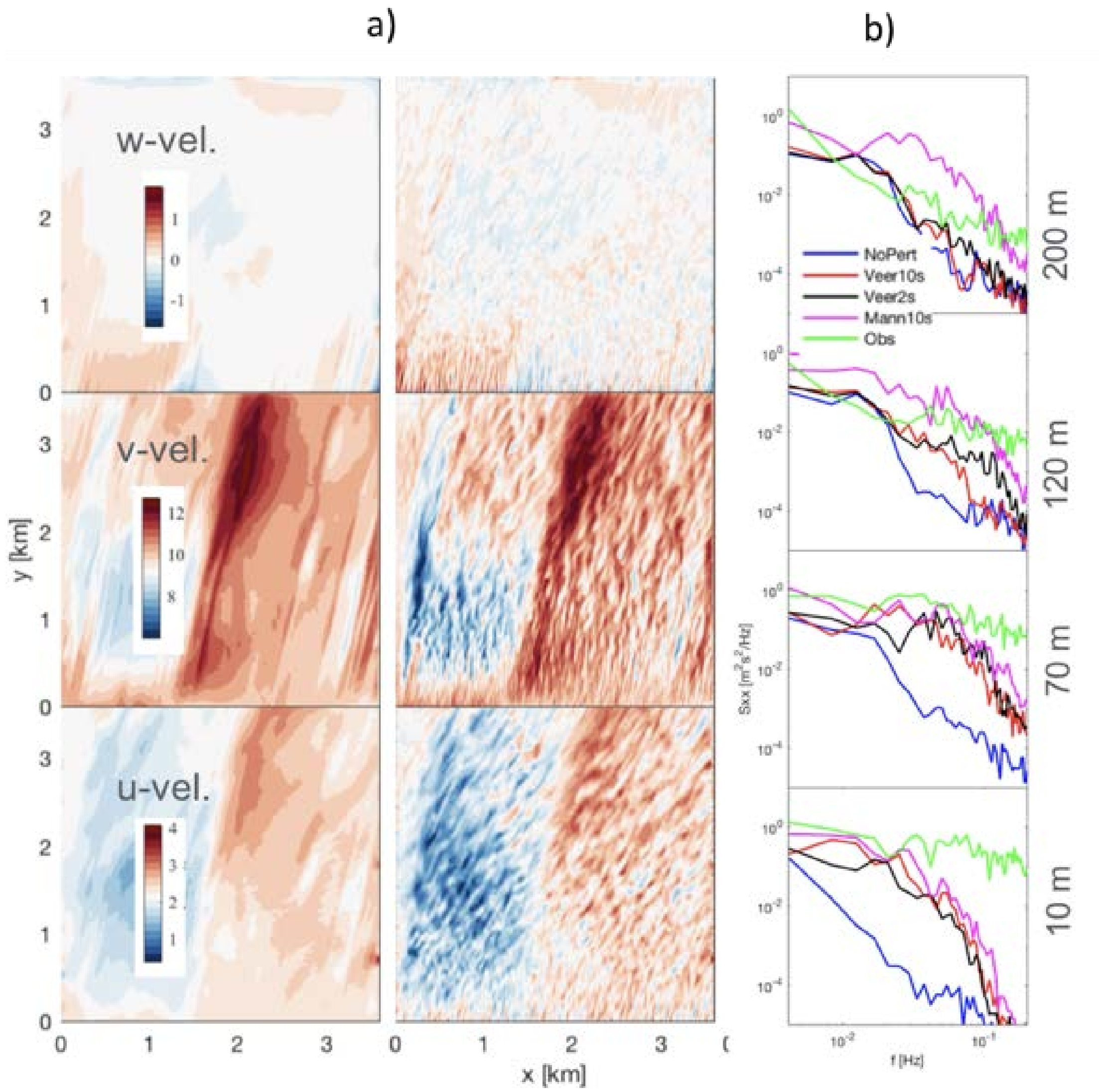

Figure 6.22. a) Instantaneous u-, v- and w-component velocity from unperturbed (left column) and perturbed (middle column) simulations. b) Spectra at different vertical heights from simulations with perturbed and unperturbed boundary conditions with different update frequencies.

For a more quantitative comparison, the spectral energies using these two inflow generation methods were calculated at the six tower heights (Figure 6.22b). The spectra resulting from the use of the Veers method show a gradual decrease of resolved turbulence that is similar to the observations. For comparison, spectra generated for simulations using the Mann method show similar resolved turbulence at all heights. These results indicate that using a stochastic method based on observations, such as the Veers or Mann method, improves the turbulence in the simulation results. This finding suggests that use of inflow turbulence at the boundary generated from observational data with a stochastic method, such as the Veers or Mann method, may yield improved simulations. In addition, increasing of update frequency of turbulence at the boundary also yielded improved simulations.

6.6 Turbulence Perturbations for Library Approach

An asynchronous offline coupling approach is investigated in order to provide turbulent inflow boundary conditions for a microscale simulation. We demonstrate our turbulent initiation approach through various simulations of neutral and convective boundary-layer setups. A short description of the model setup is provided, followed by results of simulations.

The Cloud Model 1 (CM1) is configured to be operated at large-eddy simulation (LES) scales to perform idealized simulations. Model resolution is constant, $\Delta x = \Delta y = 100$ m in the horizontal and stretched grid resolution, $\Delta z = 7.5$ to ~ 25 m is employed in the vertical. The domain size is 38.4 x 9.6 x 2 km^3, with a large extent in the x-direction. Dry flow configurations are integrated with a time step of 1 second. Revised MM5 Monin-Obukhov surface-layer scheme and thermal diffusion schemes are enabled. Random perturbations are added on the mean temperature field to help with turbulence initiation. Deardorff's tke scheme is used to compute the SGS eddy viscosity and eddy diffusivity for turbulent mixing.

6.6.1 Neutral boundary-layer simulations

Figure 6.23 shows the neutral, vertically uniform sounding that is used to initialize the simulations. The sounding is obtained at the SWiFT site in Lubbock, Texas at 00:00 to 01:00 UTC (7–8 p.m. CDT) on August 17, 2012.

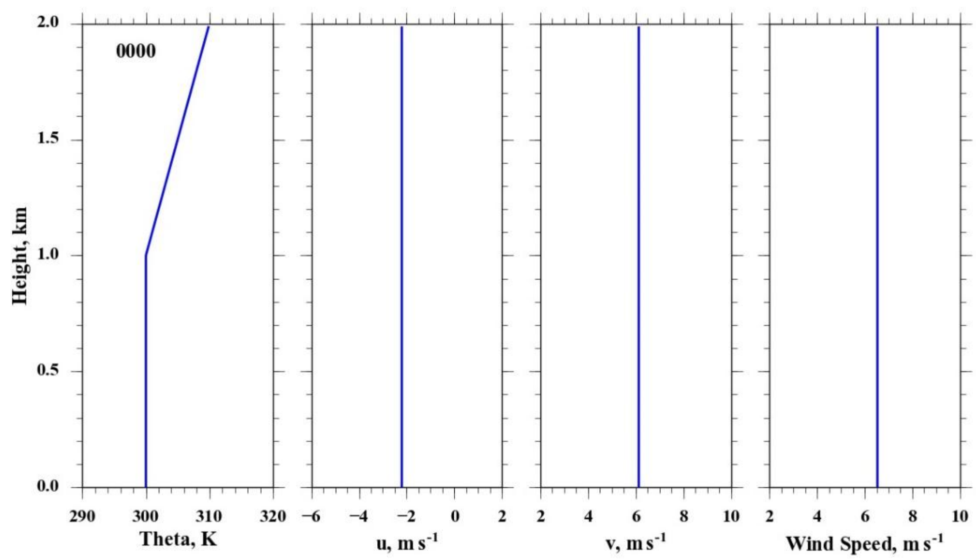

Figure 6.23. Vertical profiles of potential temperature and wind speed from an ideal dry neutral boundary layer at model initialization. The sounding data are collected at the SWiFT site at 00:00 to 01:00 UTC (7:00–8:00 P.M. CDT) on August 17, 2012.

As a preliminary exercise of turbulence triggering, we performed simulations by adding random perturbations on perturbation potential temperature (theta) and vertical velocity fields at the lateral flow boundary. Figure 6.24 shows vertical velocity profiles at 2 h into the simulation based on a simulation with U = 5 m/s wind profile. In this case, random perturbations are applied along 24 grid points in the x-axis for the entire y-domain within 1 km of the boundary layer. The field evolution closely resembles that of a periodic boundary simulation (not shown).

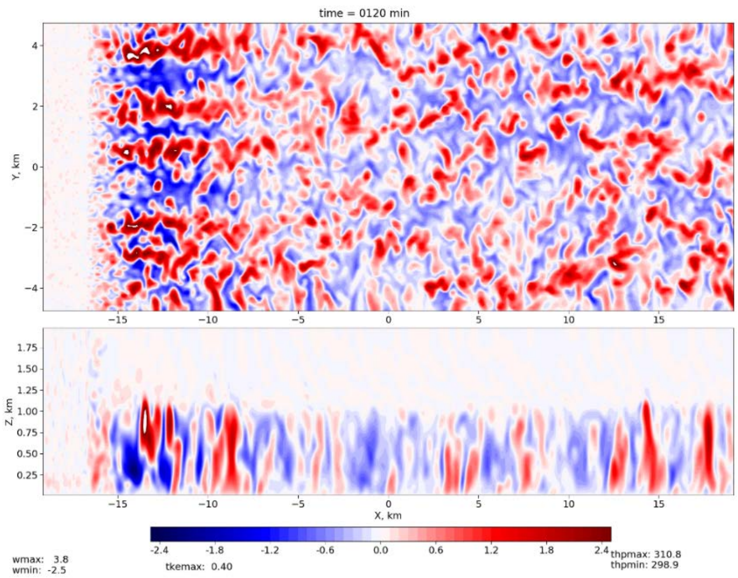

Figure 6.24. Vertical velocity profiles from a neutral boundary-layer simulation with random perturbations applied for 24 slices through the x-axis shown at 2 h. The top panel shows horizontal cross-sections at 500 m; the bottom panel shows vertical cross-sections at y=0. A constant heat flux profile is specified at the bottom boundary, and perturbation is applied on θ within [-1, 1] K and w – [-0.1, 0.1] m/s.

An important factor for turbulence generation are the heterogeneities imposed by surface heat flux, enabled in the previous simulation. Results using the same numerical setup, but without surface heat fluxes, show much weakened velocity profiles and laminar flow evolution near the southern boundary in Figure 6.25. Note that in this case, the vertical velocity scale is shown within [-0.5, 0.5] m/s range. Comparison with a periodic boundary simulation setup (Figure 6.26) shows qualitative similarities within the domain center. The domain size in the x-direction is halved in the periodic boundary simulation, thus updraft/downdraft features look elongated in Figure 6.26.

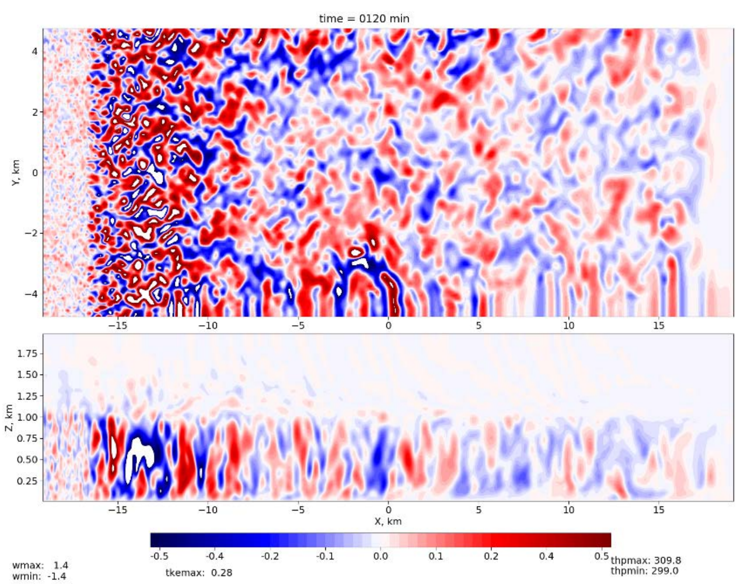

Figure 6.25. Same as the previous figure, but heat flux is disabled. Notice the vertical velocity scale shrinks to [-0.5, 0.5] ms^{-1} range compared to previous [-2.5, 2.5] ms^{-1} scale.

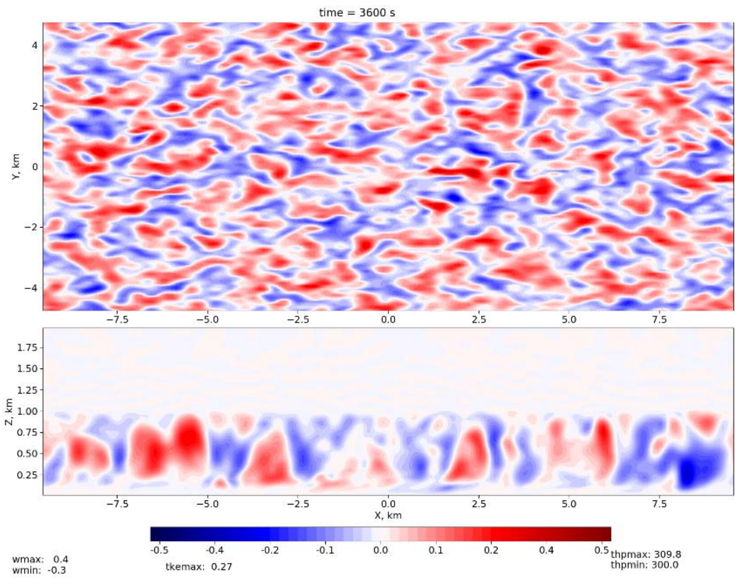

Figure 6.26. Vertical velocity profiles from periodic boundary simulations (initial theta = 300 K, U = 5 ms^{-1}). Top panels show horizontal cross-sections at 500 m; the bottom panel shows vertical cross-sections at y=0 at 1h. Notice that in this case, the x-domain extent is reduced to 19.2 km.

A comparison of random perturbation and offline coupling-based evolution of vertical velocity fields is shown in Figure 6.27 and Figure 6.28. The former approach shows stronger velocity magnitudes as the perturbation amplitude is 100 times larger compared to the latter method. Based on same perturbation magnitudes, as shown in Figure 6.29, the velocity fields have more coherent structures in the offline coupling simulation.

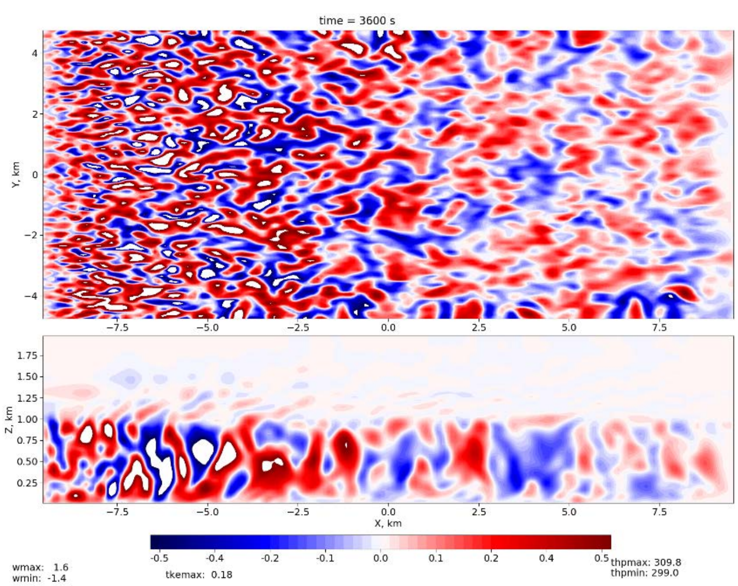

Figure 6.27. Vertical velocity profiles from neutral boundary-layer simulations with random perturbations applied through the first slice of x-domain shown at 1 h. No heat flux is specified at the bottom boundary, and perturbation is applied on θ within [-1, 1] K and w within [-0.1, 0.1] ms^{-1}.

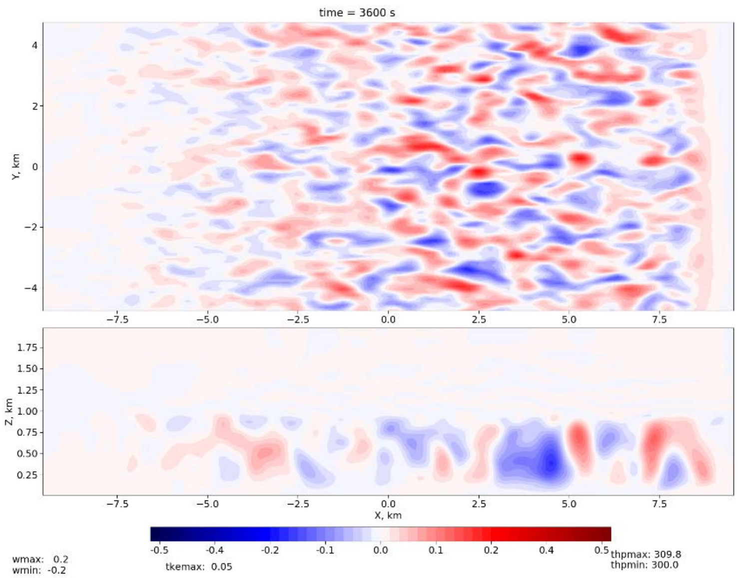

Figure 6.28. Vertical velocity profiles based on offline perturbations that are applied to θ [-0.01, 0.01] K; w [-0.001, 0.001] ms^{-1} through the first slice of x-domain.

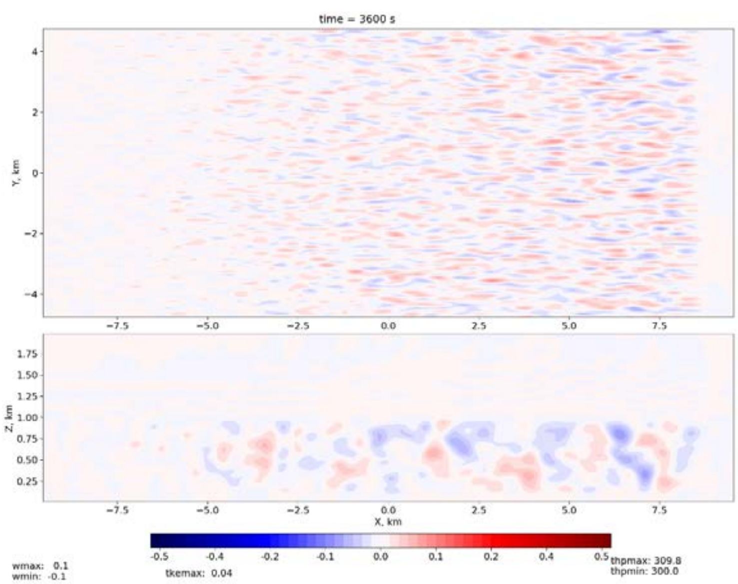

Figure 6.29. Vertical velocity profiles with random perturbations: θ [-0.01, 0.01] K; w [-0.001, 0.001] ms^{-1}. The perturbation magnitudes match with the offline coupling case.

We compared potential temperature perturbation magnitudes for each method in Figure 6.30. The perturbations are applied on the first slice of the x-domain for the entire y-extent within 1 km of the vertical domain. The top panels of Figure 6.30 show perturbation magnitudes that are used for Figure 6.27 and Figure 6.28. The surface-layer perturbation values (on 96 grid points) are stacked for a 1 h period. Magnitude scales are [-1, 1] K and [-0.01, 0.01] K for each corresponding approach. The first approach shows noisy random characteristics as the numbers are sampled randomly from a uniform distribution for each grid point. In the case of offline coupling, perturbations are extracted from a periodic boundary simulation that was already spun up for an hour. When presented via histogram plots, uniform and Gaussian distribution of random perturbation magnitudes become more visible.

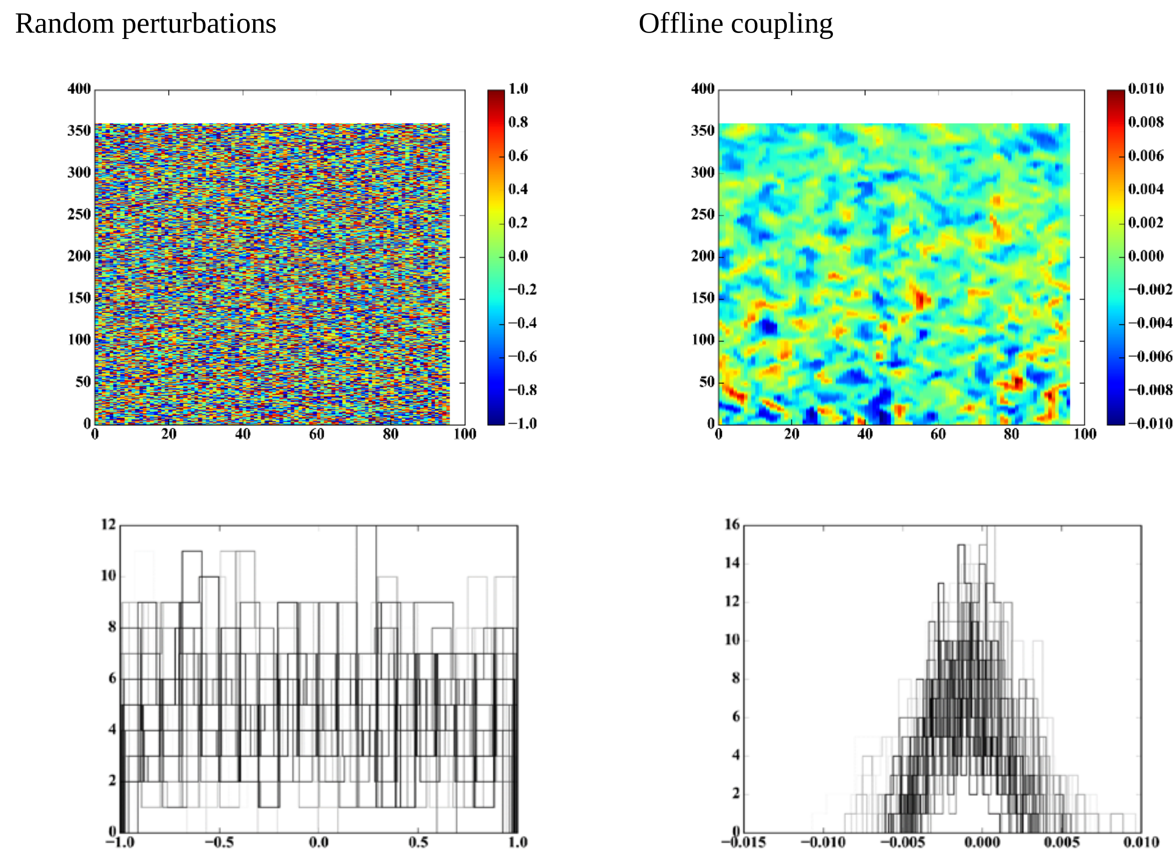

Figure 6.30. (Top panels) Magnitudes of potential temperature in each method, which are stacked temporally at 10 s for each perturbation slice. (Bottom panels) Histogram representation of magnitudes for each method.

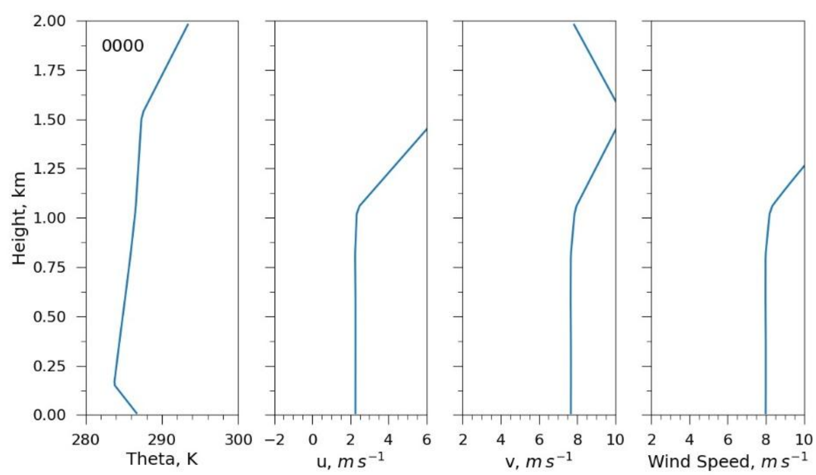

Figure 6.31. Vertical profiles of potential temperature and wind speed at the model initialization based on the sounding from the GFS data for the SWiFT site (averaged between 2013-11-08_20Z - 2013-11-08_22Z).

6.6.2 Convective Boundary-layer Simulations

In this section, results of ideal convective boundary-layer simulations are discussed. Figure 6.32 shows the convective sounding, which is output from the GFS model for the SWiFT site (averaged for the period of 20 to 22 Z on November 8, 2013). The sounding is unstable within the first 125 m, and wind speeds are nearly constant with heights up to 1 km of the domain.

The periodic boundary condition case has well-developed vertical velocity features within -5 to 5 ms^{-1} range (Figure 6.33). For the ease of model setup, we employed the same theta profile, yet used a constant U=5 m/s sounding as in the neutral case simulations. Single slices of data are saved from the periodic boundary simulations every tenth step, i.e., 96 x 40 x 4 bytes = 0.015 MB. A total of 360 slices, which covers a single simulation hour, requires about 5.5 MB for the theta perturbation at 100 m horizontal grid spacing.

A snapshot of the vertical velocity fields from an open boundary simulation at 2 h is shown in Figure 6.34. Compared to the neutral case, laminar features transition to turbulent eddies much faster. In the case of the neutral boundary, laminar streaks occupy the entire domain (not shown). This difference could be attributed to the convectively unstable nature of the sounding, as well as heat flux input.

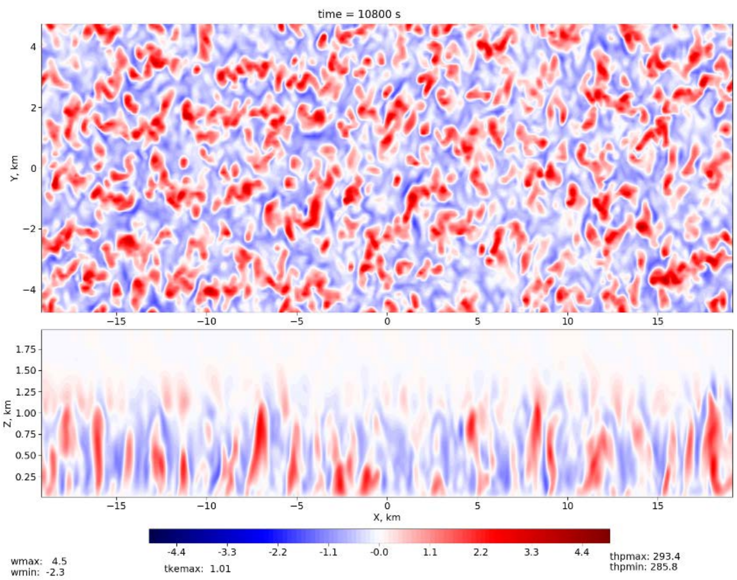

Figure 6.32. Vertical velocity profiles from periodic boundary convective boundary-layer simulation at 3 h.

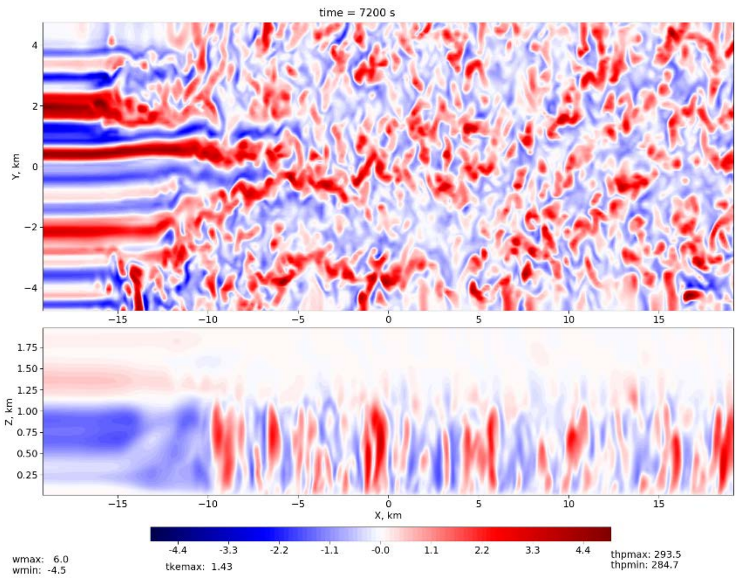

Figure 6.33. Vertical velocity profiles from open boundary convective boundary-layer simulations at 2 h.

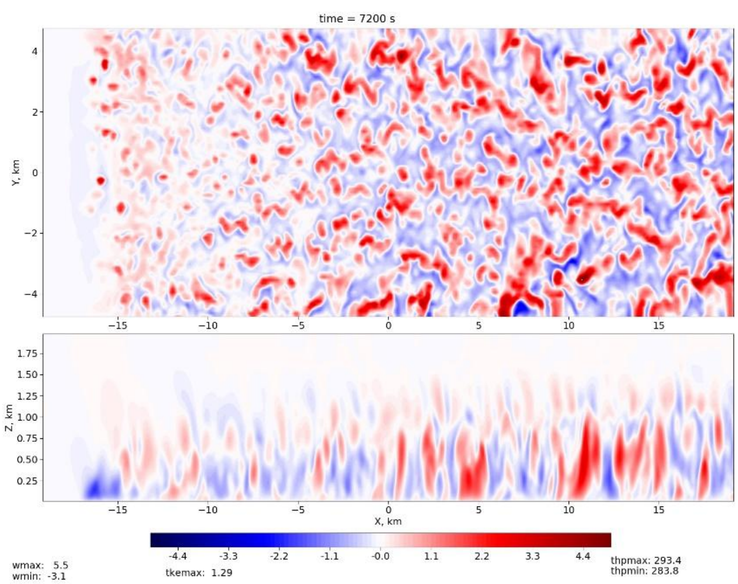

Figure 6.34. Vertical velocity profiles from offline coupled, open boundary, convective boundary-layer simulations at 2 h.

Potential temperature perturbation fields are applied through incoming flow boundaries; thus, a more realistic flow development is established. Much smaller magnitude perturbations are sufficient to trigger turbulence as convective instabilities and surface heat fluxes provide natural flow heterogeneity.

6.6.3 Conclusions

These results test the applicability of offline perturbation methods for neutral and convective boundary-layer simulations. When simulations are run with open boundary conditions, flow cannot recycle within the domain; thus, turbulent eddies cannot develop quickly. This problem is partially alleviated by applying perturbations to the incoming flow direction that are extracted from periodic boundary-evolved simulations. Work is in progress to extend the workflow to capture flow evolution in 2D and for MPI parallel domain setups. Performing longer simulations (over 10 h) is also intended to better capture flow development and assess the method for variations in lateral boundaries. With the introduction of proper nudging/scaling while adding perturbations, it is expected that turbulent eddies will be more quickly developed compared to the current approach.

6.7 Development of a Generalized Boundary Condition with Velocity Perturbations

6.7.1 Motivation

Robust offline mesoscale-to-microscale coupling (MMC) imposed through the boundary conditions of the microscale domain requires a mechanism for both promoting the development of realistic turbulence and sustaining the developed turbulence scales. One way to accomplish this is by enriching the velocity spectra of the mesoscale inflow using a synthetic turbulence model (Quon et al, 2018). This entails extracting the fluctuating part of the modeled turbulence field and superimposing these perturbations onto the laminar inflow from the mesoscale. The microscale model used to demonstrate this strategy is the Simulator fOr Wind Farm Applications (SOWFA).

The original workflow for superimposing perturbations onto WRF inflow was to extract the boundary data for SOWFA using an auxiliary FORTRAN code. A Python library was then used to read in both the boundary data and a pre-calculated TurbSim field, manipulate the TurbSim field, and then write out new boundary data with the TurbSim fluctuations added. In this approach, all of the perturbed inflow data are generated and written to disk at once. While this approach produces the desired results, it very quickly becomes intractable for larger problems with WRF-derived inflow on multiple SOWFA boundaries. Depending on the coupling frequency, the intervals at which a WRF boundary snapshot is provided, the generated MMC inflow data may amount to 100 s of Gb or more. This unnecessary data I/O makes data processing and archiving exceptionally onerous.

The ability to directly read in TurbSim synthetic turbulence data for superposition onto WRF-derived inflow data will greatly facilitate the MMC research in upcoming years. Applying perturbations on the fly–instead of precomputing and loading data from disk--can significantly increase computational efficiency and reduce engineering hours. Moreover, integrating the inflow data processing directly into the microscale code allows for perturbation parameters (such as the variance of the components of the velocity field, length scales, or the perturbed boundary-layer height) to be automatically calculated and updated instead of assumed constant. This advances our MMC capabilities toward a readily deployable production code for use by industry.

6.7.2 Approach

A mixed inflow-outflow boundary condition (BC) has been recently developed (for further discussion, see Section 8.2). This BC enables simulation of conditions for which an inflow boundary can have both inflow and outflow regions (e.g., inflow with a significant amount of veer). Moreover, the inflow and outflow can change arbitrarily over time, which permits simulation of large wind direction changes (e.g., a frontal passage event). Our current work further generalizes the mixed inflow-outflow BC to allow velocity perturbations to be added in a straightforward manner with minimal additional user input.

At the moment, only the TurbSim synthetic turbulence model is supported, and an auxiliary TurbSim simulation is still needed to produce a binary TurbSim full-field file. Additional synthetic turbulence models may be added in the future. At the beginning of each simulation, each processor will read the TurbSim field into memory; at each time step, the BC will map the current simulation time to an equivalent TurbSim simulation time accounting for periodicity. The instantaneous fluctuating velocity field is then interpolated, scaled, and added to the WRF inflow data. These perturbed inflow data are only applied if the calculated mass flux on the boundary indicates an inflow condition.

Prior to the velocity perturbations being added to the WRF inflow, the perturbations are scaled to introduce height dependency. The scaling depends on the perturbed layer height, which at this time must either be constant or tabulated (based on WRF output or field observations). The profile to which the perturbations are scaled can either be: constant up to the perturbed layer height; nearly constant up to approximately the perturbed layer height, as described by a sigmoid (hyperbolic tangent) function; or, linearly increasing up to the perturbed layer height. Currently, the turbulent kinetic energy (or turbulence intensity) is not adjusted over time. But in the future, output from the WRF planetary boundary-layer scheme may be utilized.

6.7.3 Demonstration Case

A near-neutral period within the diurnal cycle observed at the SWiFT facility on November 8, 2013 was selected as a demonstration case of the mixed inflow-outflow BC with perturbations (see Section 2.2). A near-neutral period between 21:00 and 00:00 UTC is of interest. During this time, a nocturnal transition is occurring, during which the atmospheric boundary-layer transitions from convective daytime conditions to stable nighttime conditions. An additional three hours prior to this period was simulated to allow for the turbulence field to fully spin up. Excellent agreement was observed between WRF and the field data in terms of wind speed and direction, as well as the time of the down-ramp prior to the nocturnal transition. The WRF velocity and temperature fields are used to drive the SOWFA microscale simulation. Enrichment of the velocity spectra was performed using TurbSim with hyperbolic tangent function scaling with height; the boundary layer was seen to increase in height from 560 m at the beginning of the spin-up period, up to 885 m during the period of interest; the perturbed layer height was updated over time to match this variation. Within TurbSim, the IEC Kaimal turbulence model was used to generate synthetic turbulence with the default IEC parameters for the turbulence length scale and coherence modeling.

Preliminary results appear in Figure 6.35 and Figure 6.36, which show a horizontal slice through the flow field at a nominal hub height of 80 m above ground level. Figure 6.35 shows the flow field at the beginning of the period of interest at 21:00 UTC, and Figure 6.36 shows the end of the period of interest at 00:00 UTC on the following day. At 21:00 UTC, the atmosphere remains slightly unstable, which facilitates the development of some turbulence features—even without perturbations—following a lengthy fetch region. However, by 00:00 UTC, the turbulence structures that had developed in the control case have vanished. These figures clearly indicate that velocity perturbations are needed to develop a realistic turbulence field; otherwise, the turbulence will decay over time. While the TurbSim-enriched fields are able to develop and maintain a level of turbulence intensity, the development of that turbulence still takes a significant amount of time, and the three-hour spin-up period may be insufficient in this case. In addition, the TurbSim synthetic turbulence may be optimized in terms of correlations and simulated length scales in order to more closely approximate the actual inflow field, if such data are available.

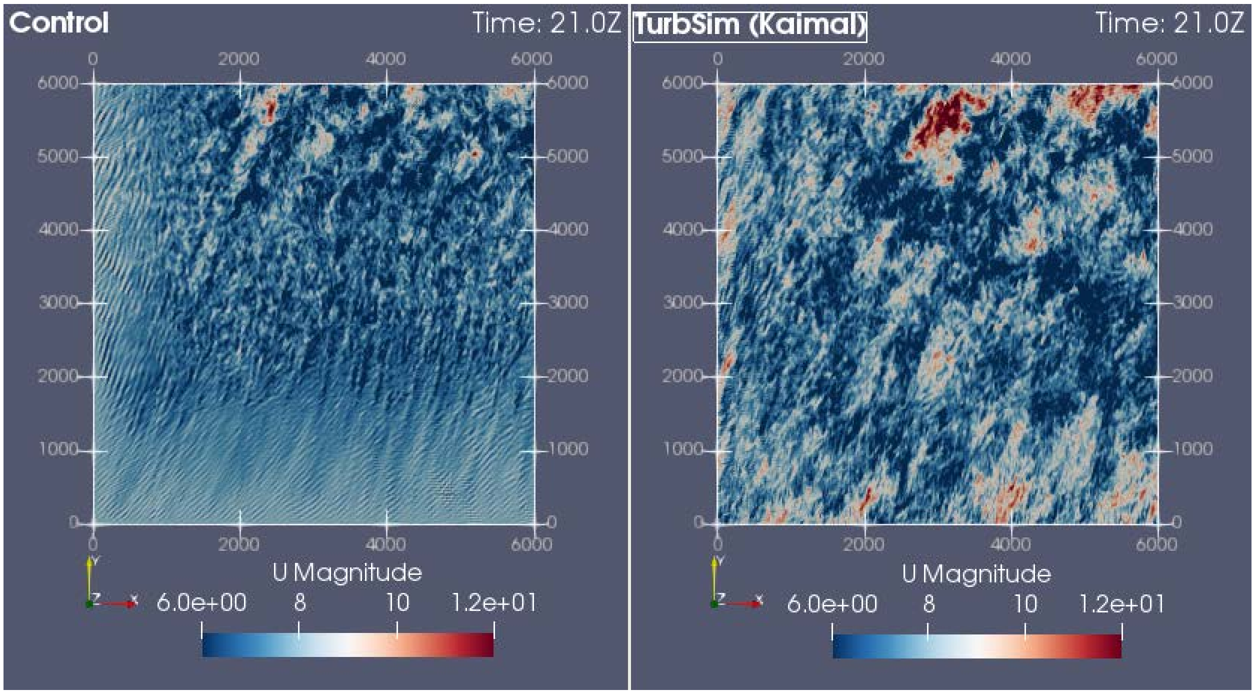

Figure 6.35. Velocity fields on a horizontal plane at the beginning of the period of interest, without (left) and with (right) TurbSim perturbations applied.

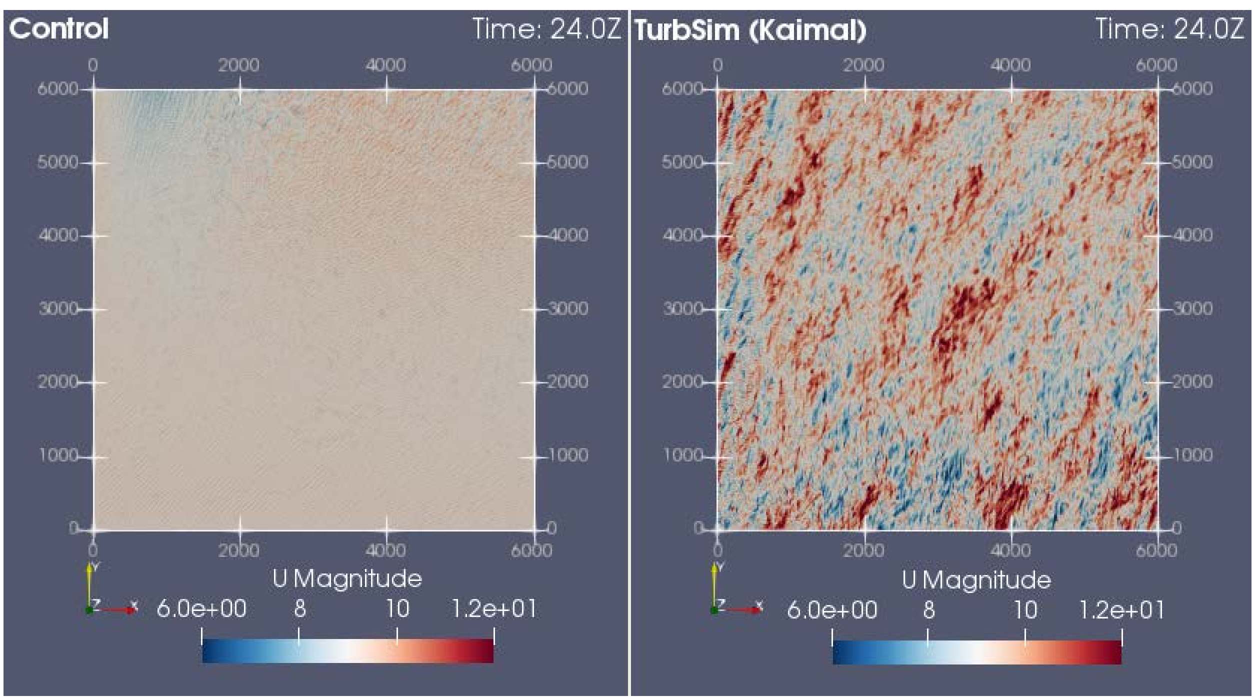

Figure 6.36. Velocity fields on a horizontal plane at the end of the period of interest, without (left) and with (right) TurbSim perturbations applied.

6.8 Formal Assessment of Perturbations Cases

As noted previously in Section 3.2, the assessment of different approaches to generating turbulence at the microscale is proceeding. As simulation data from the November 8 and 9, 2013 case is shared with NCAR's evaluation team, the outlined evaluation method will be implemented. The goal is to provide a rigorous comparative assessment of the full variety of techniques being considered.

7.0 Improvements in Near-Surface Physics

7.1 Analysis of WRF-LES Simulations With Spatially Varying and Homogeneous Surface Fluxes

In its current configuration, Nalu does not include a surface energy budget model to represent the surface sensible, latent, and momentum fluxes. This shortcoming precludes Nalu from estimating time varying fluxes that are consistent with the flow. The WRF model run in large-eddy simulation (LES) mode includes a land surface model (LSM) that explicitly calculates the surface fluxes. The WRF-LES output could be used as a bottom boundary condition to Nalu at the spatial resolution of the LES, with the complication that the LES output must be interpolated to the Nalu mesh. A simpler alternative approach is to provide spatially homogenous but temporally varying surface fluxes to the microscale model. This simple approach, however, might have an impact on the simulated turbulence.

As a proof of concept, two sets of simulations have been completed using WRF-LES nested inside a mesoscale WRF domain located near the Department of Energy Scaled Wind Farm Technology (SWiFT) facility. The first simulation applies the interactive WRF LSM to provide temporally and spatially varying surface fluxes. The second simulation uses surface fluxes that are averaged over the domain for that time step. This approach assures that the energy input is the same in both simulations.

There are differences in the instantaneous wind speed and vertical velocity at 80 m above ground in the two simulations (Figure 7.1). Clearly, the differences in the surface fluxes are expected (top row of Figure 7.1). There are also differences in both the vertical velocity (as large as ±4 ms^{-1}) and horizontal wind speed (also as large as ±4 ms^{-1}). Do these differences, however, impact the properties of the turbulence within the model domain?

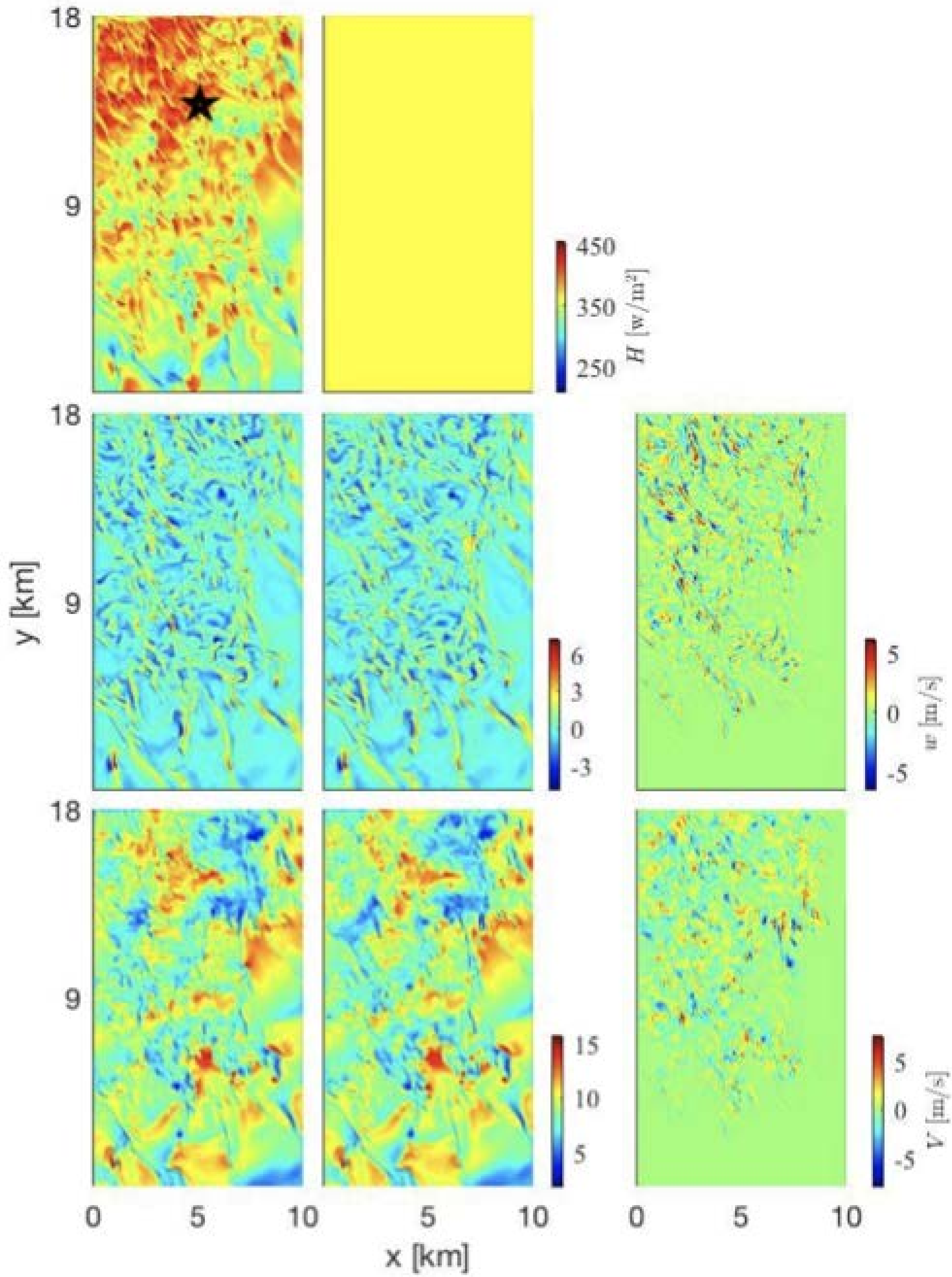

Figure 7.1. Instantaneous heat fluxes (top row), vertical velocity (middle row), and wind speed (bottom row) with spatially varying fluxes (left column), homogeneous surface fluxes (middle column), and difference in the two sets of simulations (right column). The star indicates the location of time series and profiles presented in Figure 7.2 and Figure 7.3.

Profiles of u, v, and w variance, and tke have been derived from the WRF-LES output for the location marked with a star in the northern part of the domain shown in Figure 7.1. The variance profiles are similar regardless of the method used to apply the surface fluxes (Figure 7.2). There are slightly larger differences in the w variance above an altitude of 750 m, but very little difference at hub height. Spectra have been computed from the time series of u, v, and w for the same location and are shown in Figure 7.3.

In this case the spectra are computed from three different 30-minute periods to smooth the results. Similar to the findings for variance and tke, the differences in the turbulence spectra are quite small and are not likely to be significant.

The results presented here show that while there are differences in the instantaneous flow field (Figure 7.1) the differences in the turbulence statistics (variances, tke, and spectra) are small. These results suggest that it could be sufficient to drive Nalu with a spatially averaged, but time varying, value of surface fluxes for wind-energy applications. There are two important caveats associated with this analysis. First, the result shown is for strongly convective conditions, and the findings could be different if different stabilities were considered. Second, this study is limited to the simple terrain and land use in the vicinity of the SWiFT site. Additional simulations are being conducted for a location within the WFIP 2 domain to determine if results are similar in an area with more complex terrain and land use/land cover.

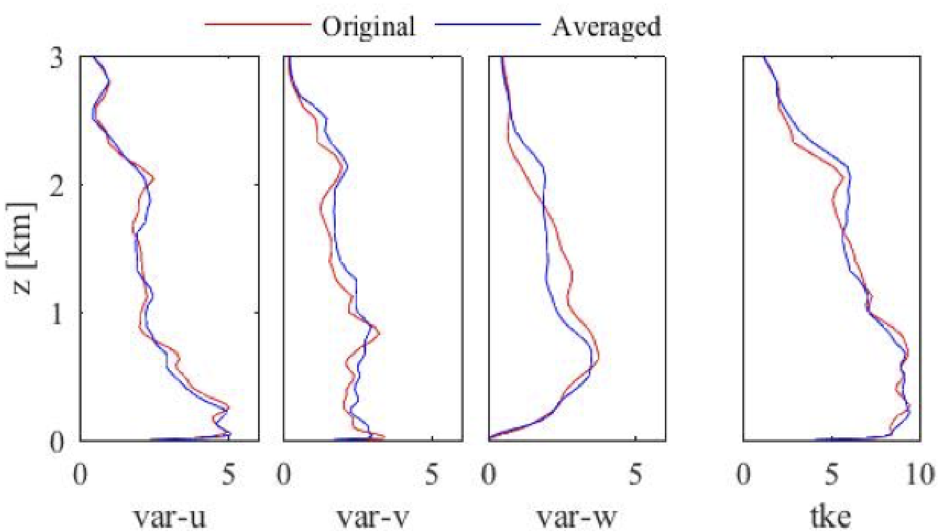

Figure 7.2. Profiles of u, v, and w variance and tke computed from simulations with spatially varying (red) and averaged (blue) surface fluxes. Results are averaged over a one-hour period for the location shown in Figure 7.1.

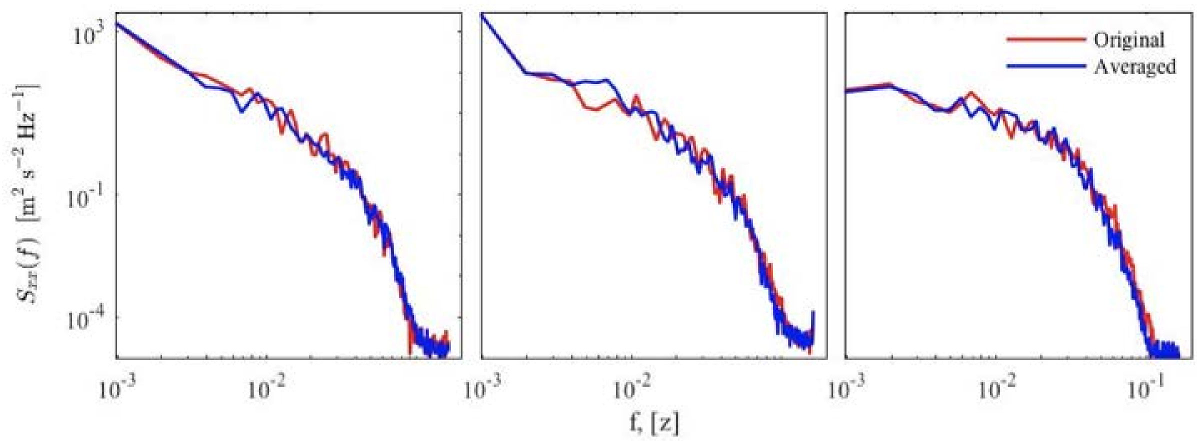

Figure 7.3. Spectra of u, v, and w computed from simulations with spatially varying (red) and averaged (blue) surface fluxes. Results are averaged over three separate 30-minute periods for the location shown in Figure 7.1.

7.2 Use of a Distributed Drag Model to Improve Near-surface Flow Physics in LES

A commonly reported shortcoming of the standard implementation of the Monin-Obukhov Similarity Theory (MOST) to parameterize surface energy exchange in LES is its inability to accurately capture the expected law of the wall behavior, the logarithmic increase of mean wind speed above the surface (e.g., the “log-law”) within the surface layer, the lowest approximately 10% of the atmospheric boundary layer (ABL). Errors in the shear surface region propagate throughout the ABL depth, and therefore impact ABL dynamics, including wind speed and turbulence characteristics, which, in turn, impact wind-plant performance.

Potential sources of error attributable to the standard MOST implementation into atmospheric LES include application to conditions that do not satisfy the assumptions of homogeneity and steadiness on which the theory is based. Also, application of the MOST relationships individually to each grid cell adjacent to the surface within the LES domain and their local velocities, which posits a mismatch between the theory that applies to the mean velocity only. These factors—along with other sources of error in LES, including the sub-filter scale (SFS) parameterizations, numerical solution procedures, and inexact forcing—combine to reduce the fidelity of the simulated flow field.

Previous attempts to improve the fidelity of near-surface flow characteristics include more sophisticated LES SFS models, and the use of damping functions near the surface. Despite the utility of these approaches to particular problems, no robust framework for improved surface-layer flow simulation under general conditions has yet been developed.

One approach that has enjoyed widespread adoption to improve the near-surface flow field over vegetated canopies and forests is the explicit plant canopy parameterization. Explicit plant canopy parameterizations move beyond simply modifying the surface fluxes and also utilize drag terms that directly impact the momentum equations within the plant canopy, as required to capture the nonmonotonic increase of mean wind speed observed in vegetated canopies. Other physical processes that may also be modified within the canopy (including SFS tke, radiative transfer, and scalar exchange) can be incorporated in more sophisticated models for applications requiring higher fidelity representations of those processes (see review by Patton and Finnigan 2012).

For wind-energy applications, concepts from the explicit plant canopy parameterization were adapted to target improvement of the mean wind speed distribution over smooth terrain with high aerodynamic roughness, an application where the WRF model, for example, has been shown to produce significant departures from the expected logarithmic behavior. This new approach, developed during the latter stages of FY17 and FY18, and referred to here as the "pseudo-canopy model" (PCM), also applies drag terms to the momentum equations over a specified depth. However, here the drag terms do not represent a plant canopy, but rather represent a distribution of the surface aerodynamic drag value, obtained from MOST, as a decreasing function of height. The idea to distribute the surface drag value vertically, rather than using it to provide a surface stress (as is common) is motivated by recognition that multiple sources of error (e.g., the model numerical discretization and the SFS stress parameterizations) impact the modeling of stresses near the surface, and relying on the divergence of those stresses to produce the near-surface wind speed distribution is likely to lead to errors. Applying the MOST-derived surface value as a distributed drag influences the flow speed directly, augmenting the accelerations arising from the divergence of the stresses, leading to improved flow characteristics.

Figure 7.4 shows vertical distributions of wind speed from a simulation of geostrophically-forced flow over a flat, rough surface with a small, uniform roughness value (see Arthur et al 2018 for details). The mean wind speed resulting from a simulation using the standard MOST implementation is shown by the solid black line. The dashed black line shows the expected logarithmic distribution based on the surface friction velocity value corresponding to the solid black line, showing the failure of the WRF simulation using the standard MOST implementation (with the drag coefficient expressed as a surface stress) to produce a wind speed that is consistent with the MOST surface boundary condition. The colored lines in Figure 7.4 show the mean wind speed distributions resulting from use of the PCM using three different shape functions for the vertical distribution of the surface drag. The dashed lines of the same color show the expected logarithmic distributions using the surface friction velocity values obtained from each of the simulations. The heights in the legend indicate the distance above the surface over which each shape function produced the lowest root mean square departure from its expected distribution (difference between the solid and dashed lines of each color). While Figure 7.4 shows significant improvement over the standard MOST implementation in one particular configuration, Arthur et al (2018) shows that the method is robust over different mesh spacings, grid aspect ratios, and surface roughness values, while also increasing the magnitude of resolved stress and tke, other flow parameters that tend to be underestimated using the standard MOST approach. The MMC team will continue exploring application of the PCM to improve near-surface and ABL flow simulations in more complicated settings during FY19.

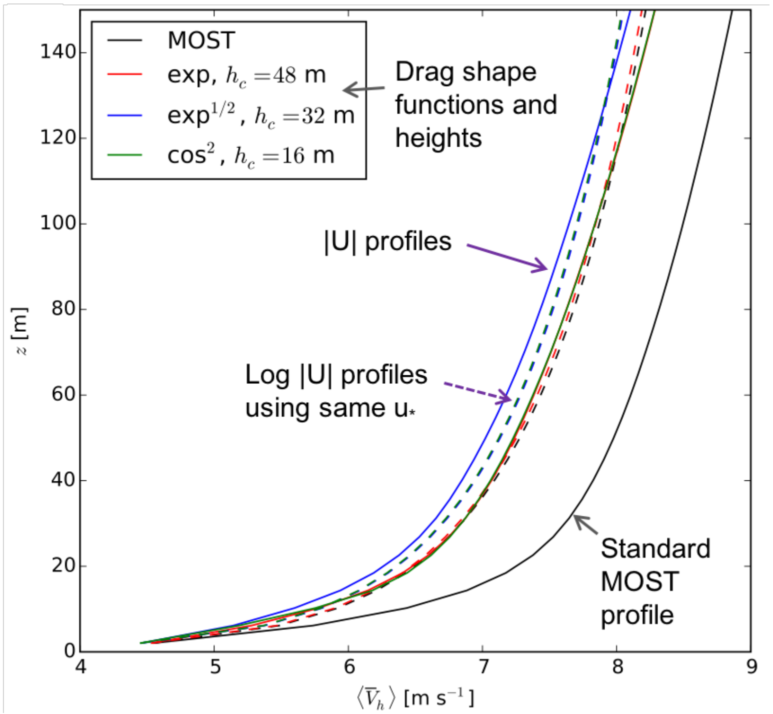

Figure 7.4. Mean vertical wind speed distributions from WRF simulations using both the standard MOST surface boundary condition and three different PCM approaches, as described in the text.

8.0 Evaluation of Coupling Techniques

In this chapter, we present the application of distinct coupling techniques to benchmark cases for the evaluation of their performance. Each of these techniques is different from one another, but all are valuable techniques. We have found that depending on the situation, different techniques are needed, so there is no single technique that fulfills all needs.

We begin in Section 8.1 by showing a coupling technique that is based on the periodic precursor method typically used to produce a canonical, horizontally homogeneous atmospheric boundary layer, but that extends it to accept mesoscale information such that it produces non-canonical results. This technique avoids the use of inflow perturbations because turbulence develops in time rather than space. Here it is used to simulate the non-canonical November 8, 2013 SWiFT diurnal cycle, but the method can also be used to generate turbulence to be added to heterogeneous WRF inflow for general cases. In Section 8.2 we show an application of a more general coupling technique using mesoscale WRF data as boundary conditions to a separate CFD simulation using SOWFA applied to the November 21, 2016 WFIP 2 case in complex terrain. Although final results are not presented, we present the challenges faced in performing this type of simulation and the possible solutions. Last, in Section 8.3, we show an application of the same sort of more general coupling technique fully within the WRF framework. The case studied is the November 15, 2016 WFIP 2 case in complex terrain.

It is important to note that in this year, when we couple WRF to a separate microscale solver, that microscale solver has been SOWFA, but all knowledge learned is directly applicable to the coupling of WRF to Nalu, which will begin to occur in FY19.

8.1 An Application of the Internal Forcing Coupling Technique: SWiFT, November 8, 2013

A detailed investigation was performed on the effect of internal forcing coupling techniques on the statistics of resolved turbulence in the microscale simulation. These coupling techniques apply mesoscale forcing internally within the microscale domain through time- and height-dependent source terms in the momentum and temperature equations. The microscale domain thereby uses periodic lateral boundary conditions so as to allow turbulent structures to be recycled at the domain boundaries, causing turbulence to spin up in time rather than in space. When the wind site of interest involves heterogeneous terrain conditions, the internal forcing techniques can still be used in a precursor domain to generate realistic three-dimensional turbulent structures that can be fed into the main simulation domain, a valuable alternative to inflow perturbation strategies.

There are two ways to determine the mesoscale tendency forcing terms:

- The first and most natural way is to extract the corresponding tendencies from the mesoscale simulation as a function of time and height and simply apply those directly to the governing equations (Sanz Rodrigo et al., 2017).
- In the second method, which is akin to data assimilation, the mesoscale model time-height history of mean wind velocity and potential temperature is used by the microscale solver to compute adequate source terms that cause the microscale simulation planar-averaged profiles to match the time-height history in the mesoscale simulation, while still resolving all the turbulence that results from those planar-averaged conditions.

The first approach based on mesoscale tendencies has proved to be a valuable coupling technique. However, the tendencies derived from the mesoscale simulation might contain small-scale turbulent fluctuations that have to be averaged out in order to avoid double counting, and the choice of averaging parameters requires modeling experience and affects the microscale solution. The second approach based on mesoscale wind and temperature profiles removes the need for averaging. Moreover, this approach can easily be used with observational data from met masts or scanning LiDARs, while the tendency approach would require measurements of pressure gradients and large-scale advection of momentum and temperature, which are seldom available from observations.

The performance of the internal forcing coupling techniques described above is evaluated based on the SWiFT site November 8, 2013 case, which represents a typical example of a diurnal cycle. Two microscale simulations are performed with SOWFA using the two different forcing techniques, and both cases are driven by the same mesoscale data set generated with WRF.

The WRF data set was generated in FY16, and the model setup is described in Section 2.3.1 of the MMC Year 2 report (Haupt et al. 2017). In summary, the WRF simulation used three nested domains centered at the SWiFT site with 27 km, 9 km, and 3 km grid spacing, and the smallest domain had a size of 354 km x 300 km. In the vertical, 88 model levels were used with a minimum resolution of approximately 5 m in the lowest 20 m of the domain. The time step was set to 15 s, and model output was saved every 5 min.

The SOWFA microscale simulations used a numerical domain of 5 km x 5 km x 2 km with uniform grid spacing of 10 m and lateral periodic boundary conditions. The effect of subgrid-scale (SGS) motions on the resolved flow is modeled using the one-equation Lilly SGS model. Both simulations were initiated at 12:00 UTC, which corresponds to 6:00 AM local time. The time step is set to 0.5 s, and the simulations cover a period of 24 h. The first SOWFA simulation incorporates mesoscale tendencies that account for the pressure-gradient force and large-scale advection of momentum and temperature, and the tendencies are computed along the WRF model column nearest the SWiFT tall tower. In the second simulation, the microscale solver computes source terms for the momentum and potential temperature budget equations that cause the solver to return the same time-height history of planar-averaged wind velocity and potential temperature as observed in the nearest WRF model column.

The time-height contours of horizontal wind speed as calculated by WRF-mesoscale and SOWFA are compared in Figure 8.1. The mesoscale results are obtained from the model column (3 km x 3 km cells) nearest the SWiFT site, and the microscale profiles have been averaged over horizontal planes spanning the entire microscale domain. It is shown that both coupling techniques are capable of capturing the primary trends in the mean wind speed. The mean values from the profile assimilation approach nearly exactly captures the WRF values because it is driven by these WRF data. Figure 8.2 shows the time histories of wind speed, wind direction, and potential temperature at 116.5 m. The numerical results obtained with WRF-mesoscale and SOWFA are compared with observations from the TTU tower. The SOWFA simulations driven by the profile assimilation technique follow the WRF-mesoscale input perfectly, while the tendency approach does yield some differences, especially in the mean wind speed and wind direction. Further, the wind speed and direction predicted by SOWFA agrees reasonably well with the observations. The prediction of temperature is good throughout the daytime, but during the evening transition the observed temperature drops off more rapidly. Overall, the agreement in terms of these mean quantities is good and seems to suggest that both coupling methods are viable options.

However, examining the turbulence intensity in Figure 8.3 shows that there is in fact a big difference between the two SOWFA simulations, especially during the daytime when the boundary layer is unstably stratified. A comparison with the TTU tower observations shows that the tendency approach predicts reasonable values of turbulent intensity, while the profile assimilation run greatly overpredicts turbulence levels.

It is currently unclear why the profile assimilation approach generates too much turbulence. This is an interesting discovery, because it has led us to consider the coupling of forcing between vertical levels along with how the forcing should deal with the large time lags in the atmospheric dynamical system. The profile assimilation coupling technique will be further investigated in FY19 to understand the higher turbulent intensities and to improve the coupling methodology.

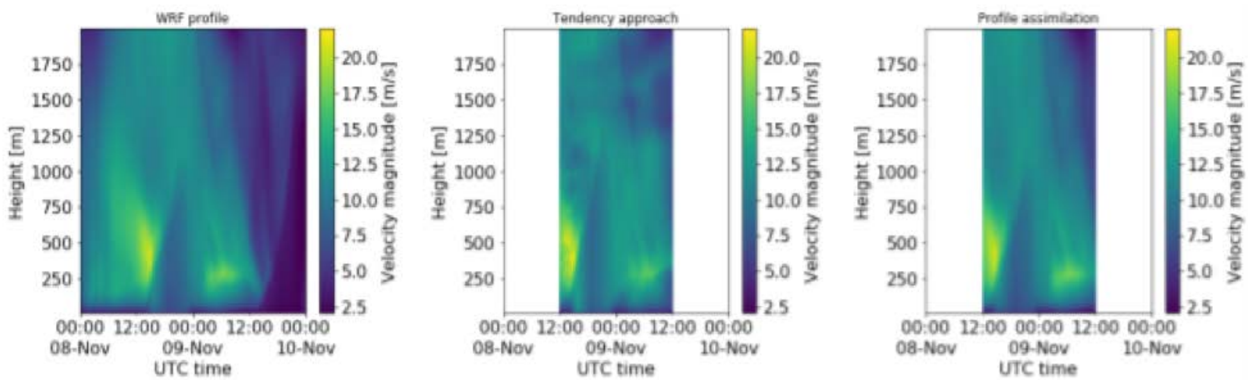

Figure 8.1. Time-height contours of horizontal wind speed of the November 8, 2013 SWiFT case from the WRF-mesoscale simulation (left), the planar-averaged wind speed from SOWFA using the tendency approach (middle), and the profile assimilation approach (right).

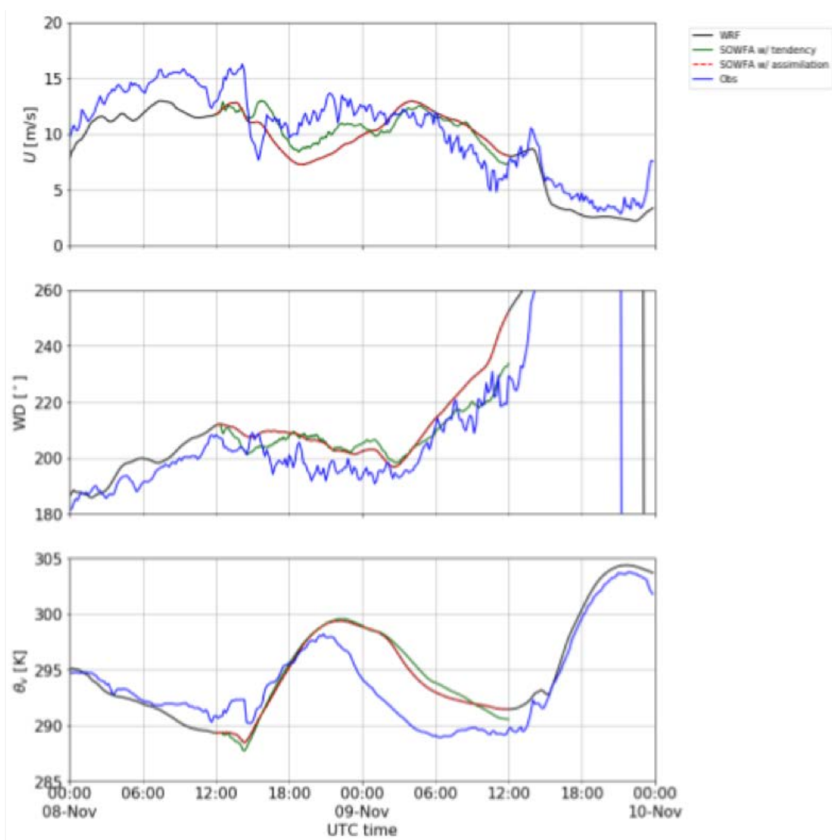

Figure 8.2. Time history of the horizontal wind speed (top), the wind direction (middle), and the potential temperature (bottom) at 116.5 m. Results obtained with WRF and SOWFA (both using the tendency approach and profile assimilation) are compared with observations from the TTU tower. The SOWFA results are planar-averaged.

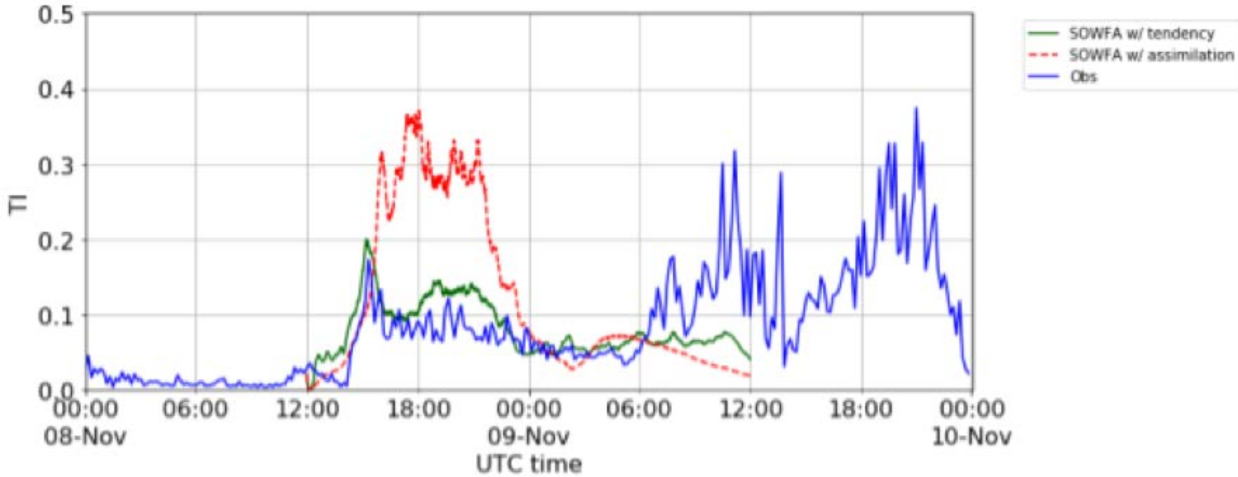

Figure 8.3. Time history of turbulence intensity (TI) at 116.5 m. Results obtained using SOWFA (both using the tendency approach and profile assimilation) are compared with observations from the TTU tower. The SOWFA results are planar-averaged.

8.2 An Application of the Boundary Forcing Technique with Separate Mesoscale and Microscale Solvers: WFIP 2, November 21, 2016

One goal of the MMC project is to be able to robustly couple mesoscale weather information, either from a numerical weather prediction code or observations, to a separate microscale code for simulating the wind-plant domain. This is in contrast to the WRF-mesoscale-microscale framework, which occurs all within a single code, as described in the next section. In this section, we describe work toward simulating the Biglow Canyon wind farm, which is within the WFIP 2 measurement region, using the SOWFA code given mesoscale information from WRF. The overarching goal is to simulate the full Biglow Canyon wind farm with actuator lines or disks, with high resolution around the rotors and wakes, capturing terrain features down to 30 m resolution, and using full mesoscale coupling. This is an excellent verification, validation, and uncertainty quantification case for MMC, because not only does it utilize all the meteorological data collected within the WFIP 2 campaign, but also the SCADA data from the turbines of the Biglow Canyon wind farm.

The microscale simulation domain is shown in Figure 8.4. It covers a 30 km x 30 km region surrounding the Biglow Canyon wind farm. The Columbia River, Deschutes River, and John Day River run through this domain. For visibility, only every other grid line is shown. The domain is 10 km tall, with coarsening resolution at higher heights, to minimize the effects of terrain blockage. The case studied here is November 21, 2016.

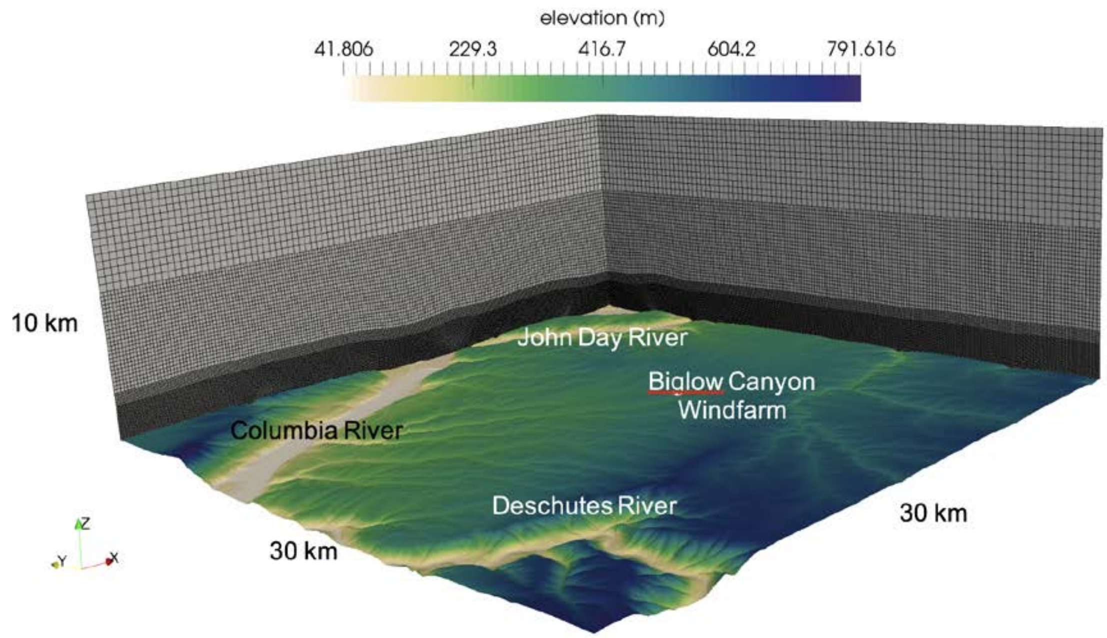

Figure 8.4. The microscale domain used in the WRF-SOWFA Biglow Canyon wind farm case study. The terrain is shown and colored by elevation. The outline of the mesh is also shown on the north and east domain boundaries (every other grid line is shown).

We extracted velocity, temperature, and surface sensible heat flux and skin temperature time series information from WRF on surfaces corresponding to the domain boundaries of the microscale domain shown in Figure 8.4. Those data then drive the microscale simulation. Flow is predominantly from the west, in this case, but there are mixes of inflow and outflow on the north and south boundaries of the microscale domain.

Four main issues have arisen in running this type of coupled simulation:

1. the mismatch in terrain resolution between the mesoscale and microscale simulations,
2. the need for terrain-generalized inflow perturbations,
3. the general condition of mixed inflow and outflow on a single boundary, and
4. spurious gravity waves generated at the regions of inflow.

One of the easier issues is issue 1, the terrain mismatch between the mesoscale and microscale. The mesoscale domain has 750 m terrain resolution, which is more resolved than typical for mesoscale simulations. The microscale has a 30-m terrain resolution, which can be on the coarse side. One can either designate a "coarsening fringe" around the outer edge of the microscale domain, in which the terrain resolution relaxes back to that of the mesoscale or map the WRF-extracted coarse resolution data (that is boundary data for the microscale simulation) to the fine resolution terrain.

Issue 2, the need for terrain-generalized inflow perturbations has not been studied in detail yet, but our current thinking is that we will simply take any one of the inflow perturbation strategies tested by the MMC group and make it terrain-following, which would be a simple extension. The other consideration is how to apply perturbations when the flow is very oblique to the inflow boundary, something that we have not yet worked out.

A more challenging issue is issue 3, the ability to have a mixed inflow and outflow boundary condition. We devised a SOWFA boundary condition that iterates over an entire microscale domain boundary, face by face (the domain boundary is discretized into thousands of small faces). For each face, the algorithm evaluates the velocity flux. If the flux is into the domain, then the time-series boundary surface data extracted from WRF are applied as a Dirichlet boundary condition (one in which the solution value is specified). If the flux is out of the domain, then a Neumann condition is set in which the boundary-normal gradient of the solution is set to zero. The zero-gradient condition on outflow does nothing to ensure that flux out of the domain will balance the flux into the domain. Therefore, a global flux balancing adjustment is applied by comparing the total velocity flux in to the total velocity flux out. The flux out is scaled to correct any mismatch, but rather than explicitly applying this correction, the boundary-normal pressure gradient is adjusted. We tested this algorithm on a simple test case with mixed inflow and outflow on the north and south boundaries. We found that to make it work robustly, one of the boundaries containing outflow must be excluded from the global velocity flux balancing step. It is unclear why this is needed, but we conjecture that by allowing all outflowing boundary faces to be adjusted, the problem is too unconstrained and can have multiple solutions. We also tested this method on the full Biglow Canyon case (without thermal stratification, as explained next, and without inflow perturbations), and the oscillating northerly component of the flow is naturally allowed to switch sign as a function of location and time on the north and south boundaries without any spurious effects, as shown in Figure 8.5.

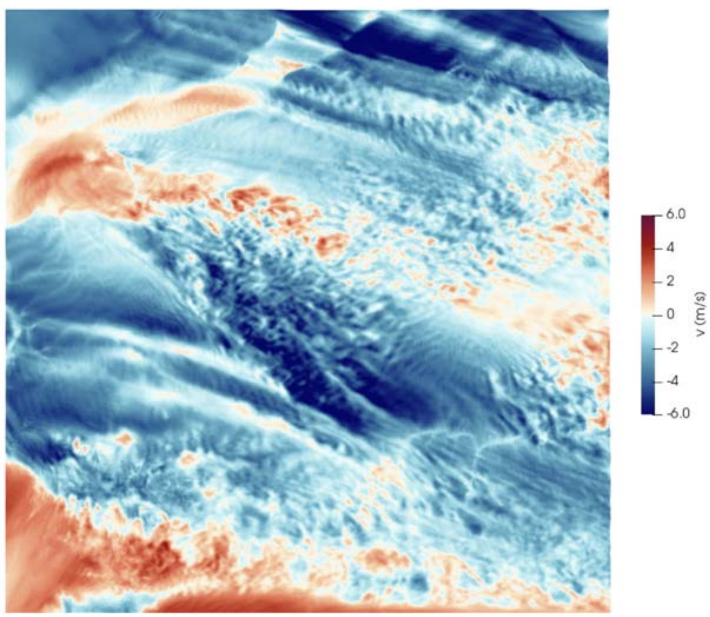

Figure 8.5. A terrain-following surface at 100 m above the surface showing contours of the northerly component of the flow at one instant in time. There are times in which the north and south boundary contain mixed inflow and outflow. Here, this is clearly seen on the south boundary.

A remaining issue to be solved is issue 4, the presence of spurious standing gravity waves originating at the inflow regions of the domain, which are shown in Figure 8.6. We believe these to be gravity waves, because they disappear if we set gravity to zero; however, these waves are peculiar because they are standing waves with regions of reverse flow circulation underneath. We have been able to re-create these waves in a simple two-dimensional case with stable stratification over the top of the boundary layer, like this case, by feeding in inflow that does not match the equilibrium LES solution. This is, perhaps, the problem we face in this complex case: possibly, the WRF inflow profiles do not match what LES predicts under the same conditions, causing a disturbance. We continue to look for a solution to this problem in FY19.

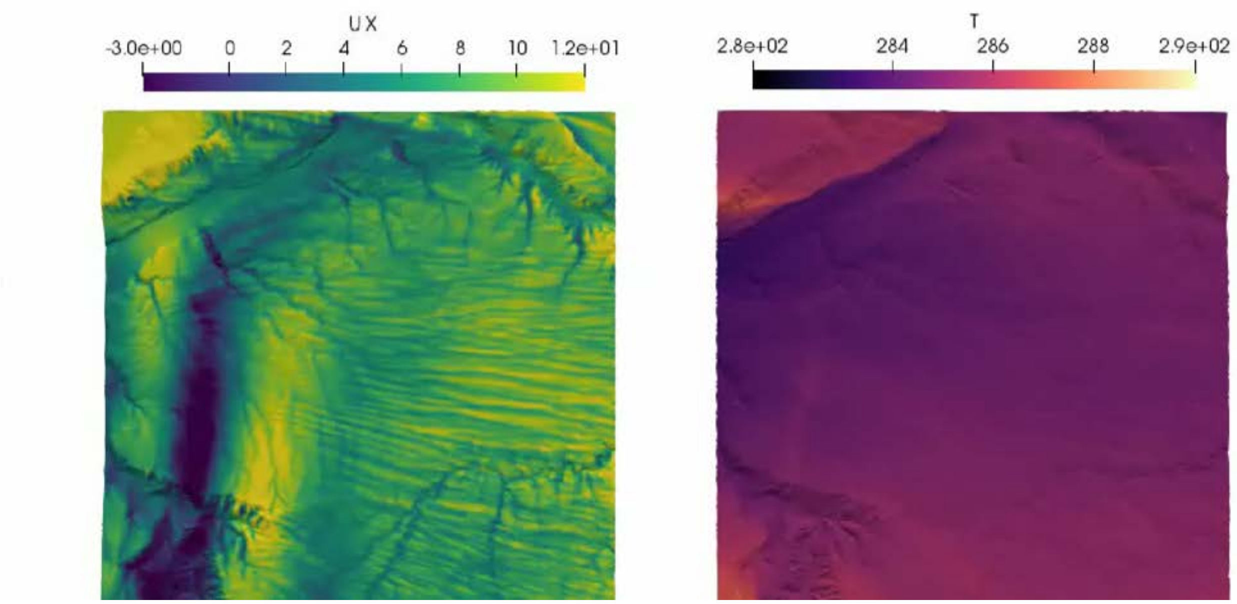

Figure 8.6. Terrain-following surfaces at 100 m above the surface of the westerly flow component (left) and potential temperature (right) 2 hours into the Biglow Canyon simulation, showing the presence of spurious standing gravity waves.

8.3 An Application of the Boundary Forcing Technique with a Unified Mesoscale and Microscale Solver: WFIP 2, November 15, 2016

A mesoscale-microscale coupled simulation was performed using the unified WRF to WRF-LES solver with multiple nested domains. The case simulated is the WFIP 2, November 15, 2016 case (the method of selecting this benchmark case is described in Section 2.1.2). Each domain is forced at its boundary by its parent domain, which has similarities to the approach shown in Section 8.2, but all in one code and all solved in the same simulation. This can also be referred to as the concurrent online simulation approach. This simulation used three domains, denoted as D01 through D03, as shown in Figure 8.7.

The horizontal grid spacing of the outer domain D01 is 1.215 km, whereas the grid spacing in the innermost domain is 15 m, obtained by using two grid refinement ratios of 9 between the nested and parent domains. The vertical grid spacing is set in such a way that its aspect ratio with respect to the horizontal grid spacing does not exceed more than one, in the innermost, fine resolution domain. The area of interest for the analysis is domain D03, which contains the WFIP 2 Physics Site that has observational data collected during the WFIP 2 field campaign. The Physics Site is also adjacent to the Biglow Canyon wind farm.

Ten hours of vertical profiles from the simulation were saved near the center of domain D03. To help develop turbulence properly, temperature perturbations were applied near the surface of lateral boundaries of both domains D02 and D03. Figure 8.8 shows a time series of temperature and wind speed/direction as well as the turbulent kinetic energy derived from simulated data of domain D03 and observational data at about 80 m above the surface. The turbulent kinetic energy was calculated using 15-minute statistical windows of the 1 Hz data. Assessment of these results is given in Section 8.4.

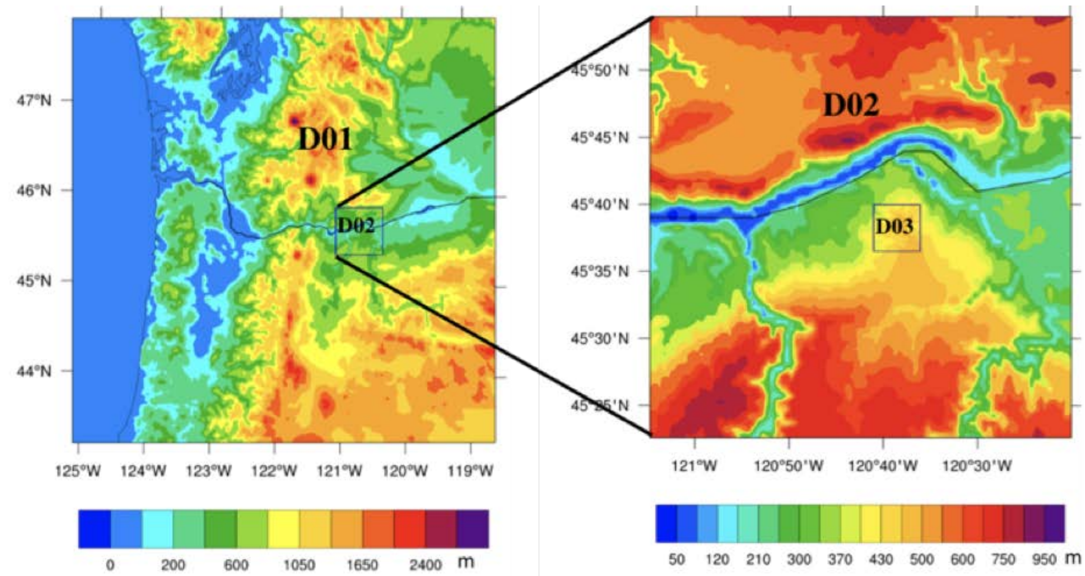

Figure 8.7. Domain configurations for a coupled mesoscale-microscale WRF simulation of the WFIP 2/Biglow Canyon region.

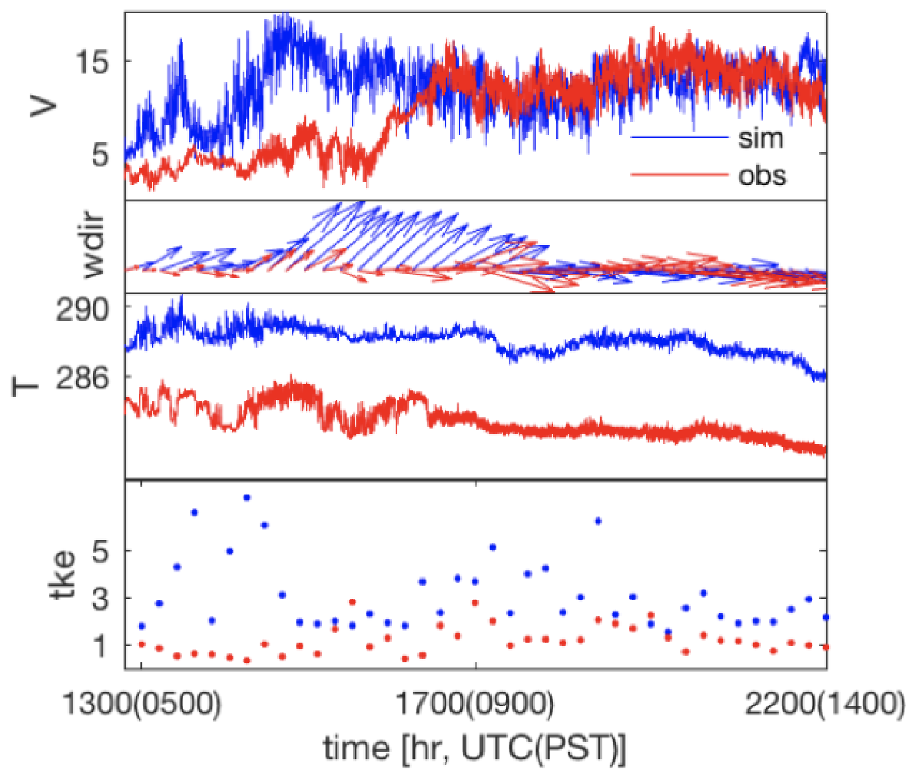

Figure 8.8. A time series of wind speed, wind direction, potential temperature, and turbulent kinetic energy derived from simulated and observed data from near the center of domain D03 at about 80 m above the surface.

8.4 Formal Assessment Results

The coupling method presented in Section 8.3, which uses a unified mesoscale-microscale solver along with inflow temperature perturbations to generate turbulence, is evaluated using a simulation based on the observations from WFIP 2. The assessment is based on observations made on November 15, 2016 when a signature of a weak frontal passage could be identified in the observations of wind speed and direction as well as potential temperature. Relatively rapid change in the observed wind speed at the Physics Site, 80-m tower, near the Biglow Canyon wind farm between 16:00 and 17:00 UTC (8 and 9 AM local time), can be seen above in Figure 8.8. Wind speed changes from 5 ms^{-1} to nearly 15 ms^{-1}. Over the same period of time, the wind also changes direction. Initially the wind direction varies from westerly to southwesterly. Following the frontal passage, the westerly wind direction prevails. Simultaneously, the temperature drops slightly, by 1-2°C, and the temperature variance decreases.

The analysis of model output from the innermost, large-eddy simulation domain with grid-cell size of 15 m collocated with the 80 m tower at the Physics Site, shown in Figure 8.8, indicates that the numerical simulation captured some elements of the frontal passage. However, the timing of the frontal passage is not captured well. In the simulation, the frontal passage occurs nearly two hours before it is observed. As a consequence, prior to the frontal passage, wind speed and turbulent kinetic energy (tke) are significantly higher than observed. In contrast, post-frontal features of the flow are, in general, accurately simulated. In particular, the post-frontal wind speed and direction are in excellent agreement with the observations. However, simulated temperature displays a bias of nearly 4°C. At the same time, simulated tke is higher than observed. The elevated tke could be associated with more vigorous convection that observed.

More detailed analysis of the passage of this weak cold front on November 15 will include spectral and cospectral analysis and comparison with observations at multiple locations within the Physics Site, where a range of instruments was deployed.

9.0 Chapter 9: Synthesis & Summary

A2e MMC project participants have been functioning as a team since mid-March 2015. The team has consisted of six DOE laboratories (ANL, LANL, LLNL, NREL, PNNL, and SNL [the latter's participation was dropped in FY17]) and NCAR (as a subcontractor to PNNL, the lead laboratory).

Within the context of a multiyear effort to develop, assess, and provide best practice MMC recommendations for the A2e HPM framework, the third year of effort during 2018 focused on:

- documenting and assessing the impacts of modeling at the mesoscale;
- assessing methods of initiating turbulence in microscale simulations;
- exploring methods to better represent the near-surface physics;
- evaluating the turbulence statistics for coupled model case studies in flat and in complex terrain.

The results and recommendations for each of these are summarized below.

9.1 Summary of Mesoscale Modeling and the *Terra Incognita*

The team has put some effort into understanding how the mesoscale model setup impacts the microscale simulation, largely in the context of WRF this year. A common issue that the team has identified is that if we wish to match the timing of nonstationary events, such as frontal passages, it must first be matched at the mesoscale if the microscale is expected to capture the phase well. In Chapter 4, that issue is studied for both complex and flat terrain cases. For the November 21, 2016 case in complex terrain at the WFIP 2 site, the HRRR simulation showed a phase error. Even when substituting different boundary conditions (from ERA-Interim), a phase shift persisted. That phase shift impacted all variables at each site.

The team is also continuing research begun in the WFIP 2 project to develop, test, and evaluate a new three-dimensional PBL scheme. To that end, the team began testing this scheme for the November 15, 2016 frontal passage case in the WFIP 2 domain. Difficulties have arisen, however, due to the triggering of gravity waves by the steep slopes of the mountains in that region. The team continues to test methods to alleviate these issues.

The team conducted a rigorous analysis of the impact of modeling in the *terra incognita* on the microscale simulations as reported in Chapter 5 and in more detail in Rai et al. (2018). We found that 1) the upper range of the *terra incognita* is roughly the current depth of the boundary layer, 2) using higher resolution for the mesoscale model will produce a smaller fetch distance in a microscale simulation that will thus contain more turbulent kinetic energy, 3) use of the Lilly turbulence model on the microscale domain results in a higher level of turbulence than using the MYNN or YSU mesoscale schemes, and 4) the microscale results do not vary with the type of turbulence model (PBL schemes or LES closure) used by its parent domain whose grid spacing falls within the *terra incognita*.

9.2 Summary of Turbulence Generation

Chapter 6 is devoted to analyzing methods to generate turbulence in the microscale flows, given that these motions are subgrid scale for the mesoscale models that drive them. In prior years, the team studied the application of stochastic perturbations in potential temperature at the inflow, the stochastic cell-perturbation method (SCPM). This year, the team added perturbations of the momentum field (force perturbations). Section 6.2 compares these methods directly, finding that application of force perturbations lead to a faster turbulence development in terms of distance from the inflow boundary. Neutral stability conditions benefit most from horizontal force perturbations, while convective conditions benefit more from vertical force perturbations.

Section 6.3 examined fully online-coupled MMC simulations with the WRF model forced by real data and employing full physics to examine agreement between the LES domain and observations using data from the SWiFT facility during both a diurnal cycle and a frontal passage case. The simulations broadly captured the trends of the prevailing meteorology; however, near-surface wind shear and resolved turbulent kinetic energy showed significant departures from the observations. Application of the SCPM improved the simulated turbulence content, but still produced values that were smaller than the observations. Testable hypotheses for some of the discrepancies were provided, motivating future work at improving the online coupling technique in WRF.

Section 6.4 examined application of the SCPM to improve the turbulence equilibration process under mesh refinement within turbulence-resolving simulations, from coarse LES to fine LES. A key difference for this application is that unlike mesoscale inflow, for which all turbulence is subgrid, in coarse-to-fine LES refinement, the inflow being downscaled already contains resolved turbulence. However a significant distance is still required for the flow and turbulence field to equilibrate to the finer mesh spacing. This study highlighted the flexibility of the SCPM to improve this application as well, showing that application of the perturbations to the velocities, rather than the potential temperature, and using smaller perturbation cells sizes can improve the coarse-to-fine LES equilibration process. This study also highlighted the potential for generalization of the method to a broader range of downscaling applications, including adaptive mesh refinement.

Section 6.5 assessed two different methods of adding turbulence at the inflow boundary based on observational data – the Veers and the Mann methods. Both methods were effective at generating turbulence at the microscale at multiple elevations, being most effective at the higher observed elevations. When the update frequency of turbulence added at the boundary was increased, the spectra of the simulations agreed even better with those observed.

A library approach is described and assessed in Section 6.6. In this case, periodic precursor runs are used to initialize the simulations and perturbations are added at the inflow. The turbulence spins up and evolves in both neutral and convective case simulations.

Section 6.7 describes a generalized boundary condition with velocity perturbations that would greatly enhance the efficiency of generating turbulence to superimpose TurbSim synthetic turbulence data on WRF-derived inflow data in a microscale solver like SOWFA or Nalu. This TurbSim-based method was effective at spinning up turbulence for a flat terrain simulation during transition to stable nighttime conditions. The period for turbulence spin up may be longer than preferred, however.

9.3 Summary of Near-surface Physics Improvements

Discovering the impact of differing methods to treat near-surface physics is treated in Chapter 7. Section 7.1 looks at two different methods of deriving surface fluxes for the microscale model – using the full land surface model available to WRF versus deriving a spatially averaged, yet temporally varying surface flux as input to the microscale model. It was shown that although any instantaneous view of the heat flux, vertical velocity, or wind speed may differ for these two different approaches, the statistics (in terms of profiles of wind components or tke and spectra) are essentially the same, demonstrating that there is no substantial difference between the approaches on the statistics of the flow. Although this analysis focuses on simulations in WRF and WRF-LES, the results are expected to transfer to the Nalu model.

Section 7.2 discusses the use of a pseudo-canopy model that applies drag terms to the momentum equations over a specified depth in place of Monin-Obukhov Similarity Theory. Three different PCM shape functions are explored, each improving on the standard MOST approach.

9.4 Summary of Coupling Techniques

The MMC team continued to develop, test, and evaluate several techniques to couple the mesoscale to the microscale. A first basic technique is nesting from the WRF model run in mesoscale mode into the WRF-LES mode, which we call the concurrent online approach. This technique was used for the studies of the *terra incognita* described in Chapter 5, as well as in the perturbation method approaches of Chapter 6 and the near-surface physics exploration of Section 7.1. This online approach was also used to study a frontal passage case for the WFIP 2 site, November 15, 2016 as described in Section 8.3. Using rather large grid refinement ratios of 9 between the nested and parent domains to skip over the *terra incognita*, the WRF simulation was able to capture the changes in the flow due to the frontal passage in terms of changes in wind speed, temperature, and tke, but the timing of the passage was incorrect (in the mesoscale as well as the microscale). The tke was higher than observed, and the team continues to investigate this feature.

The team also studied offline coupling between WRF-mesoscale model simulations and SOWFA as a proxy for Nalu (Sections 8.1 and 8.2). Two methods to integrate the mesoscale influence into the microscale solver were assessed for flat terrain (the SWiFT site) - 1) applying the large-scale advective and pressure-gradient terms extracted from the mesoscale simulation to the governing equations of the microscale solver, and 2) assimilating the mesoscale time-height history of mean wind velocity and potential temperature to generate microscale source terms. For this flat terrain case, the domain was treated as flat and periodic (a reasonable approximation of the SWiFT site under many conditions), so turbulence naturally forms without the need for boundary perturbations. Both methods showed success at forcing the mean quantities of wind speed and direction. The turbulence intensity was overpredicted by the assimilation approach, however. For complex terrain, the team attempted to use WRF-derived velocity, temperature, and surface sensible heat flux and skin temperature time series as boundary forcing for SOWFA. Four issues arose that the team has been working through: 1) mismatch in terrain resolution between the mesoscale and microscale simulation, for which some preliminary solutions have been tested with success, 2) the need for terrain-generalized inflow perturbations, which is under study, 3) boundary conditions of mixed inflow and outflow on a single boundary, which has been successfully addressed by using mixed boundary conditions (Dirichlet and Neumann), and 4) generation of spurious gravity waves at inflow regions, which is under study.

9.5 Next Steps

The MMC made substantial progress in FY18, but the team is also in the midst of some studies that will add to the knowledge base of coupled modeling. Some of the studies begun in FY18 will be completed in FY19. Those studies include:

1. The team is working toward producing an authoritative analysis of the various perturbation methods described in Chapter 6. The experimental setup for the assessment is described in Section 3.2.
2. Further analysis of best approaches to modeling the surface layer within both WRF and SOWFA/Nalu are needed, as well as studying how to make the approaches harmonious between the mesoscale and microscale.
3. The team has put considerable effort into studying best coupling methods between the mesoscale and microscale, but further study is needed to fully understand the advantages and disadvantages of each approach. It is expected that best practice methods may differ by situation and the purpose of the

application. The team also expects to rigorously assess how far one should nest WRF before handoff to Nalu.

4. Section 8.2 discusses several issues that arose in coupling WRF simulations to SOWFA for the complex terrain of the WFIP 2 study. The team will continue to investigate these issues, working toward a resolution that will be made known to the community.
5. The team will continue to study coupled modeling of nonstationarity in complex terrain in terms of cases of frontal passage by continuing to model cases from the WFIP 2 field study.

9.6 Impacts for Wind Plants

The research of the MMC team continues to define optimal methods for coupled modeling of wind plants. This coupled modeling approach is needed to reflect the energy flow from the largest scales of atmospheric motion down to the finest scales that impact the performance of individual turbines. By providing this coupled modeling approach, and working toward a full suite of opensource tools, this project will facilitate better planning, design, layout, and optimization of wind plants, thus facilitating deploying higher capacities of wind generation.

10.0 References

Araya, G., Castillo, L., Meneveau, C., and Jansen, K., 2011: A dynamic multi-scale approach for turbulent inflow boundary conditions in spatially developing flows. *Journal of Fluid Mechanics* **670**, 581–605.

Arthur, R. S., Mirocha, J. D., and Lundquist, K. A., 2018: Using a canopy model framework to improve large-eddy simulations of the atmospheric boundary layer in the Weather Research and Forecasting model, Accepted at *Mon.-Wea. Rev.*

Bailey, B. H., 2013: The financial impact of wind plant uncertainty, NAWEA Symposium, Boulder, CO, Aug. 06, 2013.

Haupt, S. E., Anderson, A., Berg, L., Brown, B., Churchfield, M., Draxl, C., Kalb, C., Koo, E., Kosović, B., Kotamarthi, R., Mazzaro, L., Mirocha, J., Quon, E., Rai, R., and Sever, G., 2018: Third Year Report of the Atmosphere to Electrons Mesoscale to Microscale Coupling Project, Pacific Northwest Laboratory Report PNNL-28259, 137 pp.

Haupt, S. E., Anderson, A., Kotamarthi, R., Churchfield, M., Feng, Y., Draxl, C., Mirocha, J., Quon, E., Koo, E., Shaw, W., Linn, R., Berg, L., Kosović, B., Rai, R., Brown, B., and Ennis, B., 2017: Second Year Report of the Atmosphere to Electrons Mesoscale to Microscale Coupling Project: Nonstationary Modeling Techniques and Assessment, Pacific Northwest Laboratory Report PNNL-26267, 156 pp.

Haupt, S. E., Anderson, A., Berg, L., Brown, B., Churchfield, M. J., Draxl, C., Ennis, B. L., Fang, Y., Kosović, B., Kotamarthi, R., Linn, R., Mirocha, J. D., Moriarty, P., Muñoz-Esparaza, D., Rai, R., and Shaw, W. J., 2015: First Year Report of the A2e Mesoscale to Microscale Coupling Project, Pacific Northwest Laboratory Report PNNL-25108, 124 pp.

Keating, A., Piomelli, U., Balaras, E., and Kaltenbach, H.-J., 2004: A priori and a posteriori tests of inflow conditions for large-eddy simulation. *Physics of Fluids* **16**, 4696–4712.

Kelley, C.L., and Ennis, B. L., 2016: SWiFT Site Atmospheric Characterization, Sandia Report SAND2016-0216, 82 pp.

Mann, J., 1998: Wind field simulation. *Probabilistic engineering mechanics* 13.4, 269-282.

Mazzaro L. J., Muñoz-Esparza, D., Lundquist, J. K. and Linn, R. R., 2017: Nested mesoscale-to-LES modeling of the atmospheric boundary layer in the presence of under-resolved convective structures. *Journal of Advances in Modeling Earth Systems* **9**, 1795–1810.

Mehta, D., van Zuijlen, A. H., Koren, B., Holierhoek, J. G., and Bijl, H., 2014: Large-Eddy Simulation of wind farm aerodynamics: A review, *J. Wind Eng. Ind. Aerodyn*. 133, 1–17.

Mirocha, J. D., Churchfield, M. J., Muñoz-Esparza, D., Rai, R., Feng, Y., Kosović, B., Haupt, S. E., Brown, B., Lee, B., Draxl, C., Rodrigo, J. S., Shaw, W. J., Berg, L. K., Moriarty, P., Linn, R., Kotamarthi, R. V., Balakrishnan, R., Cline, J., Robinson, M., and Ananthan, S., 2018: Large-eddy simulation sensitivities to variations of configuration and forcing parameters in canonical boundary layer flows for wind energy applications, *Wind Energy Sci.*, **3**, 589-613, https://doi.org/10.5194/wes-3-589-2018

Mirocha, J., Kosović, B., and Kirkil, G., 2014: Resolved Turbulence Characteristics in Large-Eddy Simulations Nested within Mesoscale Simulations Using the Weather Research and Forecasting Model. *Mon. Wea. Rev.* **142**, 806–831.

Mirocha, J. D. and Lundquist, K. A., 2017: Assessment of Vertical Mesh Refinement in Concurrently Nested Large-Eddy Simulations Using the Weather Research and Forecasting Model, *Mon. Wea. Rev.*, **145**(8), 3025-3048, https://doi.org/10.1175/MWR-D-16-0347.1

Morgan, B., Larsson, J., Kawai, S., and Lele, S. K., 2011: Improving Low-Frequency Characteristics of Recycling/Rescaling Inflow Turbulence Generation. *AIAA Journal* **49**, 582–597.

Muñoz-Esparza, D., et al., 2014: Bridging the transition from mesoscale to microscale turbulence in numerical weather prediction models. *Boundary-layer meteorology* 153.3, 409-440.

Muñoz-Esparza, D. and Kosović, B., 2018: Generation of Inflow Turbulence in Large-Eddy Simulations of Nonneutral Atmospheric Boundary Layers with the Cell Perturbation Method. *Mon. Wea. Rev.* **146**, 1889–1909.

Muñoz-Esparza, D., Kosović, B., van Beeck, J., and Mirocha, J., 2015: A stochastic perturbation method to generate inflow turbulence in large-eddy simulation models: Application to neutrally stratified atmospheric boundary layers. *Physics of Fluids (1994-present)* **27**, 035102.

Nakayama H., Takemi T., and Nagai H., 2011: Large-eddy simulation of urban boundary-layer flows by generating turbulent inflows from mesoscale meteorological simulations. *Atmospheric Science Letters* **13**, 180–186.

Patton, E. G. and Finnigan, J. J., 2012: Canopy turbulence. Handbook of environmental fluid dynamics, H. J. S. Fernando, Ed., Vol. 1, CRC Press, chap. 24, 311–328.

Poletto, R., Craft, T., and Revell, A., 2013: A New Divergence Free Synthetic Eddy Method for the Reproduction of Inlet Flow Conditions for LES. *Flow Turbulence Combust* **91**, 519–539.

Quon, E. W., Ghate, A. S., and Lele, S. K., 2018: Enrichment methods for inflow turbulence generation in the atmospheric boundary layer. *J. Phys.: Conf. Ser.*, **1037**, 072054, doi:10.1088/1742-6596/1037/7/072054.

Rai, R. K., Berg, L. K., Kosović, B., Haupt, S. E., Mirocha, J. D., Ennis, B., and Draxl, C., 2018: Evaluation of the Impact of Horizontal Grid Spacing in *Terra Incognita* on Coupled Mesoscale-microscale Simulations using the WRF Framework, submitted to *Monthly Wea. Rev.*, under revision.

Sanderse, B., van der Pijl, S. P., and Koren, B., 2011: Review of computational fluid dynamics for wind turbine wake aerodynamics, *Wind Energy* **14**, 799–819.

Sanz Rodrigo, J., Churchfield, M., and Kosović, B., 2017: A methodology for the design and testing of atmospheric boundary layer models for wind energy applications, *Wind Energ. Sci.*, **2**, 35-54, https://doi.org/10.5194/wes-2-35-2017

Shaw, W. J., Lundquist, J. K., and Schreck, S. J., 2009: Workshop on Research Needs for Wind Resource Characterization, *Bull. Amer. Meteorol. Soc.* **90**, 535–538.

Tabor, G. R. and Baba-Ahmadi, M. H., 2010: Inlet conditions for large eddy simulation: A review. *Computers & Fluids* **39**, 553–567.

Troldborg, N., Larsen, G. C., Madsen, H. A., Hansen, K. S., Sørensen, J. N., and Mikkelsen, R., 2011: Numerical simulations of wake interaction between two wind turbines at various inflow conditions, *Wind Energy*, **14**, 859–876.

Veers, P. S, 1988: Three-dimensional wind simulation. No. SAND-88-0152C; CONF-890102-9. Sandia National Labs, Albuquerque, NM (USA).

Zajaczkowski, F. J., Haupt, S. E., and Schmehl, K. J., 2011: A preliminary study of assimilating numerical weather prediction data into computational fluid dynamics models for wind prediction. *Journal of Wind Engineering and Industrial Aerodynamics* **99**, 320–329.

Appendix A

List of Project Publications

Appendix A

List of Project Publications

A.1 Journal Papers:

Arthur, R. S., Mirocha, J. D., and Lundquist, K. A., 2018: Using a canopy model framework to improve large-eddy simulations of the atmospheric boundary layer in the Weather Research and Forecasting model, Accepted, *Mon.-Wea. Rev.*

Abstract: A canopy model framework is implemented in the Weather Research and Forecasting model to improve the accuracy of large-eddy simulation (LES) of the atmospheric boundary layer (ABL). The model includes two options that depend on the scale of surface roughness elements. A resolved canopy model, typically used to model flow through vegetation canopies, is employed when roughness elements are resolved by the vertical LES grid. In the case of unresolved roughness, a modified "pseudo-canopy model" is developed to distribute drag over a shallow layer above the surface. Both canopy model options are validated against idealized test cases in neutral stability conditions and are shown to improve surface-layer velocity profiles relative to simulations employing Monin-Obukhov Similarity Theory (MOST), which is commonly used as a surface boundary condition in ABL models. Use of the canopy model framework also leads to increased levels of resolved turbulent kinetic energy and turbulent stresses. Because LES of the ABL has a well-known difficulty recovering the expected logarithmic velocity profile (log-law) in the surface layer, particular focus is placed on using the pseudo-canopy model to alleviate this issue over a range of model configurations. Tests with varying surface roughness values, LES closures, and grid aspect ratios confirm that the pseudo-canopy model generally improves log-law agreement relative to simulations that employ a standard MOST boundary condition. The canopy model framework thus represents a low-cost, easy-to-implement method for improving LES of the ABL.

Mirocha, J. D., Churchfield, M. J., Muñoz-Esparza, D., Rai, R., Feng, Y., Kosović, B., Haupt, S. E., Brown, B., Ennis, B. L., Draxl, C., Rodrigo, J. S., Shaw, W. J., Berg, L. K., Moriarty, P., Linn, R., Kotamarthi, R. V., Balakrishnan, R., Cline, J., Robinson, M., and Ananthan, S., 2017: Large-eddy simulation sensitivities to variations of configuration and forcing parameters in canonical boundary layer flows for wind energy applications, submitted to *Wind Energy Science.*

Abstract: The sensitivities of idealized large-eddy simulations (LES) to variations of model configuration and forcing parameters on quantities of interest to wind power applications are examined. Simulated wind speed, turbulent fluxes, spectra, and cospectra are assessed in relation to variations of two physical factors, geostrophic wind speed and surface roughness length, and several model configuration choices, including mesh size and grid aspect ratio, turbulence model, and numerical discretization schemes, in three different code bases. Two case studies representing nearly steady neutral and convective atmospheric boundary-layer (ABL) flow conditions over flat terrain, occurring at the Sandia Scaled Wind Farm Technology test facility, were used to force and assess idealized LES using periodic lateral boundary conditions. Comparison with fast-response velocity measurements at five heights within the lowest 50 m indicates that most model configurations performed similarly overall, with differences between observed and predicted wind speed generally smaller than measurement variability. Simulations of convective conditions produced turbulence quantities and spectra that matched the observations well, while those of neutral simulations produced good predictions of stress, but smaller than observed magnitudes of turbulent kinetic energy, likely due to tower wakes influencing the measurements during the neutral case. While sensitivities to model configuration choices and variability in forcing can be

considerable, idealized LES are shown to reliably reproduce quantities of interest to wind-energy applications within the lower ABL during quasi-ideal, nearly steady neutral and convective conditions.

Quon, E. W., Ghate, A. S., and Lele, S. K., 2018: Enrichment methods for inflow turbulence generation in the atmospheric boundary layer. *J. Phys.: Conf. Ser.*, **1037**, 072054, doi:10.1088/1742-6596/1037/7/072054.

Abstract: We investigate the feasibility of introducing synthetic turbulence into finite-domain large-eddy simulations (LES) of the wind plant operating environment. This effort is motivated by the need for a robust mesoscale-to-microscale coupling strategy in which a microscale (wind-plant) simulation is driven by mesoscale data without any resolved microscale turbulence. A neutrally stratified atmospheric boundary layer was simulated in an LES with 10-m grid spacing. We show how such a fully developed turbulence field may be reproduced with spectral enrichment starting from an under-resolved coarse LES field (with 20-m and 40-m grid spacing). The velocity spectra of the under-resolved fields are enriched by superimposing a fluctuating velocity field calculated by two turbulence simulators: TurbSim and Gabor Kinematic Simulation. Both forms of enrichment accurately simulated the autospectra of all three velocity components at high wavenumbers, with agreement between the enriched fields and the full-resolution LES observed at 400 m from the inflow boundary. In contrast, the spectra of the unenriched fields reached the same fully developed state at four times the downstream distance.

Rai, R. K., Berg, L. K., Kosović, B., Mirocha, J. D., Pekour, M. S., and Shaw, W. J., 2016: Comparison of measured and numerically simulated turbulence statistics in a convective boundary layer over complex terrain. *Bound.-Layer Meteor*., **163**, 69-98.

Abstract: The Weather Research and Forecasting (WRF) model can be used to simulate atmospheric processes ranging from quasi-global to tens of meters in scale. Here we employ large-eddy simulation (LES) using the WRF model, with the LES domain nested within a mesoscale WRF model domain with grid spacing decreasing from 12.15 km (mesoscale) to 0.03 km (LES). We simulate real-world conditions in the convective planetary boundary layer over an area of complex terrain. The WRF-LES model results are evaluated against observations collected during the US Department of Energy-supported Columbia Basin Wind Energy Study. Comparison of the first- and second-order moments, turbulence spectrum, and probability density function of wind speed shows good agreement between the simulations and observations. One key result is to demonstrate that a systematic methodology needs to be applied to select the grid spacing and refinement ratio used between domains, to avoid having a grid resolution that falls in the grey zone and to minimize artifacts in the WRF-LES model solutions. Furthermore, the WRF-LES model variables show large variability in space and time caused by the complex topography in the LES domain. Analyses of WRF-LES model results show that the flow structures, such as roll vortices and convective cells, vary depending on both the location and time of day as well as the distance from the inflow boundaries.

Rai, R. K., Berg, L. K., Pekour, M., Shaw, W. J., Kosović, B., Mirocha, J. D., and Ennis, B. L., 2017: Spatiotemporal variability of turbulent kinetic energy budgets in the convective boundary layer over both simple and complex terrain. *J. Appl. Meteor. and Climatol.*, doi:10.1175/JAMC-D-17-0124.1, in press.

Abstract: The assumption of subgrid-scale (SGS) horizontal homogeneity within a model grid cell, which forms the basis of SGS turbulence closures used by mesoscale models, becomes increasingly tenuous as grid spacing is reduced to a few kilometers or less, such as in many emerging high-resolution applications. Herein, we use the turbulent kinetic energy (tke) budget equation to study the spatiotemporal variability in two types of terrain—complex (Columbia Basin Wind Energy Study [CBWES] site, northeastern Oregon) and flat (Scaled Wind Farm Technology [SWiFT] site, West Texas) using the Weather Research and Forecasting (WRF) model. In each case six-nested domains (three domains each

for mesoscale and large-eddy simulation [LES]) are used to downscale the horizontal grid spacing from ∼10 km to ∼10 m using the WRF model framework. The model output was used to calculate the values of the tke budget terms in vertical and horizontal planes as well as the averages of grid cells contained in the four quadrants (a quarter area) of the LES domain. The budget terms calculated along the planes and the mean profile of budget terms show larger spatial variability at the CBWES site than at the SWiFT site. The contribution of the horizontal derivative of the shear production term to the total shear production was found to be ≈45% and ≈15% at the CBWES and SWiFT sites, respectively, indicating that the horizontal derivatives applied in the budget equation should not be ignored in mesoscale model parameterizations, especially for cases with complex terrain with <10 km scale.

A.2 Conference Papers: (presenter in bold)

Churchfield, M. J. and Quon, E., 2018: Coupling Mesoscale and Microscale Atmospheric Dynamics for Wind Plant Simulations in Complex Terrain, AMS Conference on Boundary Layers and Turbulence, Oklahoma City, OK, June 14, 2018.

Cline, J. W., **Shaw, W. J.,** and Haupt, S. E., 2018: Meteorology Research in DOE's Atmosphere to Electrons (A2e) Program, Ninth Conference on Weather, Climate, and the New Energy Economy, AMS Annual Meeting, January 8, 2018.

Cline, J., Haupt, S. E., and Shaw, W., 2017: Meteorology Research in DOE's Atmosphere to Electrons (A2e) Program, WindTech International Conference on Future Technologies in Wind Energy, Boulder, CO October 24, 2017.

Draxl, C., Churchfield, M., and Rodrigo, J. S., 2017: Coupling the Mesoscale to the Microscale Using Momentum Budget Components, North American Wind Energy Symposium, Ames, USA, September 2017.

Draxl, C., Churchfield, M., and Rodrigo, J. S., 2017: Coupling the Mesoscale to the Microscale Using Momentum Budget Components, AMS Annual Meeting, Seattle, USA, January 2017.

Haupt, S. E., Kosović, B., Shaw, W., Berg, L., Rai, R., Mirocha, J., Churchfield, M., Draxl, C., and Robinson, M., 2018: Recent Advances in Mesoscale to Microscale Coupling, AMS Conference on Boundary Layers and Turbulence, Oklahoma City, OK, June 14, 2018.

Haupt, S. E., 2018: Progress in Mesoscale to Microscale Coupling: Modeling Nonstationary Conditions in Flat and Complex Terrain, International Conference on Energy & Meteorology, Shanghai, China, May 22, 40 min. lecture.

Haupt, S.E., Berg, L., Churchfield, M., Cline, J., Mirocha, J., Kosović, B., Draxl, C., Rai, R., Kotatmarthi, R., Robinson, M., and Shaw, W., 2017: The US DOE A2e Mesoscale to Microscale Coupling Project: Nonstationary Modeling Techniques and Assessment, International Conference on Energy and Meteorology, Bari, Italy, June 28.

Haupt, S. E., **Cline, J.**, Shaw, W., Berg, L., Churchfield, M., Mirocha, J., Kosović, B., Draxl, C., Rai, R., Kotamarthi, R., 2017: The US DOE A2e Mesoscale to Microscale Coupling Project: Nonstationary Modeling Techniques and Assessment, European Geophysical Union, Vienna, Austria, April 26.

Haupt, S. E., Shaw, W., and Kosović, B., 2016: The DOE A2e Mesoscale to Microscale Coupling Project, AMS Symposium on Boundary Layers and Turbulence, Salt Lake City, UT, June 20.

Haupt, S. E., 2016: Meteorology Models Enabling Wind Energy, Wyoming Renewable Energy Summit, Laramie, WY, June 13. Invited Keynote.

Haupt, S. E., Shaw, W., and Kosović, B., 2015: Meso- to Microscale Coupling Project, WindTech Workshop, London, Ontario, Canada, October 19.

Kosović, B., Mirocha, J. D., Churchfield, M. J., Muñoz-Esparza, D., Rai, R. K., Feng, Y., Haupt, S. E., Brown, B., Ennis, B., Draxl, C., Sanz Rodrigo, J., Shaw, W. J., Berg, L. K., Moriarty, P., Linn, R., and Kotamarthi, R. V., 2017: Assessment of Large-eddy Simulations of the Atmospheric Boundary Layer for Wind Energy Applications, WindTech International Conference on Future Technologies in Wind Energy, Boulder, Co, October 25.

Mazzaro, L., Koo, E., Muñoz-Esparza, D., and Linn, R., 2018: Force-Based Perturbations for Turbulence Generation in Mesoscale-to-LES Grid-Nesting Applications, AMS Conference on Boundary Layers and Turbulence, Oklahoma City, OK, June 14, 2018.

Mirocha, J. D. and Haupt, S. E., 2018: The U.S. DOE Mesoscale to Microscale Coupling Project: Extending Boundary Layer Flow Simulation to Complex Environments, Ninth Conference on Weather, Climate, and the New Energy Economy, AMS Annual Meeting, January 8, 2018.

Mirocha, J. D., Rai R. K., Churchfield, M. J., Feng, Y., Draxl, C., Sanz Rodrigo, J., Ennis, B. L., Kosović, B., and Haupt, S. E., 2017: An investigation of online and offline mesoscale-microscale coupling techniques during unsteady meteorological conditions, WindTech International Conference on Future Technologies in Wind Energy, Boulder, Co, October 25.

Rai, R. K., Berg, L. K., Kosović, B., Mirocha, J. D., Haupt, S. E., Ennis, B. L., and Draxl, C., 2017: Evaluation of the Impact on *Terra Incognita* for Mesoscale and Microscale WRF Simulations, WindTech International Conference on Future Technologies in Wind Energy, Boulder, Co, October 25.

Rai, R. K., Berg, L. K., Kosović, B., Mirocha, J. D., Pekour, M., Ennis, B., and Shaw, W. J., 2017: Examination of the Spatio-temporal Variability of the Terms of the Turbulent Kinetic Energy Budget over a Complex Terrain in the Convective Boundary Layer: A Tool for Parameterization Development, American Meteorological Society Meeting, Seattle, WA, January 24.

Sever, G., Kotamarthi, R. V., Feng, Y., 2017: A turbulence library for asynchronous coupling of meso and microscale models, WindTech – International Conference on Future Technologies in Wind Energy, Boulder, CO, October 25, 2017.

Appendix B

Contributions of Individual Laboratories

Appendix B

Contributions of Individual Laboratories

The MMC project is truly a collaborative effort, with each laboratory taking a share of the effort as well as the team working together to advance the state-of-the-science of mesoscale-microscale coupling. The contributions of the individual laboratories (in alphabetical order) are briefly summarized herein:

Argonne National Laboratory (ANL): ANL primarily used carryover from FY17 for work performed this year. We continued working on our goals for the year. We developed a framework for building a library of precursor simulations for representative boundary conditions and then used the library to couple the evolution of atmosphere across mesoscale WRF-ARW (Advanced Research WRF) to microscale WRF-LES models. The challenge here is the generation of a library of simulations that could be useful for most frequent meteorological conditions that would influence the boundary-layer development at the microscale. As an initial test of the approach, we have focused on regions away from coast and terrain changes that could have a significant influence on the internal boundary-layer development. An ensemble of simulations is performed and evaluated for selected flow conditions at the SWiFT site in northeastern Texas. Our approach addresses two potential sensitivity cases (a) atmospheric stability states, including neutral and convective boundary layers, and (b) issues concerned with the time and spatial resolution of the precursor runs. For each stability case, the three key variables are the mean wind fields, surface heterogeneity and surface heat fluxes. The second key issue for implementing the library relates to the spatial resolution of the LES model and the frequency at which we need to save the model outputs for building the library. We will complete an initial construction of the turbulence library and perform test simulations using the asynchronous model coupling concept.

Lawrence Livermore National Laboratory (LLNL): LLNL staff worked with other members of the project team primarily on tasks related to online-coupled simulations using the WRF model, examination of alternate configurations of the stochastic cell-perturbation method (SCPM) for various applications, and improvements to the application of the surface boundary condition in atmospheric LES. Variants of the SCPM were shown to improve downscaling under a range of applications, from full-physics, real-data, multiple-domain WRF MMC simulations to idealized coarse-to-fine LES refinement studies, highlighting the flexibility of the SCPM to a broad range of general adaptive mesh refinement and downscaling applications. LLNL also led the development of a new distributed drag surface-layer model to improve application of the surface boundary condition within atmospheric LES codes. LLNL staff led the publication of two journal papers; a manuscript on the suitability of atmospheric large-eddy simulation to wind energy applications, comprising most of the MMC project team, which appeared in *Wind Energy Science*; and another describing the new distributed drag surface-layer model, accepted at *Monthly Weather Review*. LLNL staff also contributed to two PNNL-led journal articles, presented at the American Meteorological Society (AMS) Annual Meeting and Boundary Layers and Turbulence Symposium, worked with NCAR to lead the preparation of the formal peer-reviewed proposal that was submitted to DOE, provided guidance to other team members on other components of the project, and participated in both regular team conference and industry calls.

Los Alamos National Laboratory (LANL): LANL staff members led an MMC subgroup focusing on inflow turbulence-generation strategies at the mesoscale-microscale interface. This involved defining a benchmark case based on SWiFT observations, coordinating the multilab subgroup, along with running simulations. In addition to leading this subgroup, LANL staff also developed and tested a new force-based inflow turbulence-generation scheme. This work was presented at the American Meteorological Society Symposium on Boundary Layer Turbulence. The efforts of the multilab turbulence-generation group is reported in Chapter 6 of this report, the writing of which was heavily organized by LANL. LANL staff participates in all regular team phone calls, in-person meetings, and meetings with industry.

National Center for Atmospheric Research (NCAR): As a subcontractor to PNNL, NCAR took on project leadership, with Dr. Haupt serving as project Principal Investigator, leading most of the team teleconferences; presenting the project at A2e workshops or finding a proxy to do so; and presenting the work at several conferences, including preparing presentations for others to present at some meetings, preparing quarterly reports, and leading this fourth year report. NCAR hosted a team meeting in March where lab personnel came together to choose cases and finalize the technical approaches to modeling the nonstationary cases in both flat and complex terrain. At that meeting and beyond, NCAR led the process of formalizing goals, planning for the next three years of the project, and writing a formal proposal to DOE. NCAR was also responsible for the development and applications of the metrics, including developing the metrics plan and planning for the formal verification and validation of the model results, which appears in Chapter 3 of this report as well as embedded in several other chapters. That process required processing data from both the SWiFT tower and WFIP 2, as well as preparing model data. NCAR also supplied modeling advice and guidance. NCAR summarized the results of the assessment as well as the project overview and summary. NCAR coordinated the planning and assumed leadership for compiling and formatting this report, including writing major portions, although all laboratories contributed to the technical discussions and report writing.

National Renewable Energy Laboratory (NREL): Staff members at NREL have focused primarily on methods for coupling the mesoscale weather model with a separate wind-plant microscale model. In FY19, that work included work toward a fully coupled microscale simulation of the Biglow Canyon wind farm, improvements to a method to assimilate mesoscale mean profiles into the microscale through a controller, work on better understanding averaging requirements for the use of mesoscale tendencies to drive microscale simulations, advances in inflow perturbations for turbulence generation, and a study toward the requirements for the mesoscale-microscale interface location and turbulence perturbations in highly complex terrain. In addition to this topic, NREL's mesoscale expert has continued to provide support in mesoscale modeling and case selection. We also began a document about MMC validation using wind-plant data, and we coordinated with the NCAR assessment team to better understand its needs and communicate our assessment goals. NREL leads the MMC team concerned with overall MMC approaches, their differences, and their applications. We presented our Biglow Canyon simulation progress at the American Meteorological Society (AMS) Boundary Layers and Turbulence Symposium. We participate in all regular team phone meetings, meetings with industry, and in-person meetings in Boulder.

Pacific Northwest National Laboratory (PNNL): Staff members at PNNL have worked closely with scientists at ANL, LANL, LLNL, NREL, and NCAR. We worked with the team to identify specific cases for analysis from the WFIP 2 data set. Our team completed nested WRF-WRF/LES simulations for cases for the SWiFT site and WFIP 2, which were made available to NCAR staff for their evaluation and results from these simulations can be found throughout the report, along with some that were presented by Mirocha et al. (2018). We led the team's effort to analyze model behavior in the *terra incognita*. We also worked on the UQ part of the project and started to develop new ideas for application of UQ to microscale models. We made two presentations at the American Meteorological Society (AMS) Boundary Layers and Turbulence Symposium to provide updates to the community regarding the team's work on the *terra incognita* and inflow perturbation methods. We led the development of a manuscript presenting the *terra incognita* that is currently in revision for the AMS journal *Monthly Weather Review*. We worked closely with NCAR to lead the preparation of the formal peer-reviewed proposal that was submitted to DOE. We participated in both the regular team conference and industry calls.

Pacific Northwest
NATIONAL LABORATORY

www.pnnl.gov

902 Battelle Boulevard
P.O. Box 999
Richland, WA 99352
1-888-375-PNNL (7665)

U.S. DEPARTMENT OF
ENERGY